2014

Characteristics of High Energy Particle Interactions from the Study of Irregular Air Showers

Amir Hosein Shadkam
Louisiana State University and Agricultural and Mechanical College, a.shadkam@gmail.com

CHARACTERISTICS OF HIGH ENERGY PARTICLE INTERACTIONS FROM THE STUDY OF IRREGULAR AIR SHOWERS

A Dissertation

Submitted to the Graduate Faculty of the
Louisiana State University and
Agricultural and Mechanical College
in partial fulfillment of the
requirements for the degree of
Doctor of Philosophy

in

The Department of Physics and Astronomy

by
Amir Hosein Shadkam
B.S., Sharif University of Technology, 2006
M.S., Louisiana State University, 2012
August 2014

To my wife Sima, you are the joy of my life.

Acknowledgements

First of all I want to thank my adviser Prof. James Matthews for his support and kindness during all these years in graduate school. I have learnt both scientific thinking and professional academic ethics from him. I would like to thank Dr. Mike Sutherland and Dr. Viviana Scherini, the postdocs in our lab, for there suggestions and helps. Thanks to my brilliant colleagues Dr. Guefeng Yuan and Dr. Azadeh Keivani whom I benefited from there friendship. I would like to thank all my friends in LSU and Baton Rouge. You made living abroad an exciting and memorable experience.

Thanks to all the members of cosmic ray lab at Sharif University in Tehran, Dr. Samimi, Dr. Bahmanabadi and Dr. Khakian who trained me and provided me with a good foundation for my graduate studies. Dr. Bahmanabadi, you are truly my role model.

Thanks to my family, specially my parents Ali Shadkam and Azar Siasi for their love and support during all these years. You are always in my heart. Thanks to my aunt "khaleh Mina", you are a wonderful "khaleh".

I would like to thank my wife Sima, for all of the sacrifices she made for me. Your presence has given me energy and hope to finish this thesis. I feel blessed to have you in my life.

Table of Contents

Acknowledgements . . . iii

Abstract . . . vi

1. Introduction . . . 1
   - 1.1 Discovery of Cosmic Rays . . . 1
   - 1.2 Energy Spectrum . . . 2
   - 1.3 Extensive Air Showers . . . 3
   - 1.4 Cosmic Ray Shower Profile . . . 3
   - 1.5 Fermi Acceleration . . . 4
   - 1.6 GZK Cutoff . . . 7

2. Pierre Auger Observatory . . . 12
   - 2.1 Overview . . . 13
   - 2.2 Surface Detector . . . 13
   - 2.3 Fluorescence Detector . . . 15
     - 2.3.1 FD Triggers . . . 16
     - 2.3.2 Shower Axis Reconstruction . . . 17
     - 2.3.3 Longitudinal Shower Reconstruction . . . 18
   - 2.4 Hybrid Events . . . 20
   - 2.5 Atmospheric Aerosol and Cloud Monitoring . . . 21
     - 2.5.1 LIDARs . . . 22
     - 2.5.2 Cloud Camera . . . 22

3. Analysis . . . 23
   - 3.1 Leading Particle Physics . . . 24
   - 3.2 Basic Model . . . 26
   - 3.3 Fit Methods . . . 31
     - 3.3.1 Gaisser-Hillas Function . . . 31
     - 3.3.2 Gaussian Function in Age (GFA) . . . 32
     - 3.3.3 Energy Dependence of GFA Fit Parameters . . . 33
     - 3.3.4 Imposed Fluctuations in Simulated Shower Profiles . . . 37
     - 3.3.5 2 Added Air Showers . . . 40
     - 3.3.6 Two-GFA Fit on The Simulated Air Showers . . . 45
     - 3.3.7 Two Added Showers Separated With Exponential Distribution . . . 53
     - 3.3.8 Differences Due to Composition . . . 55

4. Contaminated Data . . . 55
   - 4.1 Cloud Identification with Satellite . . . 56
     - 4.1.1 GOES Satellites . . . 57
   - 4.2 Cherenkov Light . . . 63
     - 4.2.1 Atmospheric Density Model . . . 64
     - 4.2.2 Number of Radiated Cherenkov Photons . . . 67
     - 4.2.3 Rayleigh Scattering . . . 70

4.2.4 Mie Scattering 72
4.2.5 Reconstructed Cherenkov Light at Auger Fluorescence Detector . . . 73

5. Auger Events 77
5.1 Events Selection 77
5.2 Cloud Contamination 78
5.3 Cherenkov Light Contamination 80
5.4 Separation Distribution (ΔX) Between Fitted Sub-showers 82
5.5 Interpretation of the Result 84

Bibliography 88

Vita 90

Abstract

Since the discovery of cosmic rays about one century ago, there have been two main approaches in their experimental study. The first is analyzing their arrival directions, energies, and composition in order to determine the nature of their source or sources. The second is analysis of their interactions in the atmosphere to learn about the structure of elementary particles through the characteristics of their collisions at extremely high energy. The energy available in the collisions of cosmic ray protons with atmospheric nuclei exceeds greatly that achieved or achievable in any man-made accelerators. The study of these interactions may reveal the existence of new, exotic particle states, as well as the details of particle structure. The Pierre Auger Observatory is the largest cosmic ray experiment ever constructed. It records air shower data from the interactions of primary cosmic ray particles with energies from 10^{18}eV to beyond 10^{20}eV. The interaction energies of these events exceed the LHC at CERN by one to two orders of magnitude. I have developed a new method that seeks to identify leading particles with long tracks emerging from the primary interaction. The technique characterizes the properties of the leading particles, giving information on inelasticity and cross-section in a regime well beyond current accelerator data. The method identifies events with irregular air shower development. These events are compared to expectations from CONEX air shower simulations using the current event generator QGSJET-II. To eliminate background events, real-time data on cloud cover at the site are employed. We have measured the interaction length for the leading particles with mean energy near 10^{18}eV. Based on the predicted leading particle composition in QGSJET-II, we have determined an interaction length for protons. The method does not find any irregular air showers in simulations of iron primaries. The analysis demonstrates the proton primaries are present in the cosmic rays at these energies.

1. Introduction

1.1 Discovery of Cosmic Rays

Cosmic rays are high energy charged particles originating from outer space and coming toward us. The fact that they have extra terrestial origin was first discovered by Vitor Hess [1] one century ago. During a series of balloon flight experiments, he observed the flux of penetrating radiation (at that time they thought to be gamma rays) increases with the altitude.

For the physicists of early 20^{th} century, before the huge acceleraors were built, cosmic rays were the unique source of high energy particle physics experiments. Cosmic ray interactions in the atmosphere produce many elementary particles for free. Many were predicted by theorists before their actual discovery. The positron was discovered by Anderson in 1932 [2] (Nobel prize 1936) , whereas the existance of this particle had been predicted by Dirac in 1928. The muon was discovered by Anderson and Neddermeyer in 1937 [3] and its properties were as same as those predicted by Yukawa. Both particles were detected in a cloud chamber exposed to the cosmic rays.

Discovery of very unstable and short life mesons such as the charged pions demanded more sophisticated and precise detectors to trace. Discovery of these particles became possible in 1947 when Occhialini and Powell [4] discovered charged pions using nuclear emulsions exposed to cosmic rays at mountain altitudes.

In 1962 Linsley detected an Air Shower using an array of scintillators in Volcano Ranch, New Mexico [5]. He estimated the primary cosmic ray energy to be 10^{20}eV. This was the first evidence for existance of Ultra High Energy Cosmic Rays. Our galaxy can't confine a cosmic ray with such a high energy, and there is no known mechanism in our galaxy that can produce or accelerate particles up to this energy. So it has been concluded that it should have extragalactic origin.

1.2 Energy Spectrum

The high energy primary cosmic ray energy spectrum covers a very large range of energy from 1GeV to 10^{11}GeV and above. The low energy part of primary spectrum (< 1GeV) is modified by the Sun's and Earth's magnetic fields. The spectrum is a steeply decreasing power law with $\gamma \approx 3$ (Figure 1.1).

$$\frac{dE}{dN} \sim E^{-\gamma} \tag{1.1}$$

The flux of primary particles for energies more than 10^2GeV is about $1/\mathrm{m}^2/\mathrm{sec}$ and it falls to $1/\mathrm{m}^2/\mathrm{yr}$ for energies more than 10^7GeV.

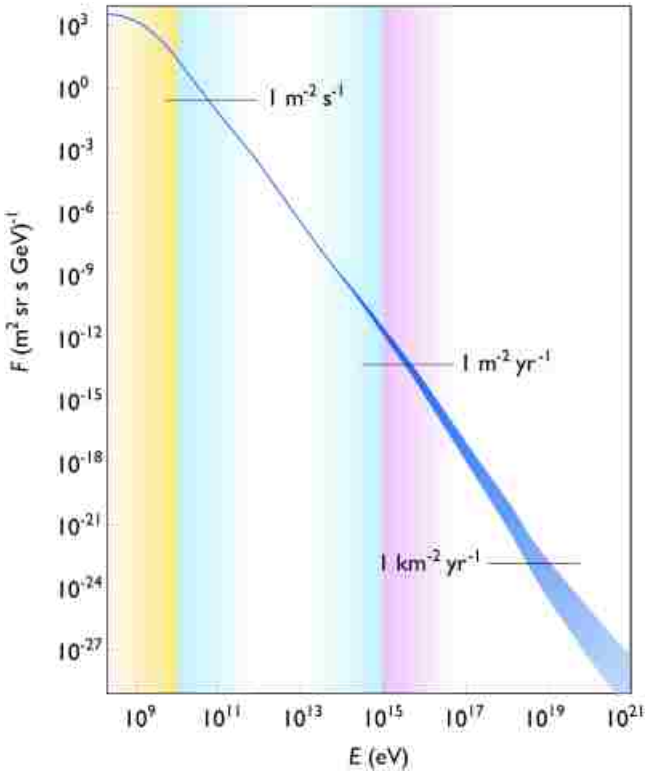

Figure 1.1: Cosmic Rays Energy Spectrum from 10^9 eV to 10^{21} eV, figure by S. Swordy of Univ. of Chicago

1.3 Extensive Air Showers

When a hadronic primary cosmic ray interacts with the air molecules (mostly nitrogen), it produces secondary particles like pions and other hadrons (Figure 1.2). The π^0 decays immediately to 2 or 3 gamma rays that initiate the electromagnetic part of the shower. The hadronic part continues the interactions until most of the charged pions decay to muons. Muons have very small cross section and usually arrive to the ground without any interaction. The gamma rays from the π^0 produce electron-positron pair. The electrons emit bremsstrahlung radiation and this cycle repeats with more gamma rays. At the same time, the electrons ionize the air and lose more energy through ionization process. The deflected low energy electrons excite the nitrogen molecules through fluorescence process and emit UV light. This light is the basis for detection of longitudinal development of air showers in the Pierre Auger Observatory.

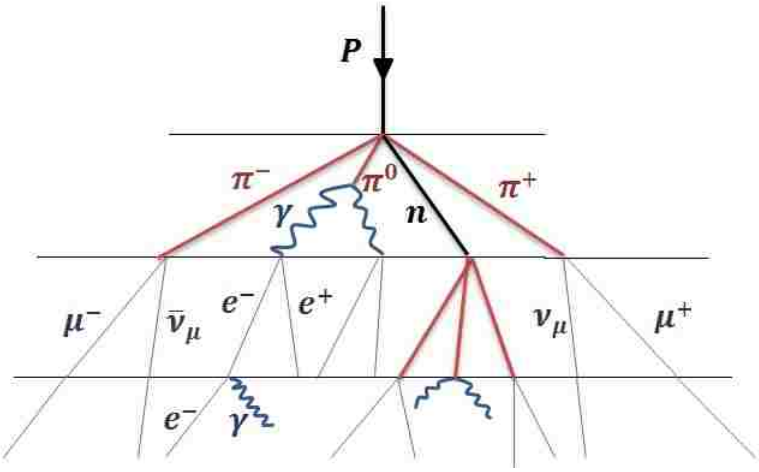

Figure 1.2: Schematic diagram of an extensive air shower

1.4 Cosmic Ray Shower Profile

Shower profile (figure 1.3) is the number of charged particles versus the shower depth X(g/cm^2). The air shower deposited energy in the atmosphere is directly related to the number of charged particles in the air shower. The fluorescence emission is proportional to the deposited energy of shower. So, the shower profiles could be shown in energy deposited

per unit of slant depth (eV / (g/cm^2)).

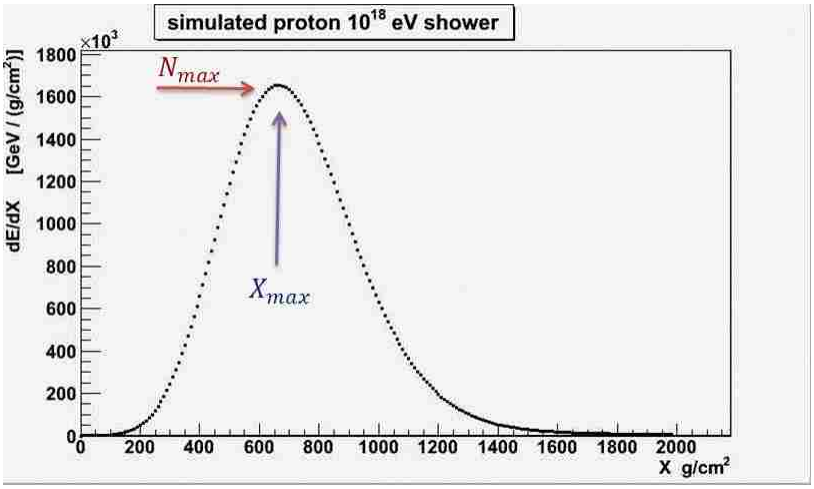

Figure 1.3: A simulated shower profile

1.5 Fermi Acceleration

In 1949 Enrico Fermi proposed a mechanism for acceleration of cosmic rays that could explain the power law spectrum of cosmic rays [7]. His suggestion is based on collisions between the cosmic ray and magnetized interstellar clouds. The cosmic ray could gain energy from head-on collisions and lose energy from hitting a cloud that moves along its direction. There is more statistical chance for the former to happen, so the cosmic ray will gain energy on average.

The main problem with this model is that the total acceleration process is inefficient [44]. The gained energy should overcome the energy that cosmic ray loses through ionization loss and synchrotron radiation. In the Fermi process the gained energy is proportional to $(V/c)^2$ where V is the cloud speed. This second order dependance weakens the acceleration process because $(V/c) \ll 1$.

In 1970s, the shock wave acceleration model was suggested by scientists [10, 11]. In this model The essence of the process is the same as the Fermi's, but the idea of interstellar clouds is substituted with a shock wave (from a supernova). The total acceleration process will happen because of repeated collisions of the cosmic ray with the same shock wave. The

advantage with this model is that the gained energy is proportional to the first order of V/c value. Also the shock waves have much higher speed than interstellar clouds.

Here, a simplified one dimensional example of the acceleration process will be explained. In figure 1.4, a proton with energy E_1 hits a shock wave moving in opposite direction with speed V. The proton enters the shock wave region, it gets deflected 180° degrees by the magnetic field and comes out of the shock wave region. The primary energy and momentum of the proton in the shock wave's rest frame is

$$E_1' = \gamma(E_1 + VP_1) \tag{1.2}$$

$$P_1' = \gamma(P_1 + \frac{V}{c^2}E_1) \tag{1.3}$$

where $\gamma = (1 - \frac{V^2}{c^2})^{-\frac{1}{2}}$ is the lorentz factor of the shock wave inertial frame.

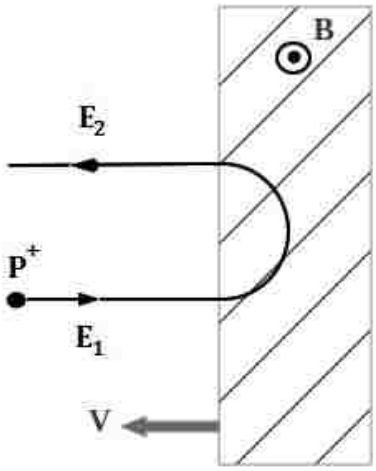

Figure 1.4: A schematic draw of proton head-on collision with a magnetized region. The magnetized region moves with speed V. The proton will gain energy in this process.

The magnetic field changes the particle direction without changing its momentum and energy.

$$\overrightarrow{P_2'} = -\overrightarrow{P_1'} \tag{1.4}$$

$$E_2' = E_1'$$

As the particle exits the shock wave, its energy needs to transfer back to the observer frame [12].

$$E_2 = \gamma(E_1' + VP_2') = E_1(1 + 2\gamma^2\frac{V^2}{c^2}) + 2\gamma^2 V\frac{\upsilon E_1}{c^2} \tag{1.5}$$

The proton gains ΔE energy during this process,

$$\Delta E = E_2 - E_1 = 2\gamma^2\frac{V}{c}E_1\left(\frac{V}{c} + \frac{\upsilon}{c}\right) \tag{1.6}$$

where υ is the particle's initial speed.

A static magnetic field does no work on a charged particle, and it can't give energy to the particle. But a moving magnetic field induces an electric field that can accelerate the charged particle. It is assumed that the particle has relativistic speed ($\upsilon \simeq c$) and the shock wave speed is very small with respect to the speed of light ($\frac{V}{c} \ll 1$). So the gained energy fraction becomes

$$\frac{\Delta E}{E} \simeq 2\frac{V}{c}. \tag{1.7}$$

In practice, The shock wave region has turbulent magnetic field and the non-unform matter density. The scattering and magnetic deflections can trap the particle in the shock wave region [9,11]. The particle goes back and forth many times, and it gains a small fraction of energy (α) every time. The following equation shows the gained energy after n collisions.

$$E = E_0(1 + \alpha)^n \tag{1.8}$$

There is a probability P_{esc} for the particles to escape the shock wave region. In this case the acceleration will be stopped. So equation 1.9 shows the number of particles remaining in the shock wave region after n collisions.

$$N = N_0(1 - P_{esc})^n \tag{1.9}$$

The escape probability P_{esc} is a function of energy, here we make a rough estimation and keep it as a constant. Further calculation shows the power law spectrum prediction for the cosmic rays (equation 1.13).

$$ln\frac{E}{E_0} = n\ ln(1+\alpha) \tag{1.10}$$

$$ln\frac{N}{N_0} = n\ (1 - P_{esc}) \tag{1.11}$$

$$\frac{ln\frac{N}{N_0}}{ln\frac{E}{E_0}} = \frac{ln(1 - P_{esc})}{ln(1+\alpha)} = -\eta \tag{1.12}$$

$$\frac{N}{N_0} = \left(\frac{E}{E_0}\right)^{-\eta} \tag{1.13}$$

The finite size of the shock front limits the maximum energy gain [9], because it can't confine a particle with too large gyroradius. The maximum achievable energy through this process is estimated to be around 5×10^5 GeV [44].

1.6 GZK Cutoff

The cosmic microwave background radiation (CMBR) was accidentally discovered by the American astronomers Penzias and Wilson in 1964 [13]. The CMBR has a thermal (blackbody) spectrum with temperature T=2.73 K. Shortly after its discovery, Greisen [14] and Zatsepin and Kuz'min [15] (GZK) predicted that high energy cosmic ray protons (E $>\sim$ 10^{19}eV) have sufficient energy to interact with CMB photons and excite the Δ^+ resonance, producing pions. The proton emerges from the interaction with less energy. This photo-pion production process will repeat until the proton energy drops below the threshold. So

the spectrum of proton cosmic rays that reach earth will show few or no events above the threshold energy region, an effect known as the GZK cutoff.

$$p^+ + \gamma_{CMB} \rightarrow \Delta^+ \rightarrow p^+ + \pi^0 \qquad (1.14)$$
$$\rightarrow n + \pi^+$$

In order to estimate the energy threshold for the reaction, we calculate the invariant mass $\sqrt{s}$ of the initial state (with c=1):

$$\begin{aligned} s_i &= (E_p + E_\gamma)^2 - (\mathbf{p}_p + \mathbf{p}_\gamma)^2 \\ &= E_p^2 + E_\gamma^2 + 2E_pE_\gamma - p_p^2 - p_\gamma^2 - 2\mathbf{p}_p \cdot \mathbf{p}_\gamma \\ &= m_p^2 + 2E_pE_\gamma - 2\mathbf{p}_p \cdot \mathbf{p}_\gamma \\ &= m_p^2 + 2E_pE_\gamma(1 - \beta\cos\theta) \\ &= m_p^2 + 4E_pE_\gamma \qquad\qquad (\text{for } \ \theta = 180^\circ) \end{aligned} \qquad (1.15)$$

where $\beta \approx 1$ at extreme energy. We have used $\theta = 180^\circ$ since a head-on collision corresponds to the minimum proton energy needed for a given value of s_i. This quantity is conserved as well as Lorentz-invariant, so it will have the same value as it has in the final state in the center-of-mass frame, where the Δ^+ is at rest:

$$s_f = m_\Delta^2 = (1232\text{Mev})^2.$$

Equating the initial and final invariant masses,

$$s_i = s_f \ \Rightarrow \ \ E_p = \frac{m_\Delta^2 - m_p^2}{4E_\gamma}. \qquad (1.16)$$

Figure 1.5 shows recent measurements of the CMBR spectrum by different experiments. The data fit a Planck blackbody radiation curve extremely well, especially near the peak. In order to estimate the threshold energy E_p in Eq. 3, we should choose a target photon energy E_γ that is in the highest energy tail of the CMBR spectrum. We take, somewhat arbitrarily, $E_\gamma = 3 \times 10^{-3}$ eV, corresponding to an intensity of about 1/100 of the peak of the distribution. With this choice,

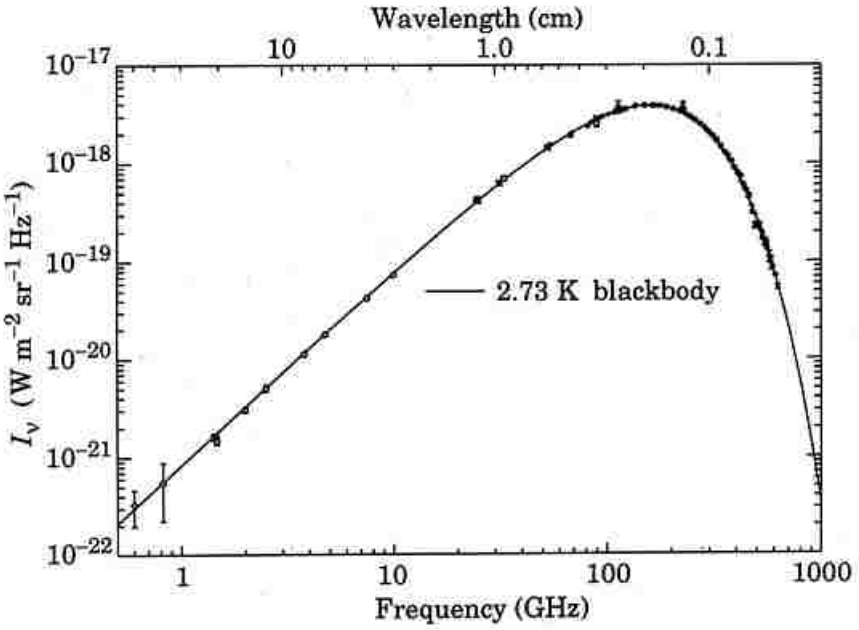

Figure 1.5: Precise measurement of CMBR spectrum with different experiments. The line represents a blackbody with T=2.73 K. Picture taken from [17].

$$E_p = \frac{m_\Delta^2 - m_p^2}{4E_\gamma} \approx \frac{(1232^2 - 938^2)\ MeV^2}{4 \times 3 \times 10^{-3}\ eV} \approx 5 \times 10^{19} eV.$$

The mean free path for protons above threshold depends on the number density n of CMBR photons and on the proton-photon interaction cross-section $\sigma_{\gamma p}$. This density is obtained by integrating the Planck function over all energies (or wavelengths):

$$n = \int_0^\infty n_\lambda d\lambda = \int_0^\infty \frac{8\pi/\lambda^4}{\exp(hc/\lambda kT) - 1} d\lambda = 16\pi\zeta(3) \left(\frac{kT}{hc}\right)^3 \tag{1.17}$$
$$\approx 400 \ \frac{photons}{cm^3}$$

where $\zeta(3) = 1.202$ is the Riemann zeta function. The γp interaction has been well-studied for many years at accelerators. Fig. 1.6 shows a compilation [18] of measurements of the cross section $\sigma_{\gamma p}$, as a function of the photon energy ϵ' (observed *in the proton rest frame*).

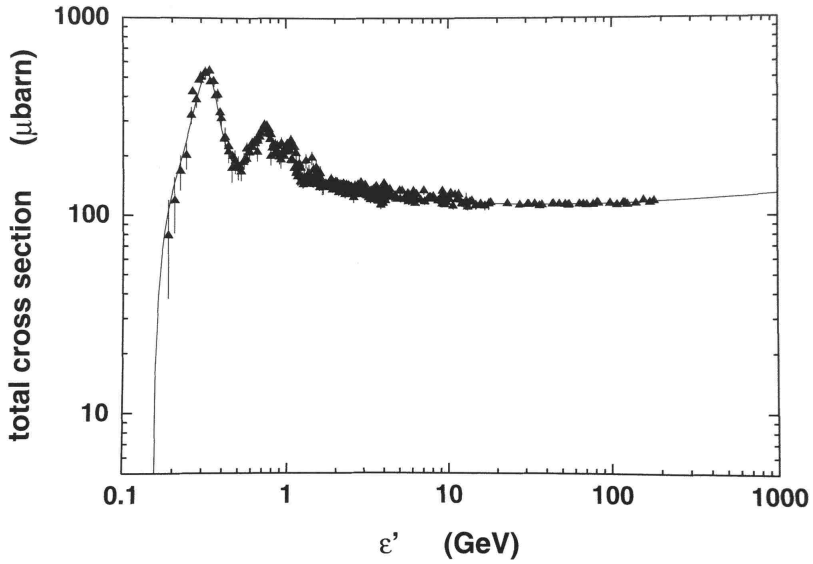

Figure 1.6: Energy dependence of proton-photon interaction total cross-section in the nucleon rest frame. ϵ' is the photon energy in this frame. Picture taken from [16]

The photon energy E_γ that we chose above, when transformed to this frame, corresponds closely to the peak of the cross section curve in Fig. 2, with a value there of $\sigma_{\gamma p} \approx 600\mu b$, giving the mean free path as

$$\text{Proton mean free path} = \frac{1}{n\sigma_{p\gamma}} = \frac{1}{400cm^{-3} \times 600\mu b} \approx 1.4 \ Mpc.$$

The calculations above serve only to give the order of magnitude of the effect. It is seen

that a beam of cosmic ray protons will begin to be disrupted when their energies exceed a few$\times 10^{19}$ eV and their path lengths exceed a few Mpc. Proper calculations have been done [18], carefully convolving the energy dependence of the $\sigma_{\gamma p}$ with the CMBR energy spectrum.

Moreover, the Δ^+ that is created decays quickly, most often to a $p\pi^\circ$ pair, with the outgoing p having on average only about 83% of the incoming proton energy [18]. So the beam of cosmic ray protons will continue, but with reduced energy. These protons themselves can undergo further GZK interactions, as long as their energies are above threshold.

Figure 1.7 shows the results of a simulation of the GZK interaction [20]. It gives the mean energy of a proton beam as a function of the distance it has propagated through the CMBR. For example, a beam with an initial energy of 10^{21}eV will have its energy degraded to less than 10^{20} eV after traveling about 100 Mpc.

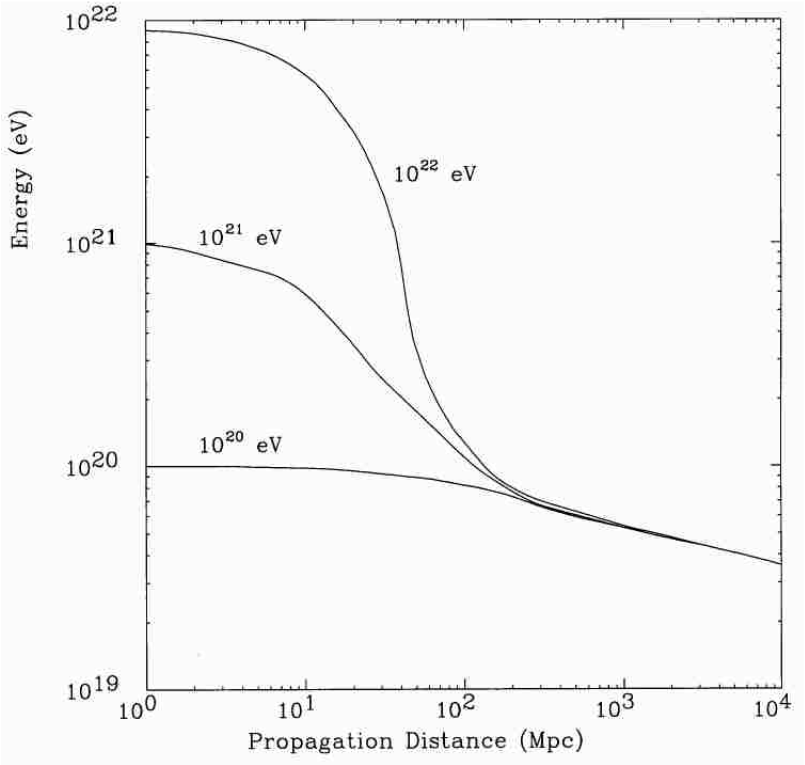

Figure 1.7: Proton energy versus the propagation distance through the CMBR. The lines represent initial proton energies 10^{20}, 10^{21} and 10^{22}eV. Picture taken from [21]

A similar result holds for all initial energies above threshold. From this we may conclude

that any cosmic ray protons that are *observed* at earth with energies exceeding $\sim 10^{20}$ must have originated within about 100 Mpc from earth. If the sources are distributed throughout the universe, then the energy spectrum observed at earth will be suppressed above the GZK threshold (the so-called *GZK cutoff*). Most candidate sources (such as AGN) for cosmic rays are far from isotropically distributed within this relatively nearby neighborhood. We expect that in such a case, the GZK effect will impose anisotropy on the distribution of arrival direction of cosmic rays observed above the GZK threshold [20].

2. Pierre Auger Observatory

2.1 Overview

The Pierre Auger Observatory is the largest "hybrid" cosmic ray air shower experiment (figure 2.1). It is specially designed to study the highest energy cosmic rays above 10^{18}eV (1 EeV). "Hybrid" refers to its use of multiple detection techniques to reconstruct the primary cosmic ray's energy, arrival direction, and inferred particle composition from the characteristics of the extensive air shower. Two main independent detection techniques are implemented: Surface Detection and Fluorescence Detection.

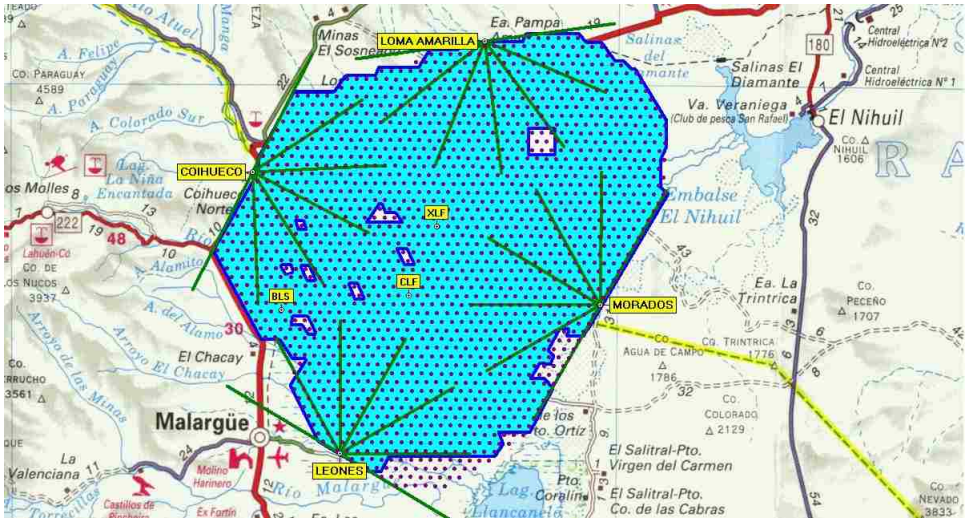

Figure 2.1: Detector map of the Pierre Auger Observatory. Purple dots are surface detector tanks and the four fluorescence detectors (eyes) are located on four sides of Observatory. Green lines indicate each eye's pointing direction.

2.2 Surface Detector

The Surface Detector (SD) is comprised of over 1600 water Cherenkov tanks deployed on a 1.5 km triangular grid, covering about 3000 km^2. Each tank has 1.2m height and 10m^2 collection surface. It is filled with 12000 liters of purified water, which is used as detection medium. It has 3 photomultipliers(PMTs) oriented downward, to face the water. There are two solar panels (see figure 2.2) connected to two 12V batteries that supply the power needed for all the electronics and communication.

When high energy particles from a cosmic ray air shower pass through the tank, Cherenkov light is emitted because they are traveling faster than the speed of light in water. The main secondary particles reaching the ground are $e^{\pm}$, γ (EM component) and muons. The muons cross section is low and their average energy is high ($>$ 1GeV) so they pass through the tank and make a narrow and large signal. The EM particles on average have few MeV (5-10 MeV) energy, and they will lose it all mainly through ionization loss in water. The EM particle statistic is much larger than muons, but they have a short track length in the water so much less Cherenkov photons are radiated per particle. Also the shower front has a thickness that causes an arrival time distribution for the EM particles and makes their signal wide with small amplitude. The tanks are specifically designed to fully absorb the EM particles and optimise the muon pulse amplitude.

There are two kinds of event triggers defined based on the EM and muon signal in the tank. First is threshold trigger (ThT) which is satisfied when all 3 PMT's detect a signal above 1.75VEM (vertical Equivalent Muon). This trigger is set to be sensitive to the Muons of the shower front. One VEM corresponds to the average recorded signal from one Muon passing vertically through the tank. The 1 VEM signal is measured using two scintillators on top and bottom of the tank. If a single muon pass through both scintillators, the recorded signal from tank is used to define the VEM unit.

Second trigger is time_over_threshold (ToT) which is satisfied when 13 out of 120 FADC bins have signal above 0.2 VEM (each bin corresponds to 25 ns time). This ToT trigger is sensitive to the integral of the signal. It is specifically set to be sensitive to the EM part of the shower.

The PMTs detect the light and pass the signal to onboard electronics. There is a GPS receiver on each detector to record the exact trigger time. The timing accuracy is crucial for reconstruction of shower plane. The SD trigger time is also important to reconstruct the shower axis in hybrid events.

Figure 2.2: A working SD station. The communication antenna and solar panel to charge the batteries are visible.

2.3 Fluorescence Detector

The Fluorescence Detector (FD) is comprised of four separate stations around the site area to look over the SD array: Los Leones, Los Morados, Loma Amarilla, and Coihueco (See Fig.2.1). Each station has six telescopes with a 30°× 30° field of view. The geometry and orientation of the telescopes at each eye provides 180° coverage in azimuth. Each telescope has a 3.8m^2 diaphragm positioned at the center of the curvature of an spherical mirror [23]. There is a UV transmitting filter installed at the aperture. It passes the light within 300-400nm wavelength band. This filter increases the signal to noise ratio. The fluorescence light comes from the nitrogen molecules excited by the low energy secondary particles of the air shower. The main emitted fluorescence light has discrete bands within 300 to 400nm wavelength (see figure 2.3).

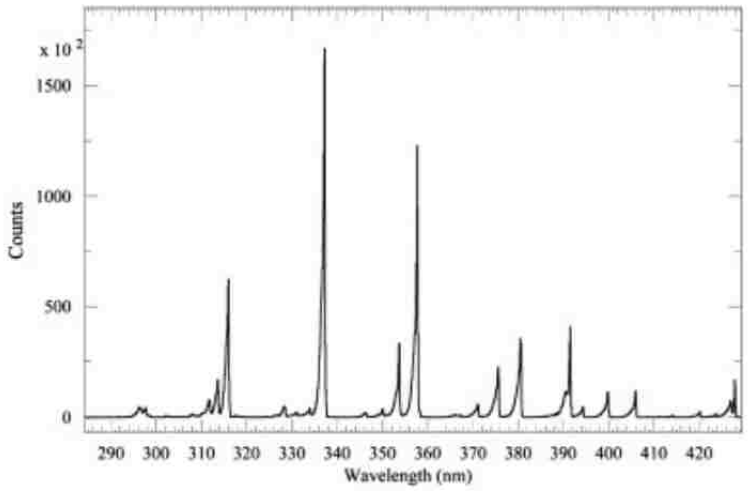

Figure 2.3: Measured fluorescence spectrum from exited nitrogen molecules.

The spherical mirror has 3.5m×3.5m dimensions (figure 2.4). The mirror is constructed from smaller hexagonal or nearly square shape segments. The average reflectivity of the segments was measured to be around 90% between 300 and 400 nm [23]. The focal surface of the mirror has a spherical shape. The light is focused on a PMT array camera located at the focal surface of the mirror [22]. Each array of 20×22 hexagonal PMT's acting as an extremely sensitive UV camera. The recorded signal is digitized every 100ns. If the signal could pass the triggers it will be sent to the data acquisition system.

2.3.1 FD Triggers

The ADC values for each pixel are recorded continuously. The first level trigger is when the sum of 10 consecutive ADC values pass an adjustable threshold. The event candidates should have at least five triggered pixels. The second level trigger is about the configuration of these five pixels. Each one of the five patterns shown in figure 2.5 is an acceptable configuration of the pixels. The third level trigger is much more complicated.

The shower geometry will be reconstructed for the candidates and the track length and space time compatibility requirements of the triggered pixels is cross checked with the reconstructed event. This technique helps to reject the pixels triggered due to the cosmic rays passing through the PMTs or other backgrounds [23].

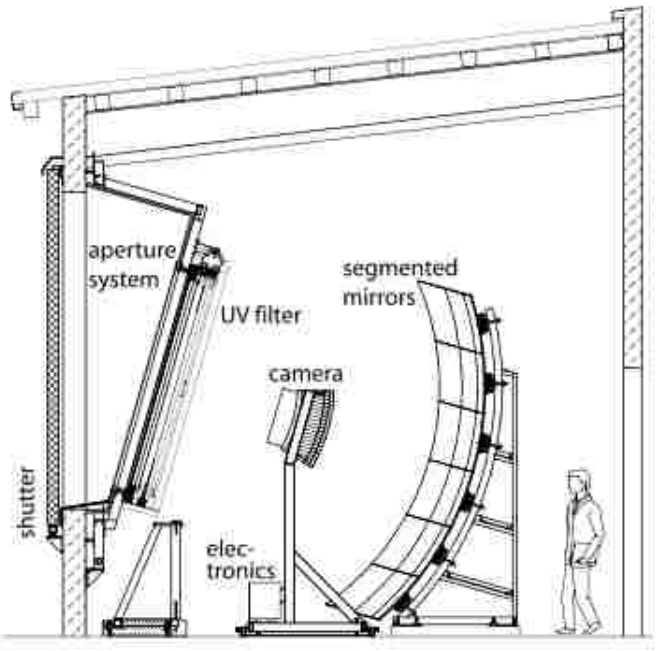

Figure 2.4: Schematic view of an FD eye at Pierre Auger Observatory.

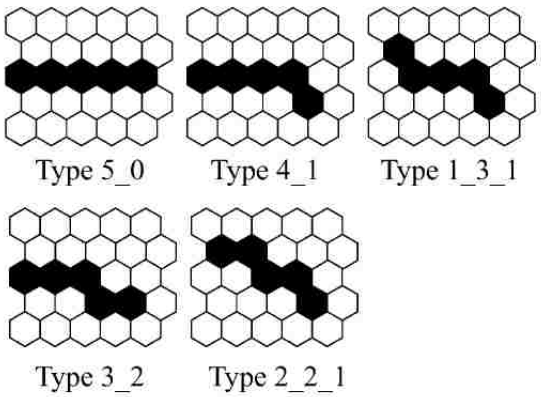

Figure 2.5: The acceptable patterns of the triggered pixels. Picture taken from [23].

2.3.2 Shower Axis Reconstruction

The detected light by PMTs and the timing of their detection can be used to reconstruct the shower geometry. First we need to find the plane that includes shower axis and the FD detector, known as SDP (shower detector plane).

Each FD pixel points to a specific direction in the sky. let $\mathbf{r}_i$'s be unit vectors with the directions of triggered pixels. In a perfect case, we expect that all these $\mathbf{r}_i$ vector lie on the

SDP. But in practice the SDP is estimated with minimizing the following quantity:

$$\chi^2 = \sum_i w_i [\mathbf{n}_{SDP}.\mathbf{r}_i]^2$$

where $\mathbf{n}_{SDP}$ is the SDP's normal vector, and the weight coefficient w_i is the measured signal for pixel $\underline{i}$.

After finding the SDP, the second step is to find the shower axis within the SDP plane. There is a small fraction of high energy events which is detected with more than one FD station. The shower axis for these events is the intersection of the two SDP's.

In order to find the shower axis with a single FD data, we need the t_i which is the corresponding time of recorded signal by the pixel i. We also need to determine the expected time t_i^{exp} for the detection. Based on the shower geometry (see figure 2.6)

$$t_i^{exp} = t_0 + R_p/c \, \tan[(\chi_0 - \chi_i)/2]$$

where R_p is the closest distance between FD and the shower axis, and t_0 is the time that shower front reaches to the R_p distance from the FD. χ_0 is the angle between shower axis and the ground plane within the SDP, and χ_i is the direction of the pixel i projected onto the SDP. The three parameters R_p, t_0 and χ_0 will be determined by minimizing the following quantity

$$\sum_i (t_i^{exp} - t_i)^2.$$

2.3.3 Longitudinal Shower Reconstruction

After reconstructing the shower geometry, the longitudinal shower profile can be reconstructed. For this purpose we need an atmosphere model to relate the shower track to the atmospheric depth X in g/cm^2. The atmosphere model details are discussed in section 4.2.1.

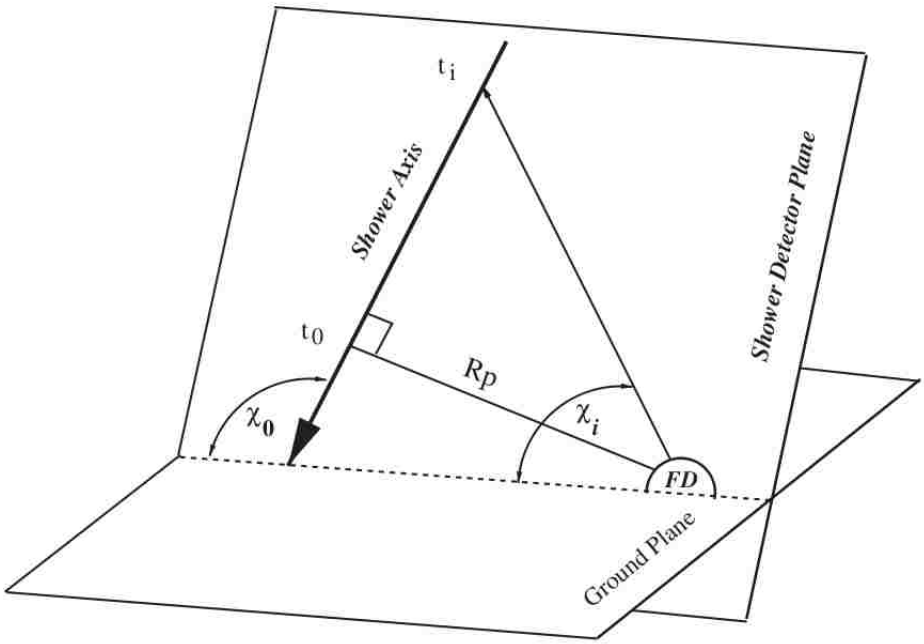

Figure 2.6: The shower geometry is illustrated here. Picture taken from [23].

The fluorescence light flux $S(X)$ received by the PMTs is approximated by:

$$S(X) = L(X)\frac{A}{4\pi r^2}\ c\ \delta t\ \epsilon\ T(r)$$

where $L(X)$ is the fluorescence light emitted isotropically from the source [24]. The emitted light $L(X)$ value is the product of fluorescence yield at the specific height $F_y(h)$ and number of the charged particles $N_e(X)$. A is the collection area (the involved pixels) and r is the observation distance. δt is the time that takes for shower to travel from X to X+δX (the corresponding distance viewed by detector in collection area A). ϵ is the detection efficiency and $T(r)$ is the transmission of the atmosphere which is related to the Rayleigh scattering in the atmosphere. The measured value for $L(X)$ is calibrated with the CLF laser shots. The measured value of $L(X)$ and the knowledge of fluorescence yield gives us an estimation from $N_e(X)$ (figure 2.7).

The high energy charged particles of air shower cause Cherenkov light radiation in the atmosphere. The main part of the emitted Cherenkov wavelength is within 300-400nm. So

the Cherenkov light contribution needs to be subtracted from the total light flux with an iterative procedure. The shower geometry and simulation is used to estimate the Cherenkov light fraction (see section 4.2 for more details).

The mean energy loss rate for electrons is $E^e_{loss} = 2.2MeV/(g/cm^2)$. The total deposited eneregy of the EM part of the shower is calculated by integration over the shower profile $E_{em} = E^e_{loss} \int N_e(X)dX$. otal energy of each shower has an invisible part E_{inv} which is the total energy of neutrinos and high energy muons that don't contribute to the emitted fluorescence light. The value of the E_{inv} is estimated using the simulation. So its value is model dependent and defers for proton and iron showers.

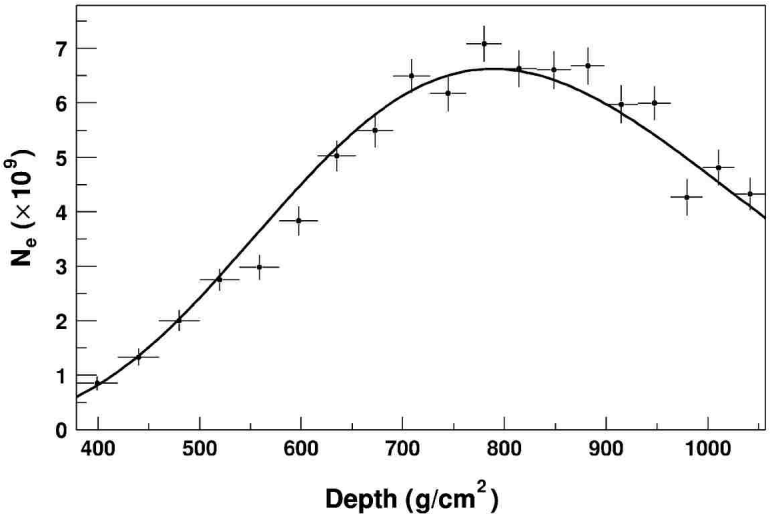

Figure 2.7: Longitudinal shower profile for an FD event fitted with Gaisser-Hillas function. Picture taken from [23].

2.4 Hybrid Events

The SD works with a 100% duty cycle, but the FD can only operate during clear moonless nights which provides an on average 10% duty cycle. So a small fraction of recorded air showers are recorded simultaneously by FD and one or more SD tanks (figure 2.8). These are called hybrid events.

The only difference in reconstruction of the hybrid showers is in finding the shower axis. Where the recorded time for the SD tank is applied to find the axis with more accuracy.

Because we use only the timing of the recorded SD data, so the threshold for SD trigger is smaller than what is explained in section 2.2.

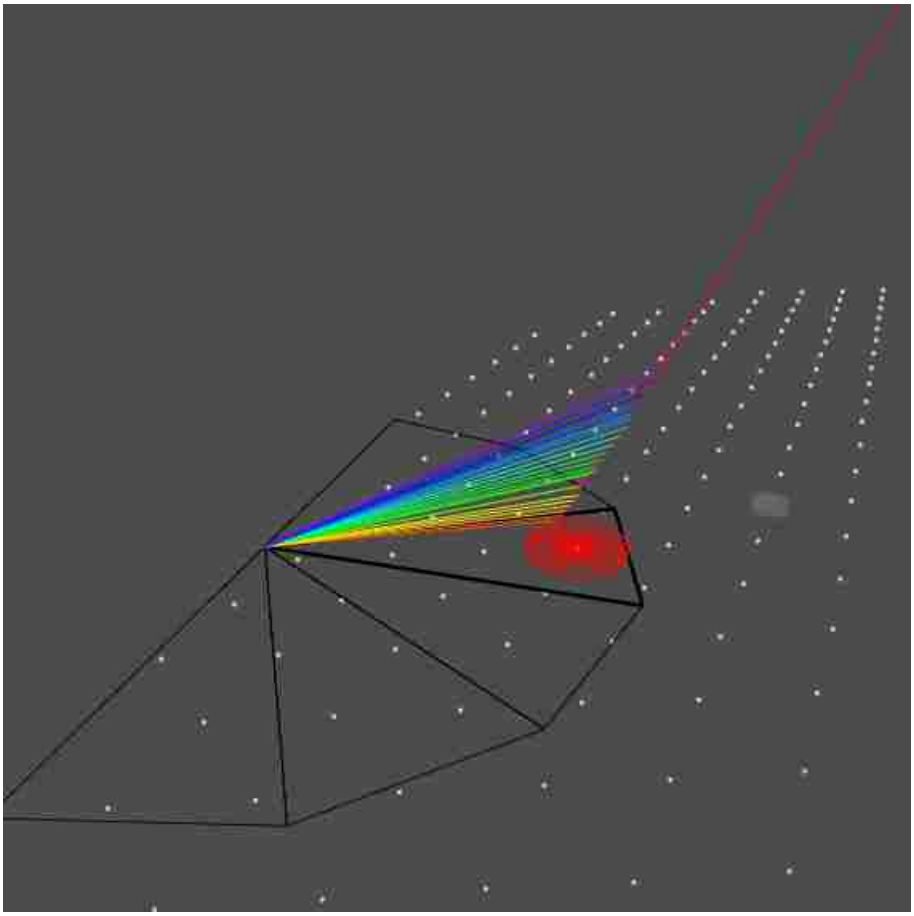

Figure 2.8: Geometric reconstruction of a hybrid event recorded by Loma Amarilla.

2.5 Atmospheric Aerosol and Cloud Monitoring

Like Cherenkov tanks that use water as detecting medium, the FD uses the atmosphere to trace the air showers. The fluorescence detection technique is particularly sensitive to the presence of aerosols and clouds, since they scatter the UV light from air showers. These aerosols are mainly dust. The main part of the monitoring system includes two laser shooting systems CLF and XLF. The FD detectors reconstruct the laser track like they do for air showers. The location, direction, wavelength an energy of the lasers are known. So the reconstructed data calibrates the detector, triggers, and the shower reconstruction. It also

helps to determine the atmospheric scattering properties and optical depth.

2.5.1 LIDARs

The LIDAR system (light detection and ranging) consists of 351nm pulsed lasers and mirrors that focus the back scattered light on PMTs (see figure 2.9). There is a LIDAR system near each of the FD stations. The lasers can point to different directions in the sky. The back scattered light can show the density of aerosols. It can also determine the existance and height of the nearby clouds. Because cloud back scatters the laser light significantly.

Figure 2.9: The LIDAR system with 3 mirrors that focus back scattered light on the PMTs. The box contains the high frequency laser. Picture taken from [25].

2.5.2 Cloud Camera

The are infrared digital cameras installed at each FD station. The images cover the spectral range between 7-14 μm. Each camera has FOV of $45^\circ \times 35^\circ$ and it is placed on a steerable mount to survey the entire sky. The cloud cameras that provide detailed all-sky map of cloud distributions each night (figure 2.10). Most of the information about clouds are gathered from the satellite images which is explained in section 4.1.

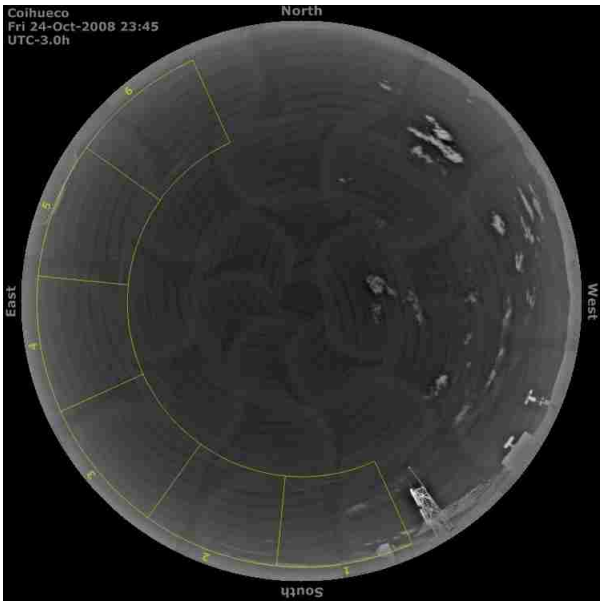

Figure 2.10: Cloud camera picture, 360° field of view.

3. Analysis

3.1 Leading Particle Physics

The collision of a high energy nucleon with a target nucleon is characterized by some energy being used to create new particles and the rest carried away by a single particle (figure 3.1).This secondary high energy particle is called the "Leading Particle" (LP). The fraction of energy carried by the LP is called the interaction elasticity. The leading particle effect describes the observation in a high energy nucleon-nucleon collision, there is a significant degree of elasticity [26]. The leading particle would carry off a large fraction of the total energy. If we don't consider the Leading Particle effect in longitudinal air shower development models, the air showers would rise and decay faster.

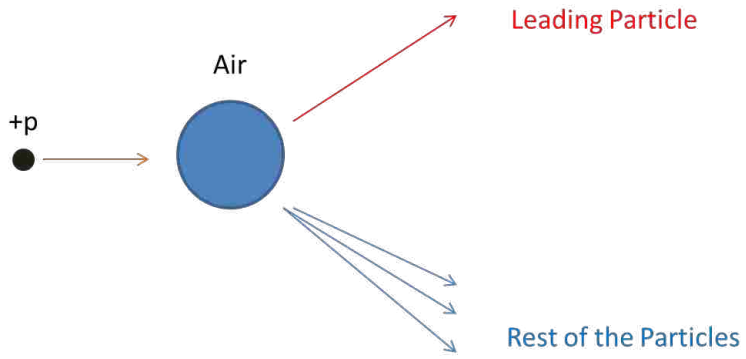

Figure 3.1: Schematic view of first interaction

The elasticity distribution for proton interactions at 10^{18} eV in simulations using the QGSJET-II [27] hadronic interaction model is shown in Figure 3.2. This shows the energy distribution of the LP from the first interaction.

In Fig.3.3 the type of leading particles that result from simulations of proton-air collisions at 1EeV are shown. The abundance of particles is based on the QGSJET-II model. Most of the LPs are protons, neutrons, or pions. The largest fraction are protons. Also the electron and gamma ray are rare leading particles.

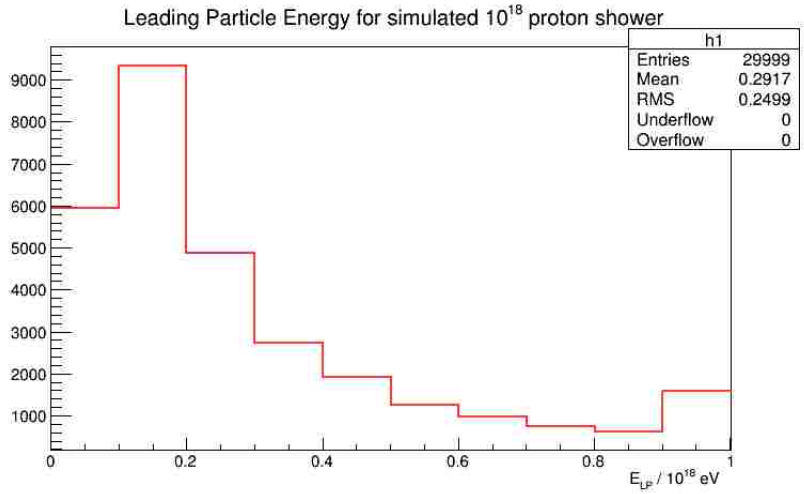

Figure 3.2: LP energy distribution from a proton primary with an energy of 10^{18} eV using CONEX [28] and the QGSJETII hadronic interaction model.

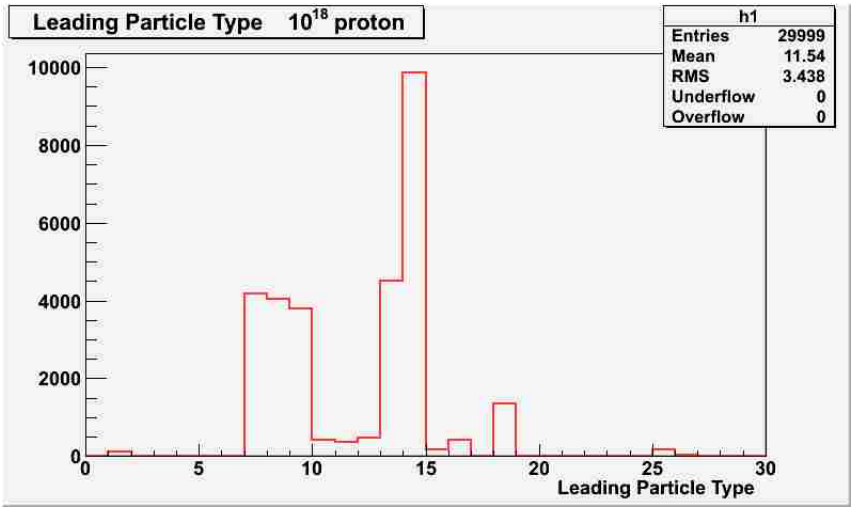

Figure 3.3: LP type from a proton primary with an energy of 10^{18} eV using CONEX and the QGSJET-II hadronic interaction model.

1	2	7	8	9	10	11	12	13	14	15	16	18	25	26
γ	e^+	π^0	π^+	π^-	K_L^0	K^+	K^-	n	p	$\overline{p}$	K_S^0	Λ	$\overline{n}$	$\overline{\Lambda}$

The leading particle traverses a distance $X_1(LP)$ from the first interaction position (where it has been generated) up to its interaction point with another air molecule. The fluctuation of $X_1(LP)$ has a specific exponential distribution which depends on the particle cross-section with air. Figure 3.4 is a histogram of the $X_1(LP)$ for leading particles of all types and energies which are generated from a primary proton with energy 10^{18}eV striking an air

molecule. The π^0 leading particles are eliminated from this histogram because they decay very fast. The leading particle distribution exhibits an exponential distribution on average. The fitted interaction length value is dominated by p,n with $\lambda \approx 48$ g/cm^2 and π^+,π^- with $\lambda \approx 58$ g/cm^2 (based on QGSJET-II model).

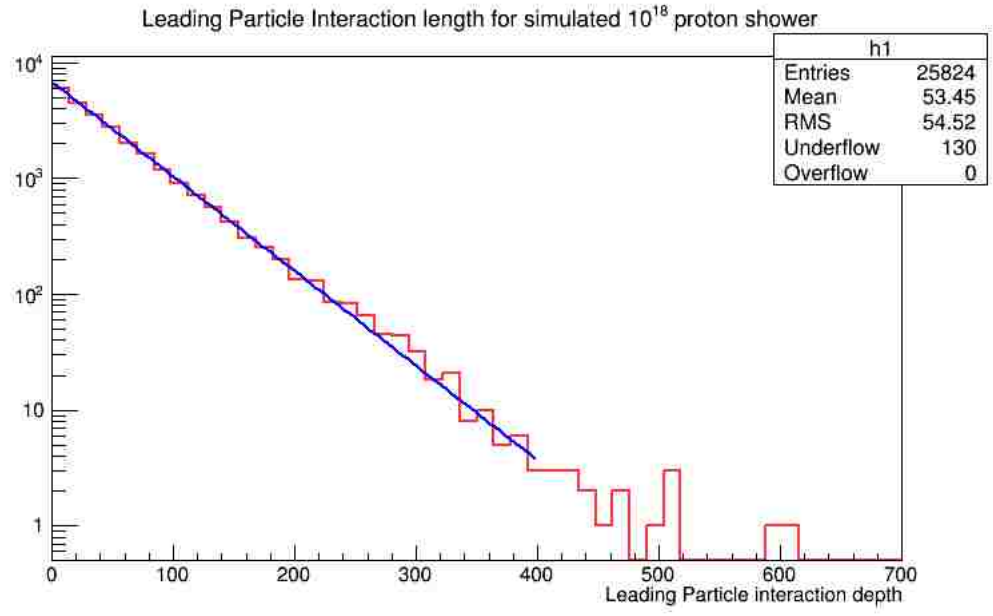

Figure 3.4: Interaction depth of the leading particles (except for π^0) for simulated proton air showers at E=10^{18}eV. The histogram fit function is $A\ exp(-x/\lambda)$. the best fit value for λ is 53 g/cm^2.

3.2 Basic Model

Ultra-high energy cosmic rays initiate extensive air showers in the atmosphere. Simulations indicate that showers will very rarely exhibit two distinct shower maxima (Figure 3.5). We call these irregular air showers as "Double-Bump" showers. This feature can arise if there are two air showers superimposed : one from the initial interaction and second from the interaction of the LP of the first interaction, provided the LP has reasonably large energy and long interaction depth.

In this example (figure 3.5), the LP has nearly half the energy of its parent, and it has traveled a long distance (420 g/cm^2) before it collides with air. The leading particle generates its own shower. The rest of the secondary particles that came out of the first

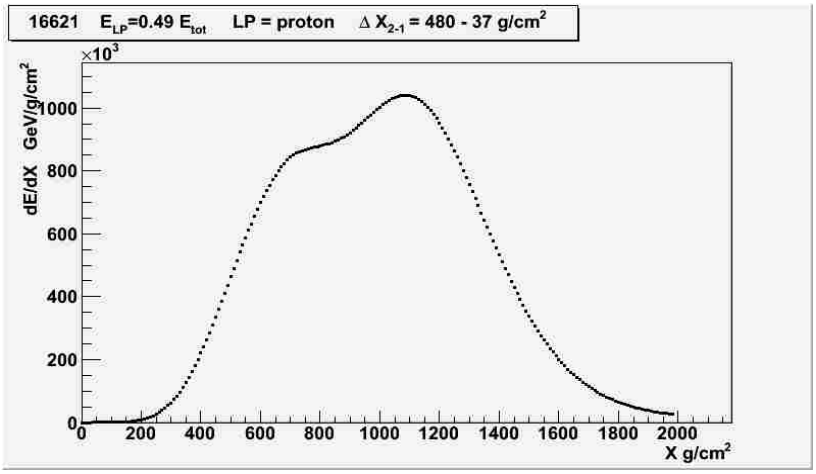

Figure 3.5: A simulated air shower from a proton primary with energy $E = 10^{18}$ eV. The LP of the first interaction is a proton with $E = 0.49 \times 10^{18}$ eV that penetrated 440 g/cm^2 into the atmosphere

interaction constitute their own shower. The whole air shower is the superposition of these two sub-showers. If the LP penetrates deep into the atmosphere before interacting, these two sub-showers become sufficiently separated that the total shower would have a double bump structure.

The average growth of the number of charged particles with depth in the atmosphere is well described by both the semi-empirical Gaisser-Hillas function and by the Gaussian Function in Age (GFA). The combination of two well separated GFA functions is plotted in the figure 3.6. The red sub-shower is the one generated by the leading particle. The observed shower is the combination of the two sub-showers. The similarity between figures 3.5 and 3.6 is in agreement with expectations from consideration of leading particle effect.

The X_{max} position of an air shower is the addition of the depth of first interaction X_1 of the primary and the subsequent shower development Δ (see figure 3.7). Fluctuations in X_{max} results from the fluctuations both in X_1 and in Δ. The depth of first interaction has an exponential distribution which is a characteristic of the primary particle cross-section with air. The subsequent shower development is a combination of many particles, so it is expected to have a normal (gaussian) distribution [30]. This description in terms of X_1 and

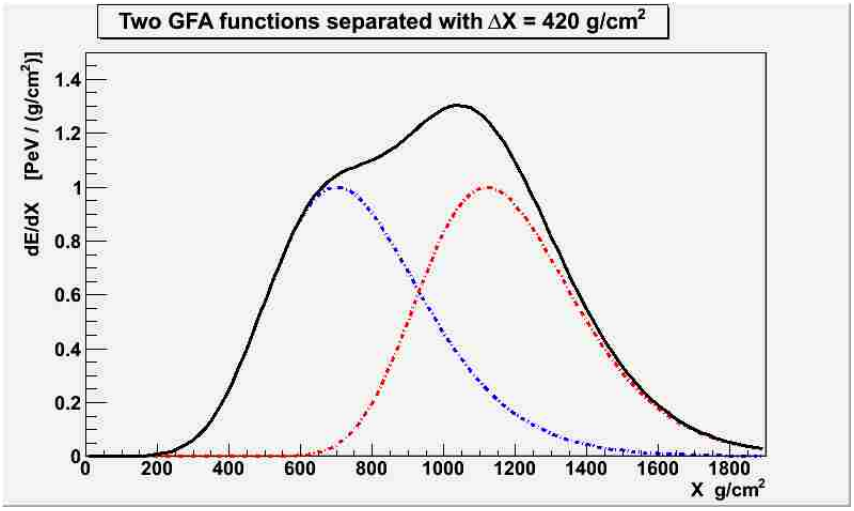

Figure 3.6: Addition of two GFA functions with 420g/cm^2 separation.

Δ applies to the sub-showers too.

$$X_{max}1 = X_1 + \Delta \tag{3.1}$$

$$X_{max}2 = X_1 + X_1(LP) + \Delta(LP) \tag{3.2}$$

$$\Delta X = X_{max}2 - X_{max}1 = X_1(LP) + \Delta(LP) - \Delta \tag{3.3}$$

In figure 3.8, the shower maximum depth ($X_{max}1$) of the first sub-shower (blue) is separated into X_1 and Δ components (equation 3.1). Also the shower maximum depth ($X_{max}2$) of the second sub-shower (Red), which is generated by the leading particle, is separated into $X_1(LP)$ and $\Delta(LP)$ as well (equation 3.2). The X_{max} separation of the two sub-showers (ΔX) depends on $X_1(LP)$, $\Delta(LP)$ and Δ (equation 3.3). The RMS value of $X_1(LP)$ and $\Delta(LP)$ distributions are almost the same [29]. It could be assumed roughly that The distribution of Δ is not much different from $\Delta(LP)$. In order to find out what does ΔX distribution may looks like, one exponential and two gaussian distributions which represent the $X_1(LP)$, $\Delta(LP)$ and Δ respectively are combined (figure 3.9). The important feature of the ΔX distribution in figure is its exponential tail. The fitted function on the tail region determines that it has same the exponential distribution as the $X_1(LP)$. So if we could find

the ΔX for a large set of air showers, then we can determine the $X_1(LP)$ distribution which corresponds to LP cross-section with air.

The LP energy in such irregular showers is comparable to energy of the parent ultra-high energy primary. There is not much knowledge about hadronic physics at this energy level because it is far beyond the available energy at accelerators like LHC. Air shower simulations must extrapolate hadronic interaction models from lower energies. I will discuss later that the ΔX could be determined in auger FD data if the two sub-showers are well separated. The superposition of these two separated sub-showers will make an irregular shape compared with an average shower. So the purpose of my work is to study irregular air showers to find the leading particle cross-section.

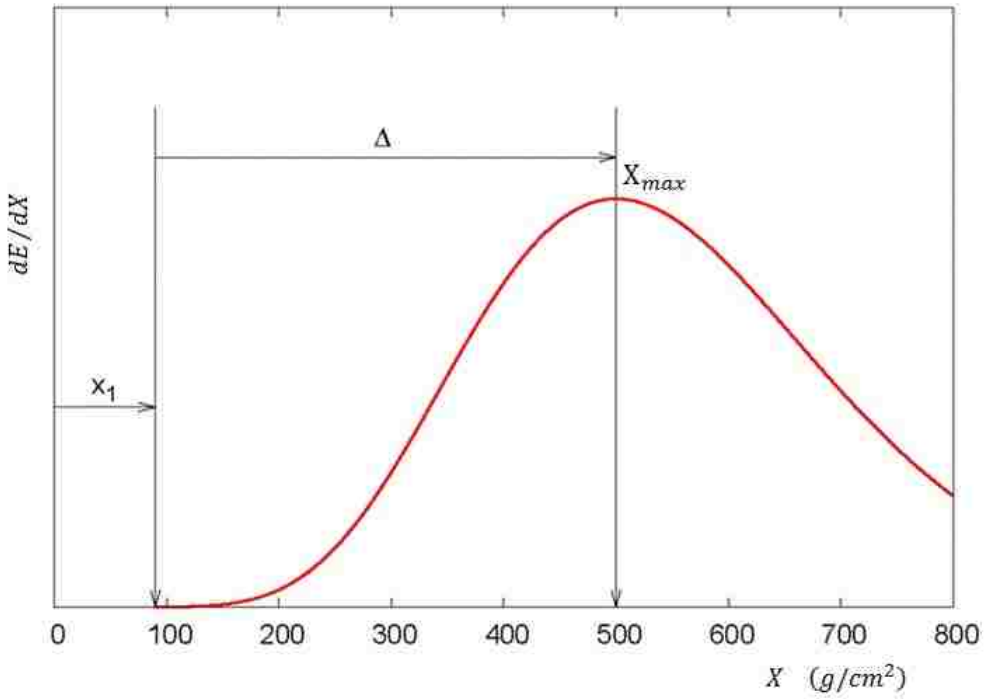

Figure 3.7: The first interaction occurs at point X_1, the development from this point to shower maximum occurs over a length Δ. picture taken from [29].

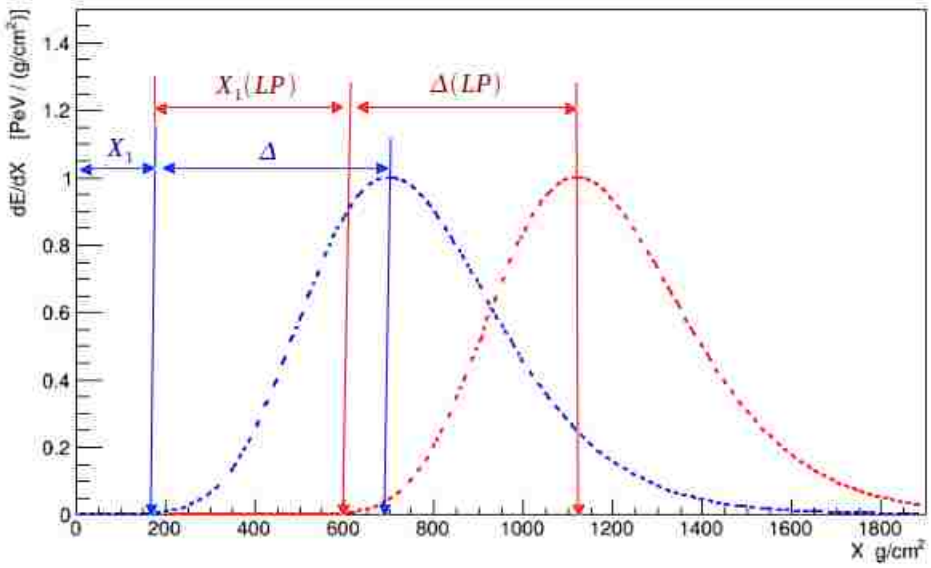

Figure 3.8: Shower maximum depth of each sub-shower is divided to X_1 and Δ. X_1 is first interaction depth of the primary cosmic ray. $X_1(LP)$ is the interaction depth of leading particle, measured from the X_1 depth. Δ and $\Delta(LP)$ are the subsequent shower developments of each sub-shower.

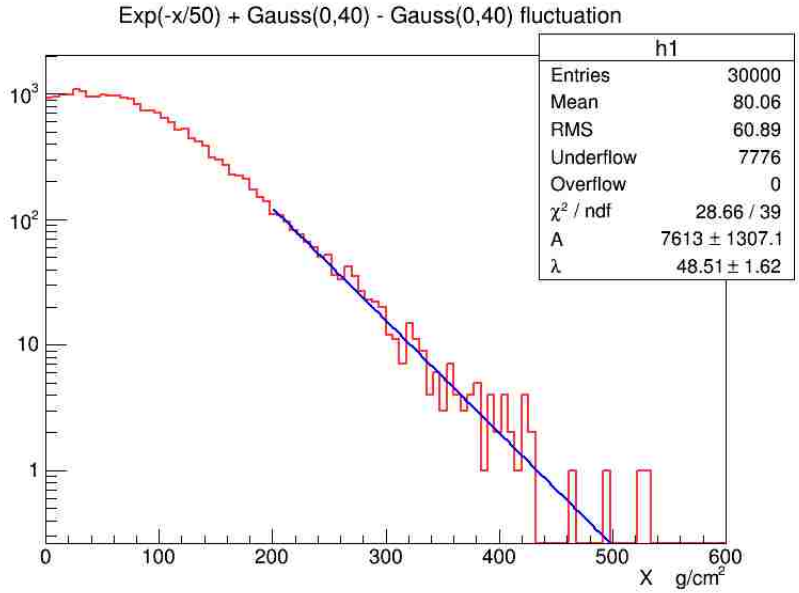

Figure 3.9: Convoluted distribution of three distributions Exp(-x/50) + Gauss(0,50) - Gauss (0,40). The Exp(-x/50) and Gauss(0,50) are rough guesses for $X_1(LP)$ and $\Delta(LP)$ distributions. Gauss(0,40) is also a rough guess for Δ distribution.

3.3 Fit Methods

3.3.1 Gaisser-Hillas Function

The longitudinal profile of an air shower is often parameterized by the semi-empirical Gaisser-Hillas function (figure 3.10) [31].

$$N(x) = N_{max}\left(\frac{x - X_0}{X_{max} - X_0}\right)^{\left(\frac{X_{max}-X_0}{\lambda}\right)} \exp\left(\frac{X_{max} - x}{\lambda}\right) \tag{3.4}$$

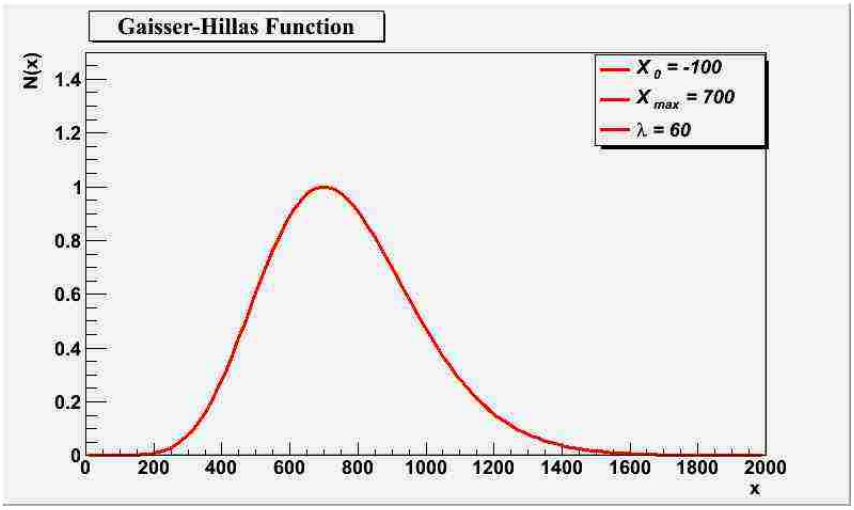

Figure 3.10: A normalized Gaisser-Hillas Function with parameters: $X_0 = -100,\ X_{max} = 700,\ \lambda = 60$

where N_{max} and X_{max} are maximum number of particles and the slant depth at shower maximum respectively. This formulation for fitting the shower profiles has some technical disadvantages. The X_0 and λ are correlated fit parameters. Also the X_0 fitted value depends on the fitting interval (it always lies outside the interval).

In order to find the two sub-showers, two of these Gaisser-Hillas functions should be fitted to the shower profile. So there are eight parameters to fit. If we could reduce the number of fit parameters and make each pair uncorrelated, it would be a big advantage. All these problems made us search for another fit function that works better for our purpose.

3.3.2 Gaussian Function in Age (GFA)

Shower profiles could be plotted as a function of age $S(x)$ instead of slant depth X [32]. The age is defined by:

$$S(x) = \frac{3x}{x + 2X_{max}}.$$

This age transformation fixes any shower maximum depth at $S = 1$. The shower profiles in age are highly symmetric (figure 3.11). A gaussian function in age (GFA), with the mean at S=1 is a good parametrization for the air showers [33].

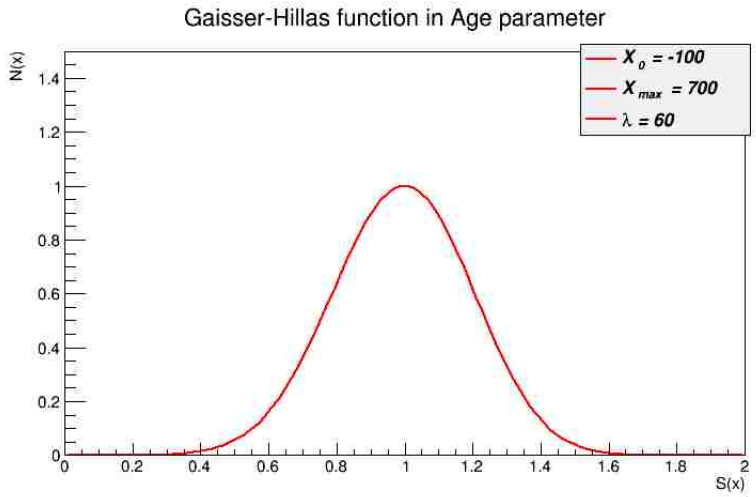

Figure 3.11: The same Gaisser-Hillas function plotted in figure 3.10,here is parameterized in age $S(x)$. Its shape is close to a gaussian function.

$$N(s) = N_{max} \exp\left[\frac{-1}{2\sigma^2}(s-1)^2\right]$$
$$N(x) = N_{max} \exp\left[\frac{-2}{\sigma^2}(\frac{x - X_{max}}{x + 2X_{max}})^2\right] \tag{3.5}$$

where σ is the width of the shower profile. The Gaussian function with age parameter can be transformed to the slant depth X again. It has three fit parameters N_{max} , X_{max} and σ. These three parameters are uncorrelated. Figure 3.12 shows a GFA function which looks very similar to the Gaisser-Hillas function in figure 3.10.

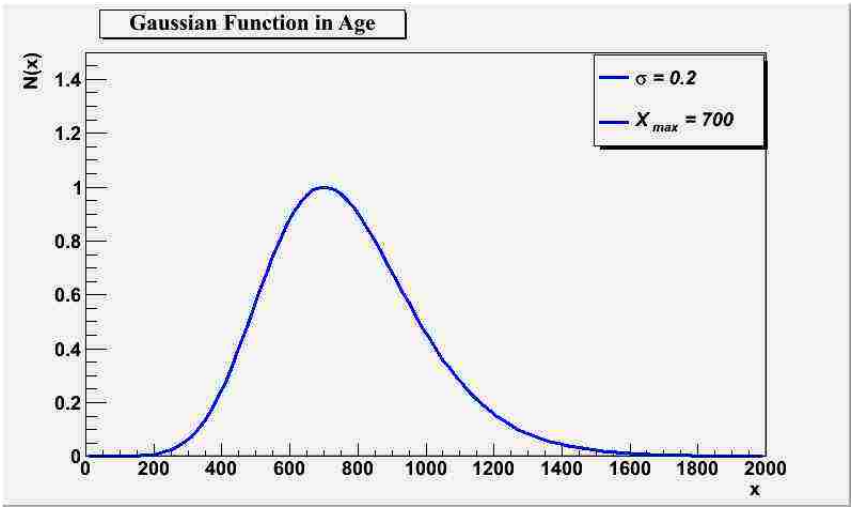

Figure 3.12: A normalized GFA Function with parameters: $\sigma = 0.2,\ X_{max} = 700$

In order to find the two sub-showers, two of these GFA functions should be fitted to the shower profile (Two-GFA). Here we have six parameters to fit. The Two-GFA fit parameters are $N_1, N_2, \sigma_1, \sigma_2, X_{max}, \Delta X$. The width parameters σ_1, σ_2 are constrained with limits. The parameter ΔX is the shift of the second GFA function with respect to the first one.

$$N(x) = N_1 \exp\left[\frac{-2}{\sigma_1^2}(\frac{x - X_{max}}{x + 2X_{max}})^2\right] + N_2 \exp\left[\frac{-2}{\sigma_2^2}(\frac{x - \Delta x - X_{max}}{x - \Delta x + 2X_{max}})^2\right] \tag{3.6}$$

3.3.3 Energy Dependence of GFA Fit Parameters

The energy dependence of the three GFA fit parameters is studied with simulated air showers. A large set of proton air showers is simulated at specific energies from 10^{17}eV to 10^{19}eV with the CONEX code and the QGSJET-II model. The GFA function is fitted on the simulated shower profiles (see table 3.1) using the ROOT fit package [34]. We use deposited energy per slant depth $(dE/dX)_{max}$ instead of the number of particles N_{max}, because the Auger reconstructed shower profiles are based on the deposited energy per slant depth. The deposited energy is expected to be proportional to N with high accuracy.

The $(dE/dX)_{max}$ has linear dependence to shower energy (see figure 3.13). But both X_{max} and σ are linearly dependent to logarithm of shower energy (figures 3.14 and 3.15).

Table 3.1: Energy Dependence of GFA Fit Parameters. Average and RMS values for the fitted parameter distributions.

log(E/eV)	$(dE/dX)_{max}$ ($\frac{\text{PeV}}{\text{g/cm}^2}$)	RMS $(dE/dX)_{max}$	X_{max} (g/cm^2)	RMS (X_{max})	σ	RMS (σ)
17	0.16	0.01	666	60	0.21	0.0181
17.2	0.253	0.014	682	65	0.207	0.0176
17.4	0.4	0.02	693	65	0.205	0.0165
17.6	0.64	0.031	701	63	0.203	0.0162
17.8	1.01	0.048	711	61	0.202	0.0152
18	1.6	0.07	724	64	0.2	0.015
18.2	2.53	0.11	732	58	0.198	0.014
18.4	4	0.16	739	60	0.197	0.014
18.6	6.33	0.23	749	56	0.196	0.013
18.8	10	0.36	757	55	0.194	0.128

The two-GFA function does fit properly on the Auger shower profiles if σ_1 and σ_2 have limited ranges. Otherwise, sudden peaks or gaps in profile data points could affect the fit severely. The figures 3.16 and 3.17 show the σ distributions for simulated proton showers at 10^{17}eV and 10^{18}eV using a one-GFA fit. Based on these distributions we have set the σ range in the fits to be $[0.16, 0.26]$.

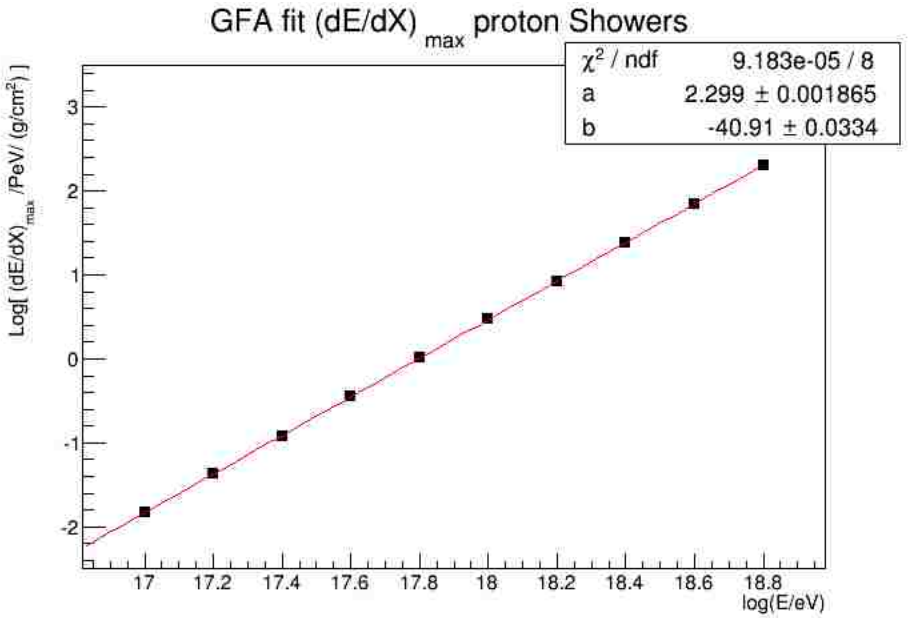

Figure 3.13: The energy dependence of $(dE/dX)_{max}$. RMS values are too small to be viewed on this plot.

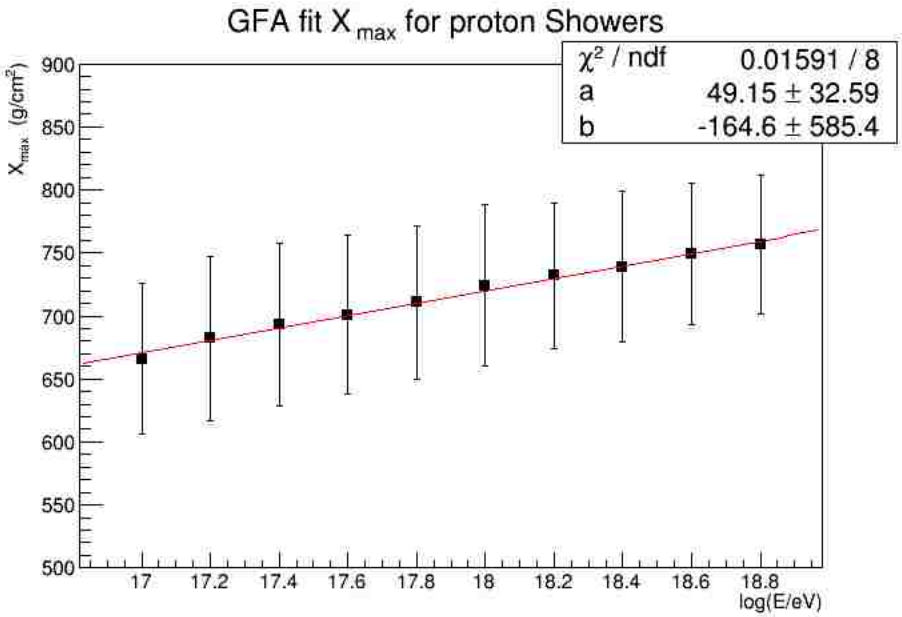

Figure 3.14: The energy dependence of mean X_{max}. The slope of this fitted line is known as the elongation rate. Bars show the RMS spread of X_{max}'s.

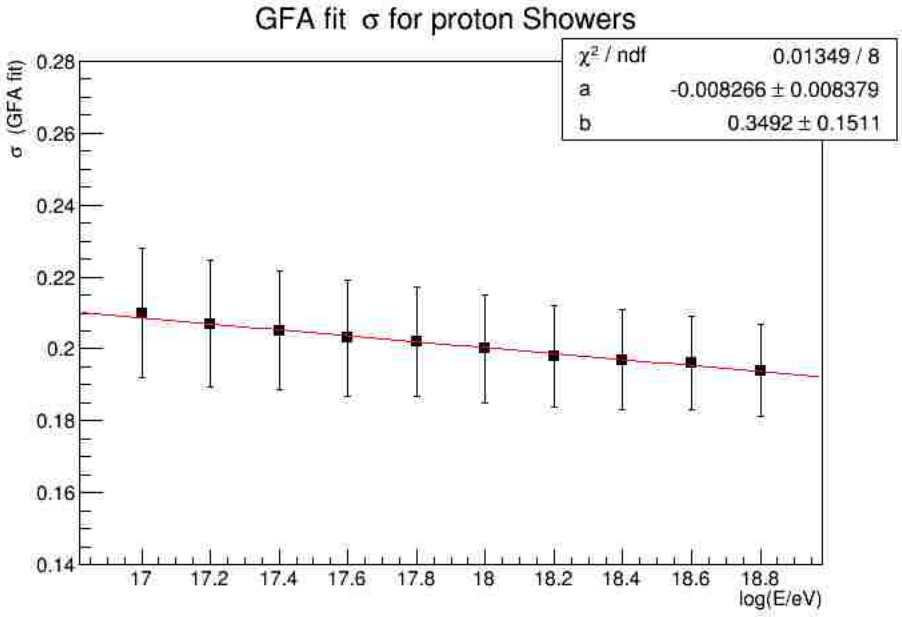

Figure 3.15: The energy dependence of mean σ. Bars show the RMS spread of points.

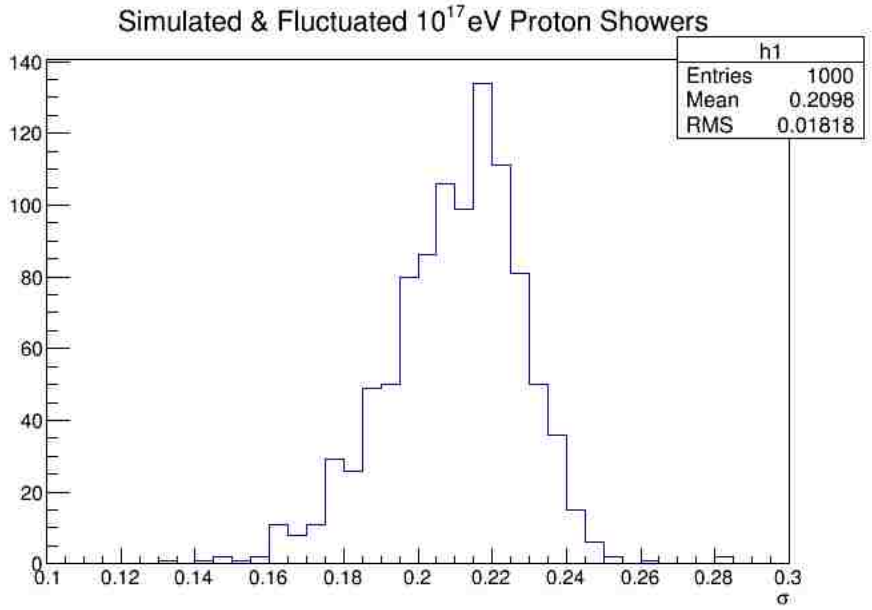

Figure 3.16: Distribution of the σ for the one-GFA fit on simulated proton air showers at 10^{17}eV.

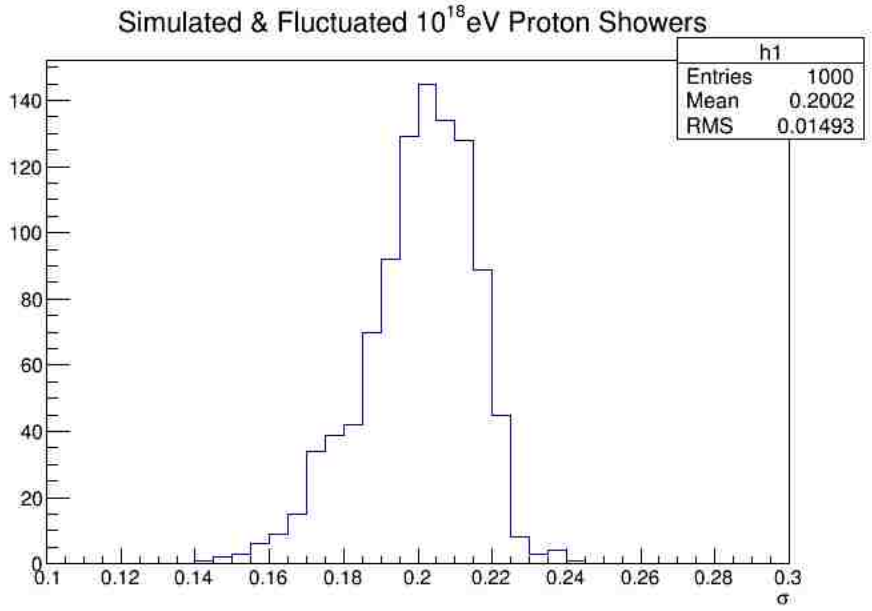

Figure 3.17: Distribution of the σ for the one-GFA fit on simulated proton air showers at 10^{18}eV.

3.3.4 Imposed Fluctuations in Simulated Shower Profiles

Simulated shower profiles generated by CONEX do not possess measurement fluctuations, whereas an observed shower profile does due to atmospheric properties and FD detection uncertainties. We will impose uncertainties on the simulation points derived from parametrization of the error bars in real data. Figure 3.18 shows a reconstructed shower profile of an Auger event with the error bar on each data point. The size of these error bars depends on many parameters like the uncertainty in fluorescence yield coefficient, atmospheric scattering and attenuation, detector efficiency, etc. These error bars also have some interesting characteristics in common. For example, the average value of the error bars in a shower profile with the distance R_p of the shower from the FD (see figure 3.19). Also have correlation with the deposited energy values in a shower profile (see figure 3.20).

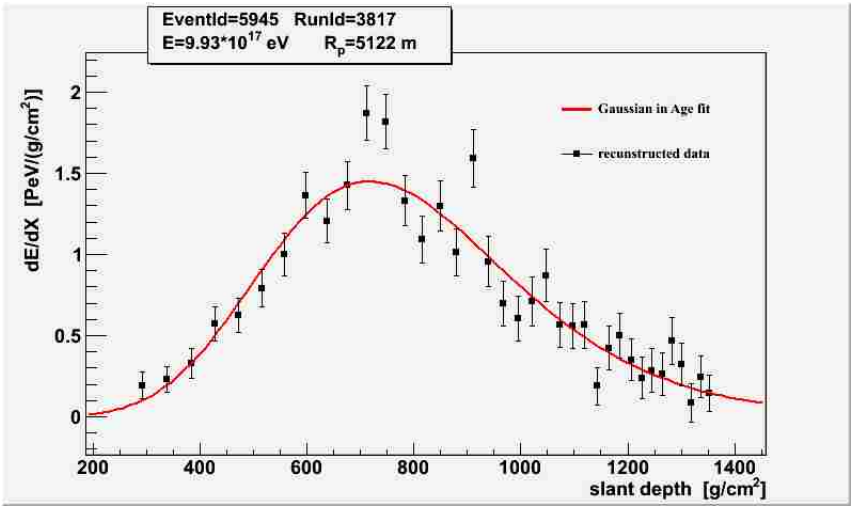

Figure 3.18: Reconstructed shower profile for an actual observed air shower. The air shower energy is $E = 9.93 \times 10^{17}$ eV and R_p=5.1 km.

Figure 3.20 shows the size of the error bars versus the magnitude of the deposited energy for each data point at the shower profile shown in figure 3.18. There is an almost linear relationship between the deposited energies and their error bars for each shower. The slope (A) and y-intercept (B) look to be dependent to the shower energy and its distance from an FD eye R_p.

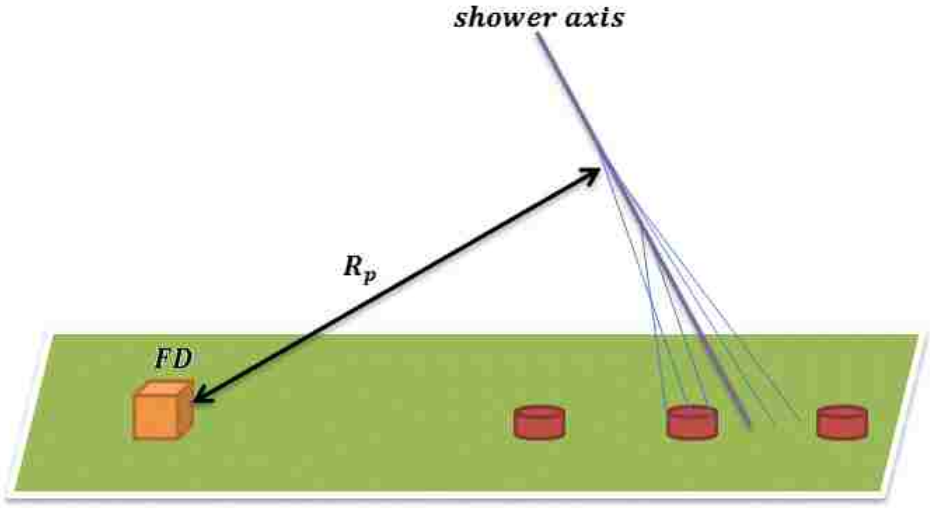

Figure 3.19: R_p is the distance between an FD eye and the shower axis.

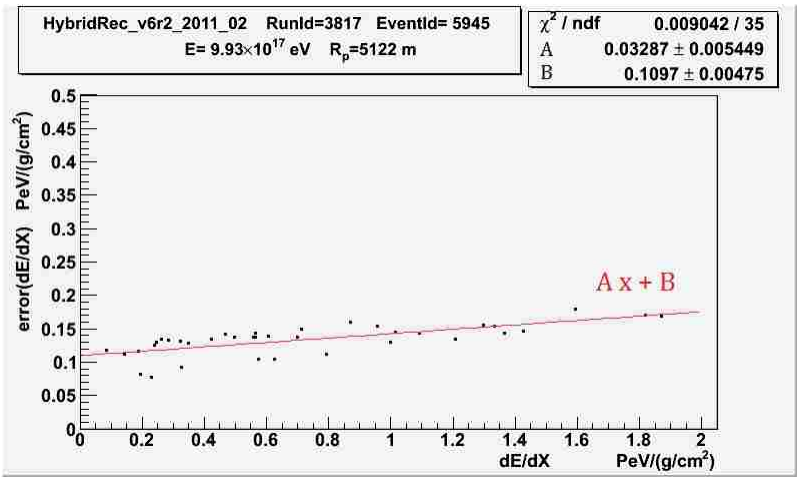

Figure 3.20: $\sigma(\frac{dE}{dX})$ vs. $(\frac{dE}{dX})$ for the shower profile in figure 3.18.

$$\sigma(\frac{dE}{dX}) = A(E, R_p)\frac{dE}{dX} + B(E, R_p) \tag{3.7}$$

Many showers with energy $E = 1.0 \pm 0.1[EeV]$ are selected from the Auger data and the fitted values for A and B are determined. The coefficient A and the distance R_p have a linear correlation (figure 3.21), and Figure 3.22 shows the B parameter dependence to the distance R_p is a power law.

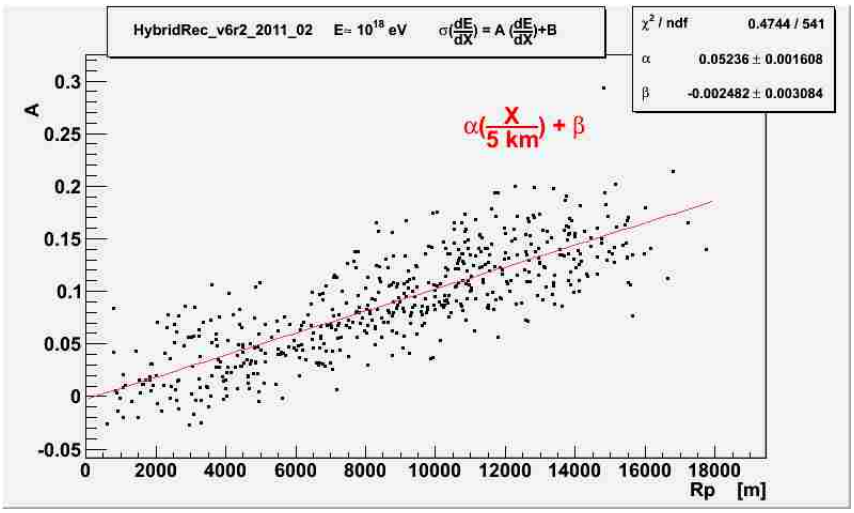

Figure 3.21: $A(1.0\ EeV, R_p)$ vs. R_p have an increasing linear relation. Selected events have $E = 1.0 \pm 0.1\ [EeV]$ fitted with linear function $\sigma(\frac{dE}{dX}) = A\frac{dE}{dX} + B$

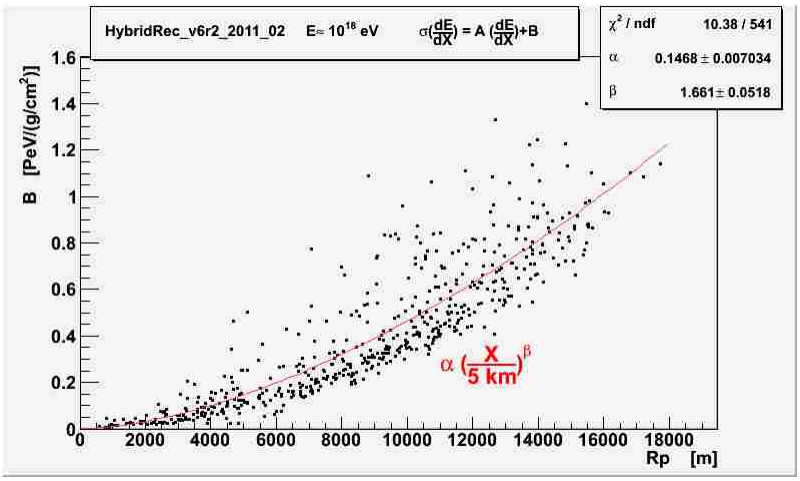

Figure 3.22: $B(1.0\ EeV, R_p)$ vs. R_p have an increasing power law relation. Selected events have $E = 1.0 \pm 0.1\ EeV$ fitted with linear function $\sigma(\frac{dE}{dX}) = A\frac{dE}{dX} + B$

The average R_p dependence of the A and B parameters for 10^{18}eV air showers

$$A(1EeV, R_p) \approx 0.05(\frac{R_p}{5km}) \tag{3.8}$$
$$B(1EeV, R_p) \approx 0.14(\frac{R_p}{5km})^{1.6} \ \ \mathrm{PeV/(g/cm^2)}.$$

These relations are implemented to generate fluctuations for simulated air shower profiles. This allows for simulated events to appear similar in form to real observed events with

$R_p = 5km$ distance. For this purpose, each point would be fluctuated according to a gaussian smearing centered at the simulated dE/dX and the gaussian width equal to the error bar $\sigma(dE/dX)$ on the point. Fig.3.23 shows the result of smearing the data points of a simulated 10^{18}eV proton shower.

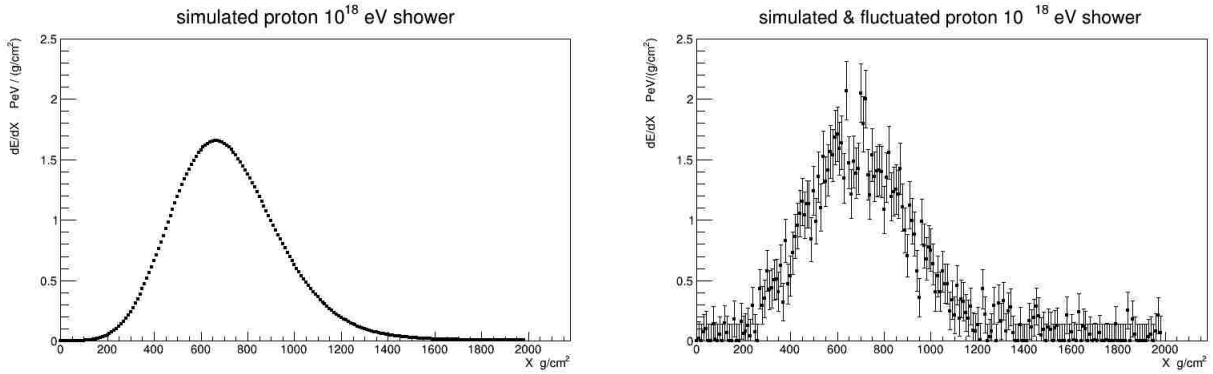

(a) A pure simulated shower.

(b) The same shower with fluctuations.

Figure 3.23: Comparison between original and fluctuated versions of a simulated air shower.

3.3.5 2 Added Air Showers

The efficiency and behavior of two-GFA function fit on air showers can only be evaluated using simulations. We will make double-bump showers by superimposing two simulated "ordinary" air showers - those that are simply typical proton-induced air showers. These simulated showers are primary protons with energy E=10^{18}eV, and they include fluctuations based on the average error bars for showers with E=10^{18}eV and R_p=5km. Figure 3.24 shows the first shower fitted with a GFA function. The second shower has been uniformly shifted in depth by discrete increments of 50 g/cm^2 (i.e., shifts of 0, 50, 100,..., 550, 600 g/cm^2).

These two showers are simply added together to mimic the two sub-showers in a double bump air shower. The so-called "actual" separation ΔX(input) between the two showers is defined as the difference between a one-GFA fit of each shower individually:

$$\Delta X(input) = X_{max}(2^{nd} shower) - X_{max}(1^{st} shower).$$

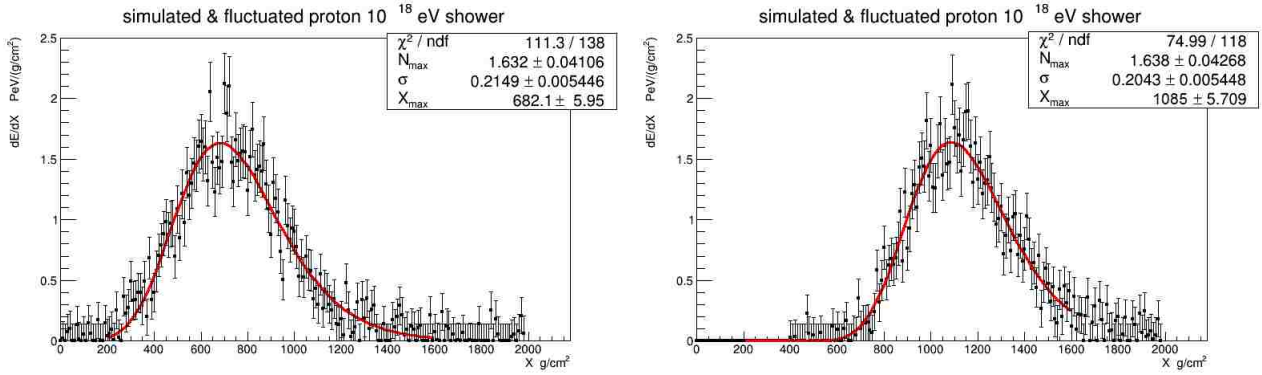

(a) 1^{st} shower (b) 2^{nd} shower is shifted 400 g/cm^2

Figure 3.24: Two simulated and fluctuated proton showers. The 2^{nd} shower profile is shifted in depth.

The one-GFA and two-GFA functions are fitted to these added showers, and the reduced χ^2 of one-GFA fit ($\chi^2(1GFA)$) is compared with the reduced χ^2 of two-GFA fit ($\chi^2(1GFA)$). We want to know how well can the fitted two-GFA function resolve the 2 added showers and their separation. Also we should find out if fitting the two-GFA function improves the fit result (reduced χ^2 of the fit). The fit results in figure 3.25 and 3.26 show a 40% improvement in the χ^2 fit result. The two-GFA fit has underestimated the separation between the 2 added showers.

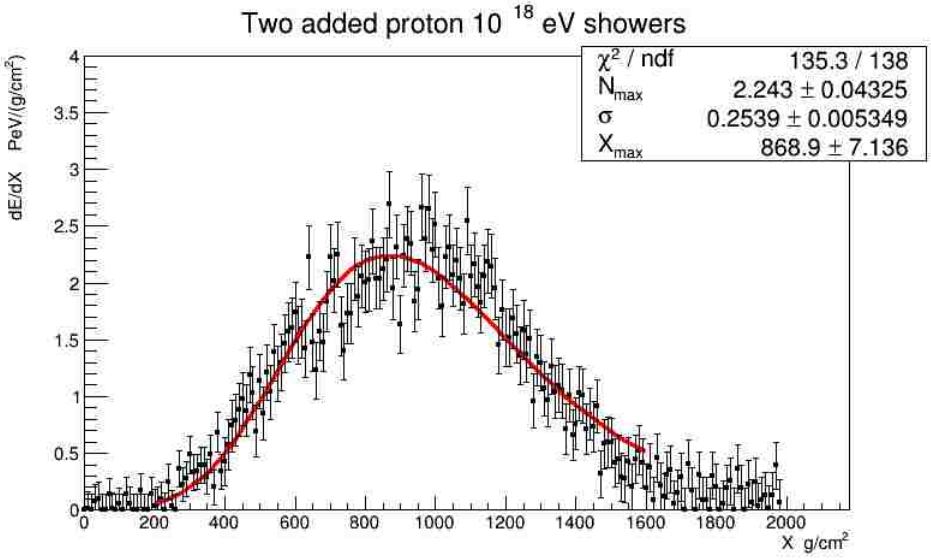

Figure 3.25: One-GFA fit one the 2 added showers

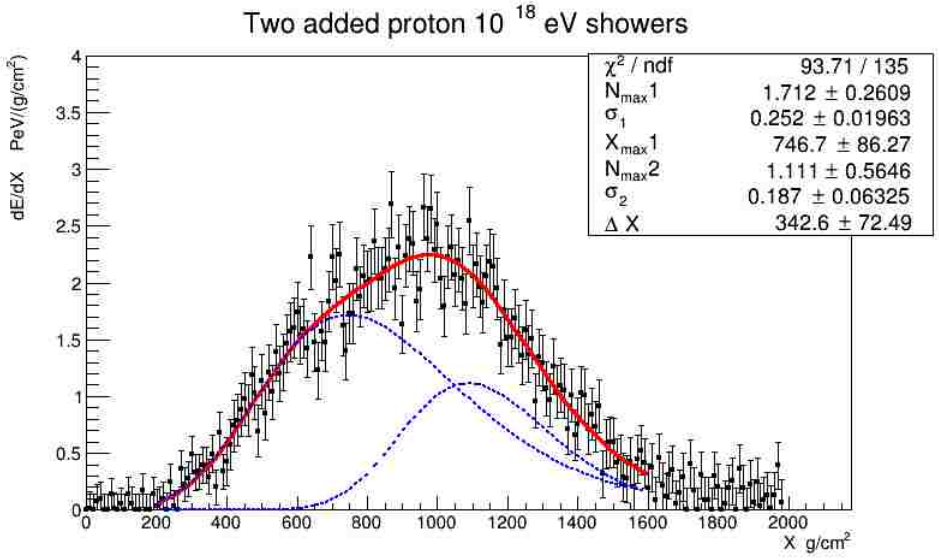

Figure 3.26: The two-GFA function (red) fit on the 2 added showers. The blue curves are the constituents of the two-GFA fit result.

The actual separation in this example is $\Delta X(input) = 403 g/cm^2$, the two-GFA fit finds just $\Delta X(input) = 342 g/cm^2$ separation. Also, the 2 added showers have almost the same value of N_{max}, but the fit finds the N_{max} of the first shower ($N_{max}1$) 50% larger than the second one ($N_{max}2$).

Figure 3.27 shows the reduced χ^2 ratio between the two-GFA and one-GFA fits on a large sample of the 2 added showers. The two-GFA fit improves (reduced χ^2 value) as the separation between the 2 added showers becomes larger. This χ^2 difference between one-GFA and two-GFA functions is a key factor that can help us to identify irregular air showers. In figure 3.28 we see the two-GFA fit finds the right separation value ($\Delta X(2GFA\ fit)$) for the events with large $\Delta X(input)$. The fit tends to overestimate the separation value for small $\Delta X(input)$ values. All the fit results presented in this plot have smaller χ^2 with two-GFA fit than the one-GFA fit.

Based on the figure 3.27, if we impose a harder cut on the $\chi^2(1GFA)/\chi^2(2GFA)$ ratio only the events with large $\Delta X(input)$ value will survive. The χ^2 ratio cuts are set to be 1.1 and 1.2 in figures 3.29 and 3.30 respectively. The higher cut value eliminates most of the events with small separation values ($\Delta X(input) < 200$ g/cm^2). These are the events that

the two-GFA fit tends to find a wrong separation value for them.

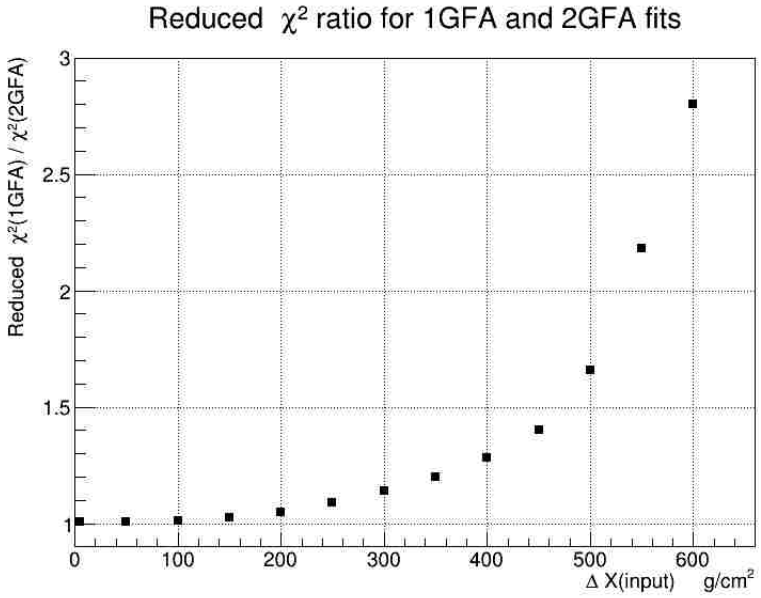

Figure 3.27: The reduced χ^2 ratio between one-GFA and two-GFA fits versus the separation between the 2 added showers. The errors are too small to be seen on this plot.

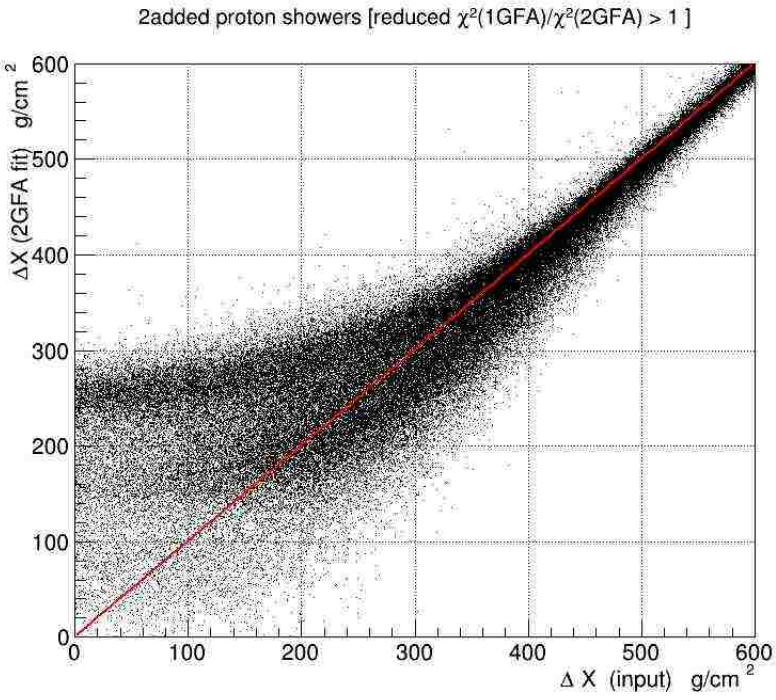

Figure 3.28: The separation that the two-GFA fit finds vs. the actual separation of the 2 added showers. These are the fit results with reduced $\chi^2(1GFA) > \chi^2(2GFA)$.

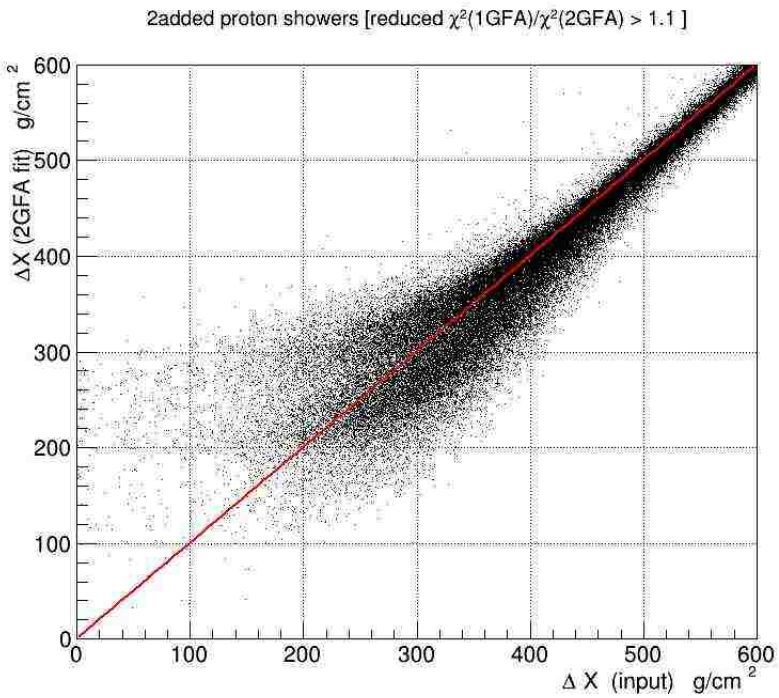

Figure 3.29: The separation that the two-GFA fit finds vs. the actual separation of the 2 added showers. These are the fit results with reduced χ^2 ratio is $\chi^2(1GFA)/\chi^2(2GFA) > 1.1$.

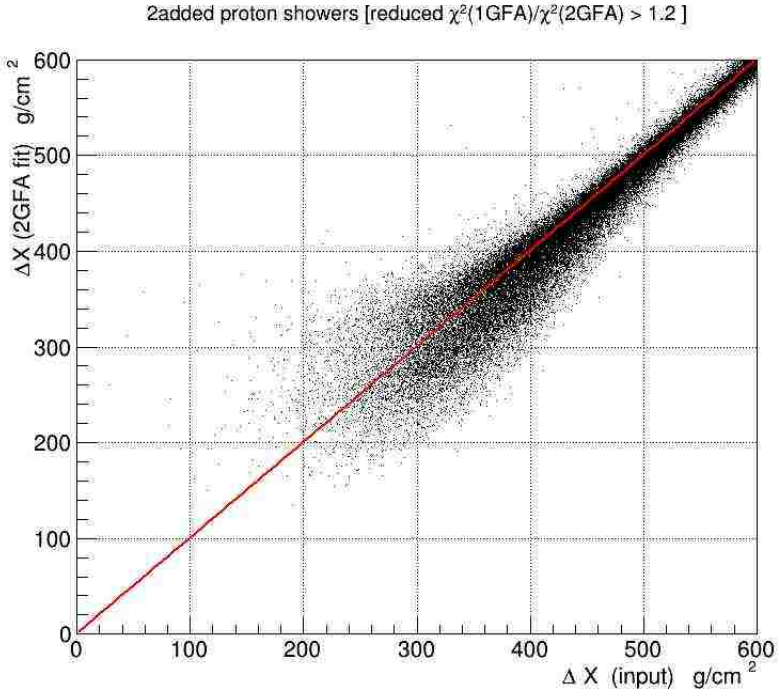

Figure 3.30: The separation that the two-GFA fit finds vs. the actual separation of the 2 added showers. These are the fit results with reduced χ^2 ratio is $\chi^2(1GFA)/\chi^2(2GFA) > 1.2$.

3.3.6 Two-GFA Fit on The Simulated Air Showers

The next step is to assess the number of "regular" air showers (i.e., single simulated showers) that are misidentified as irregular. We start by fitting single simulated air showers with the two-GFA function. Our goal is to select proper cuts to minimize the number of regular air showers that pass. This is a subtle task: some regular single air showers indeed may possess a leading particle that has traveled some distance - we do not wish to lose those. Furthermore, the cuts we select shouldn't be too harsh, otherwise no air shower will remain for the analysis.

We have simulated 30000 proton air showers with E=10^{18}eV using the CONEX code. These simulations include information about the secondary particle production and their properties. Shower profiles are fluctuated in a manner consistent with air showers observed with (E, R_p) = (1 EeV, 5 km). Figure 3.31 shows the distribution of χ^2 ratios between one-GFA and two-GFA fits of single showers. The events at the tail of the distribution would be candidate irregular showers.

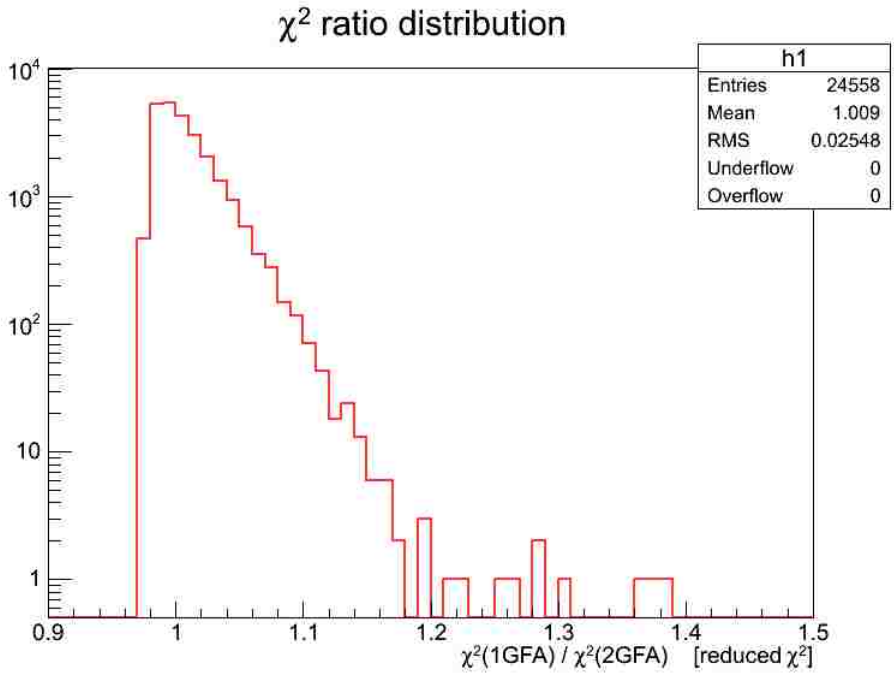

Figure 3.31: Ratio of χ^2 values for one-GFA and two-GFA fits of single, regular air showers.

We have checked the shape of the events with χ^2 ratio larger than 1.1, and there are some regular air showers among them. But for the events with χ^2 ratio larger than 1.2, almost all of them are irregular air showers. In this case there are 10 showers that passed the χ^2 ratio > 1.2 cut. The shower profile of these simulated events with the information about their LP is shown in the figures 3.32 to 3.42.

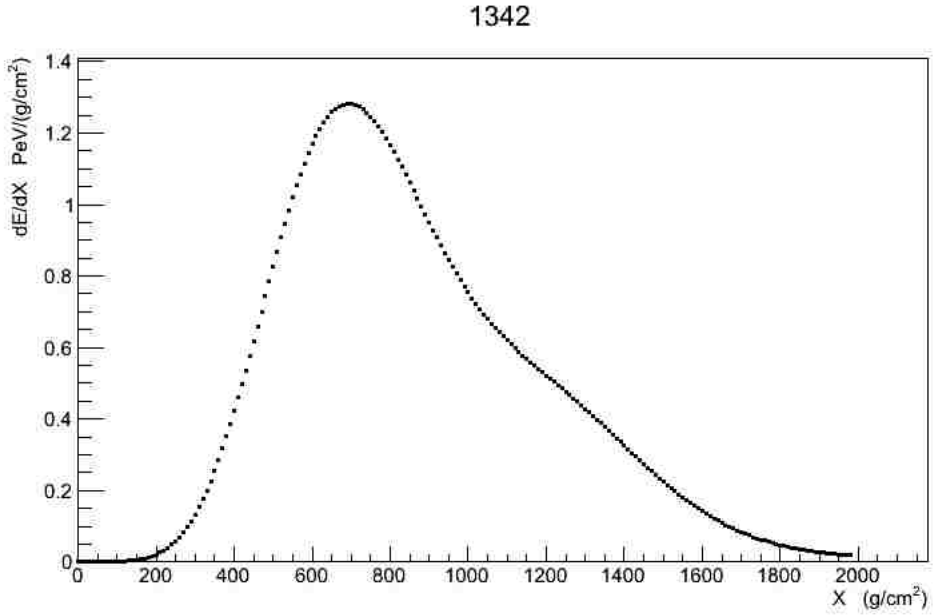

Figure 3.32: **LP**: Type: π^- E_{LP}= 0.21E$_0$ ΔX_{LP} = 410 g/cm^2
2GFA fit: $N_{max}1/N_{max}2$=3.3 ΔX= 515 g/cm^2

The two bumps are not obvious in the shower profile number 2473 (figure 3.33), because the separation between the sub-showers is not very large. There are some signs, other than 2GFA fit result, that suggests the shower profile is not a regular air shower and probably consists of two sub-showers. For example the X$_{max}$(1GFA fit) is very deep (815 g/cm^2) for a 1EeV proton shower. Also the N$_{max}$(1GFA fit) is 1.3 PeV/(g/cm^2), very below the average 1.6 PeV/(g/cm^2) for this energy. These can happen if the shower is a superposition of two sub-showers with fair separation between them.

The shower profile 3948 (figure 3.34) is a regular shower in every aspect. All the one-GFA fit parameters are around their specified mean values for 1EeV simulated proton showers. What has happened probably is that the fluctuating procedure had a severe effect on the

shower profile shape.

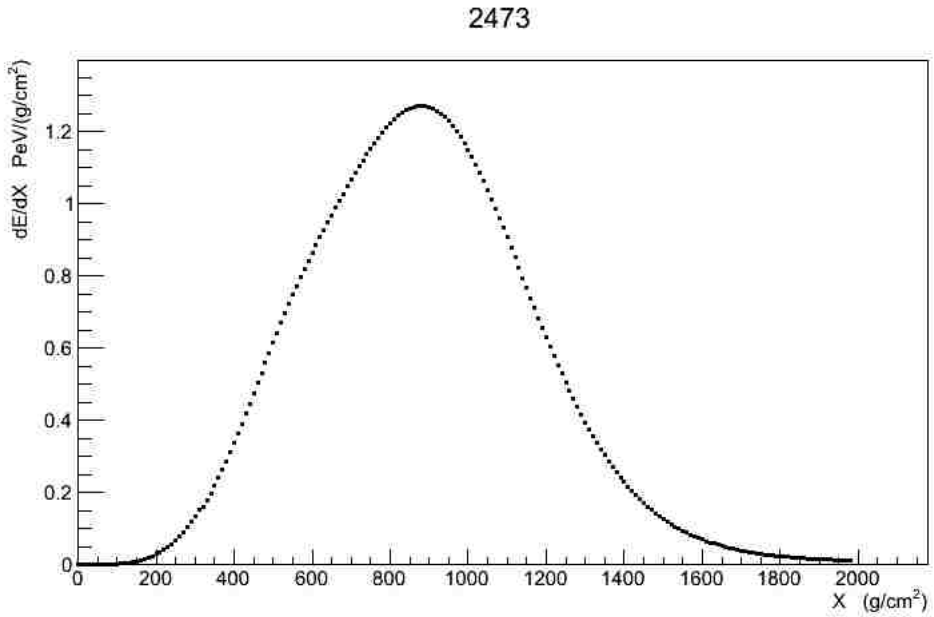

Figure 3.33: **LP**: Type: neutron E_{LP}= 0.52E$_0$ ΔX_{LP} = 287 g/cm^2
2GFA fit: $N_{max}1/N_{max}2$=1.2 ΔX= 284 g/cm^2

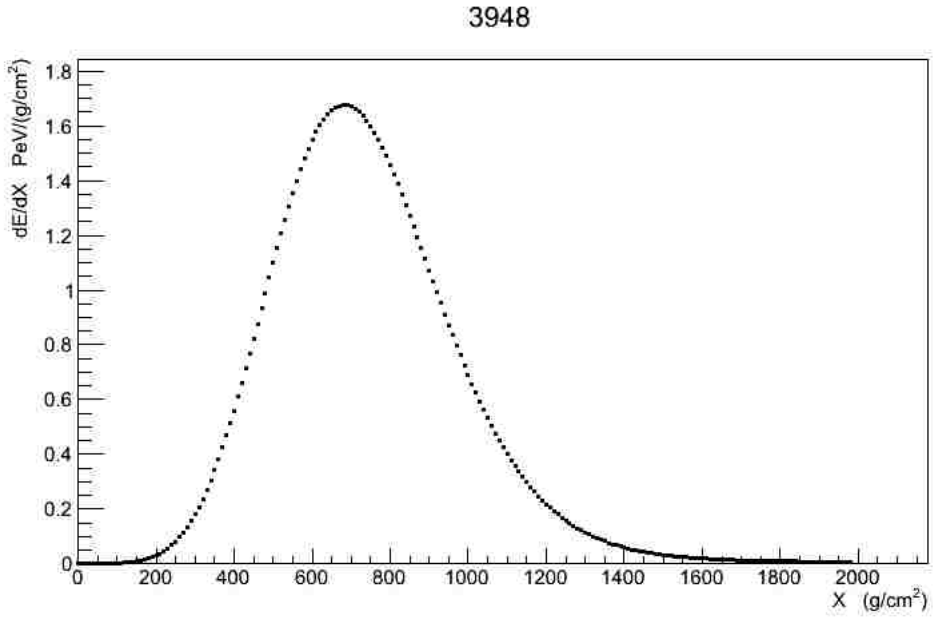

Figure 3.34: Not an irregular shower.
2GFA fit: $N_{max}1/N_{max}2$=3.5 ΔX= 259 g/cm^2

The shower profile 11296 fit result shows that when the separation between two sub-showers

is large, the fit can distinguish sub-showers even with 20% relative sizes.

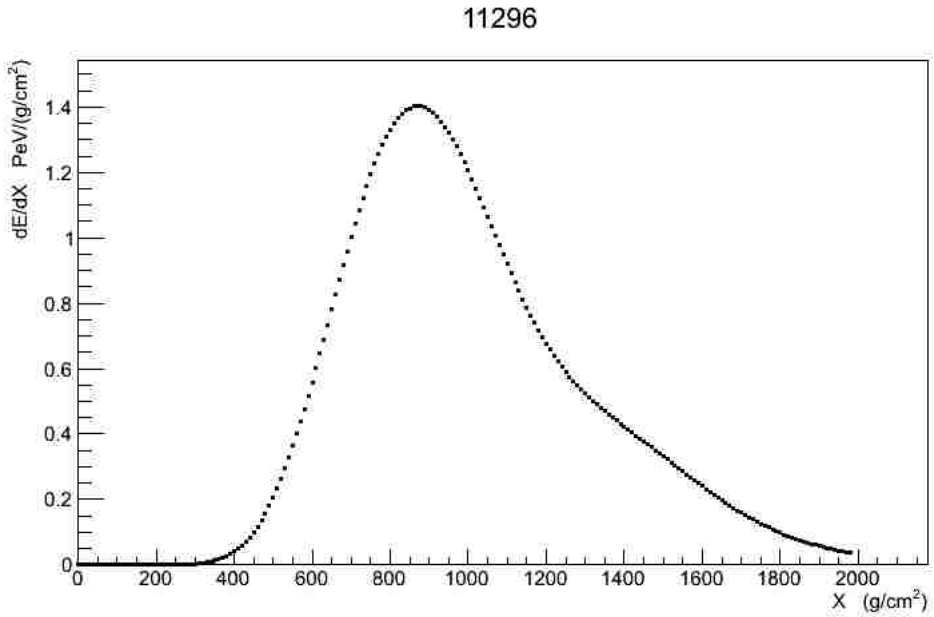

Figure 3.35: **LP**: Type: K^+ E_{LP}= 0.14E$_0$ ΔX_{LP} = 615 g/cm^2
2GFA fit: $N_{max}1/N_{max}2$=4.75 ΔX= 629 g/cm^2

In figure 3.36, the 2GFA fit finds a large separation (511 g/cm^2) between sub-showers in the shower 11536. But the leading particle path is just 220 g/cm^2. Additional information from the simulation indicate that one of the secondary particles coming out of the LP interaction with air has most of the energy (95% of its parent's energy). We name this particle "LP-of-LP". It has traveled 235 g/cm^2 before colliding an air molecule. So the two sub-showers should be almost 555 g/cm^2 apart.

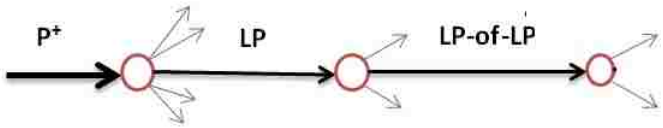

Figure 3.36: the LP interaction also can have a LP that has most of its parent(LP) energy, it is named "LP-of-LP".

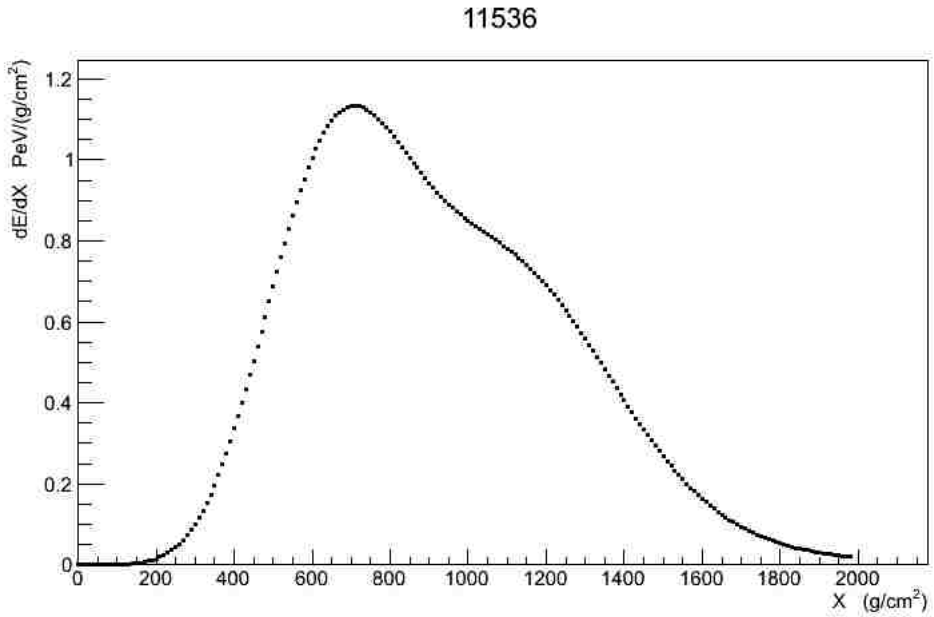

Figure 3.37: **LP**: Type: neutron E_{LP}= 0.32E$_0$ ΔX_{LP} = 220 g/cm^2
LP-of-LP: Type: neutron $E_{LP-of-LP}$= 0.3E$_0$ $\Delta X_{LP-of-LP}$ = 235 g/cm^2
2GFA fit: $N_{max}1/N_{max}2$=2.5 ΔX= 511 g/cm^2

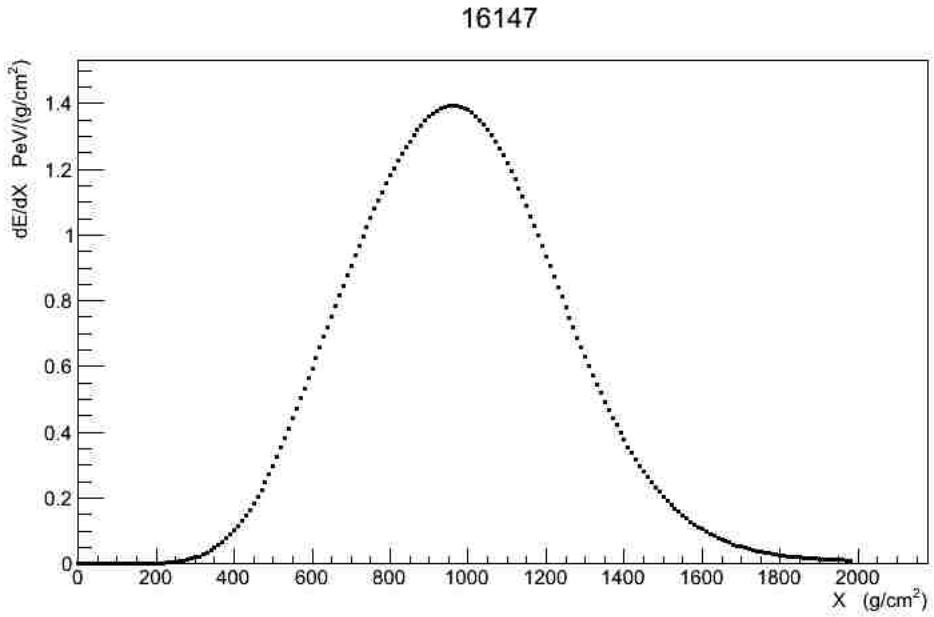

Figure 3.38: **LP**: Type: neutron E_{LP}= 0.7E$_0$ ΔX_{LP} = 1 g/cm^2
LP-of-LP: Type: neutron $E_{LP-of-LP}$= 0.58E$_0$ $\Delta X_{LP-of-LP}$ = 165 g/cm^2
2GFA fit: $N_{max}1/N_{max}2$=0.6 ΔX= 340 g/cm^2

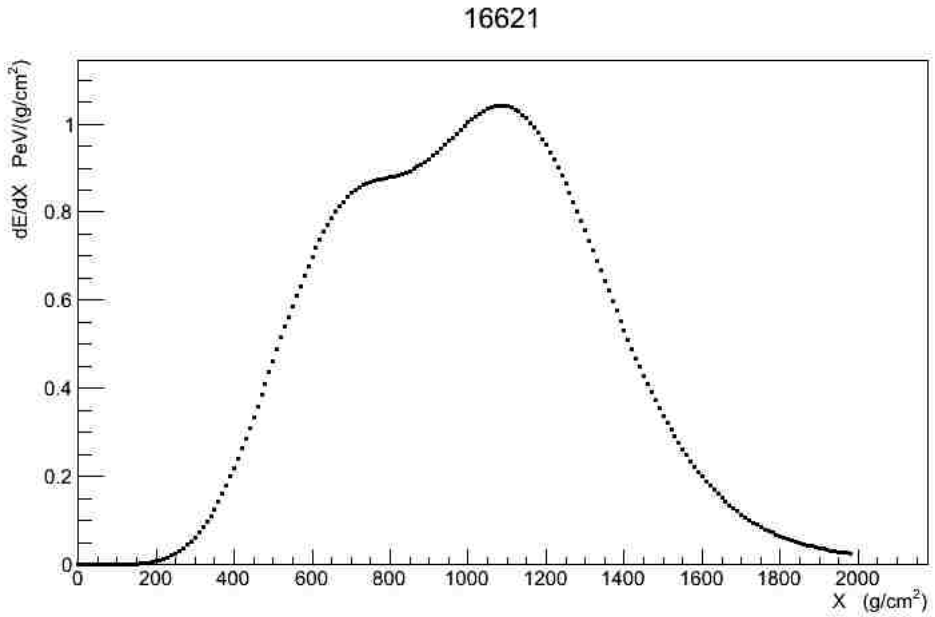

Figure 3.39: **LP**: Type: p^+ E_{LP}= 0.49E$_0$ ΔX_{LP} = 443 g/cm^2
2GFA fit: $N_{max}1/N_{max}2$=1.3 ΔX= 390 g/cm^2

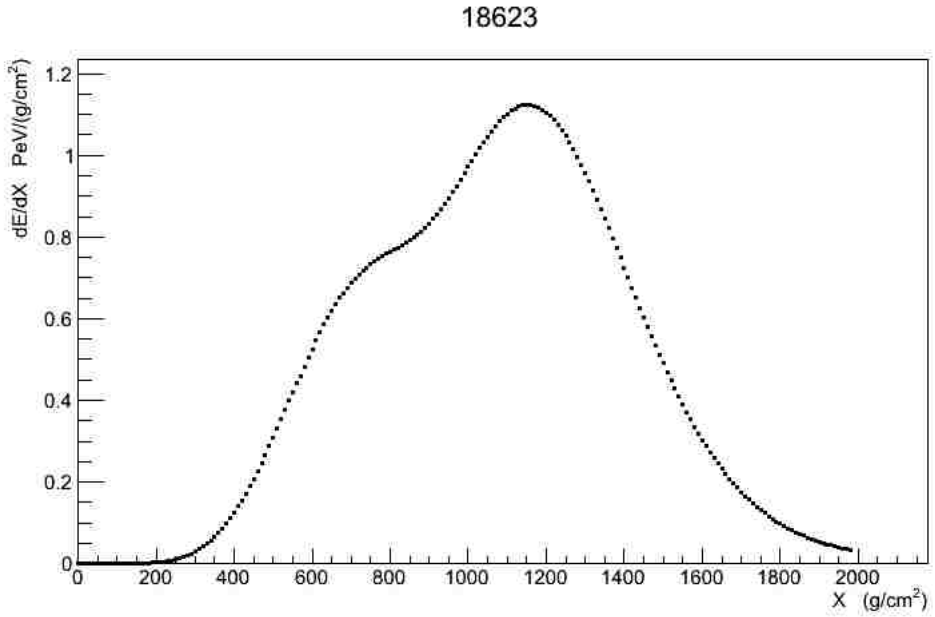

Figure 3.40: **LP**: Type: neutron E_{LP}= 0.6E$_0$ ΔX_{LP} = 506 g/cm^2
2GFA fit: $N_{max}1/N_{max}2$=0.78 ΔX= 457 g/cm^2

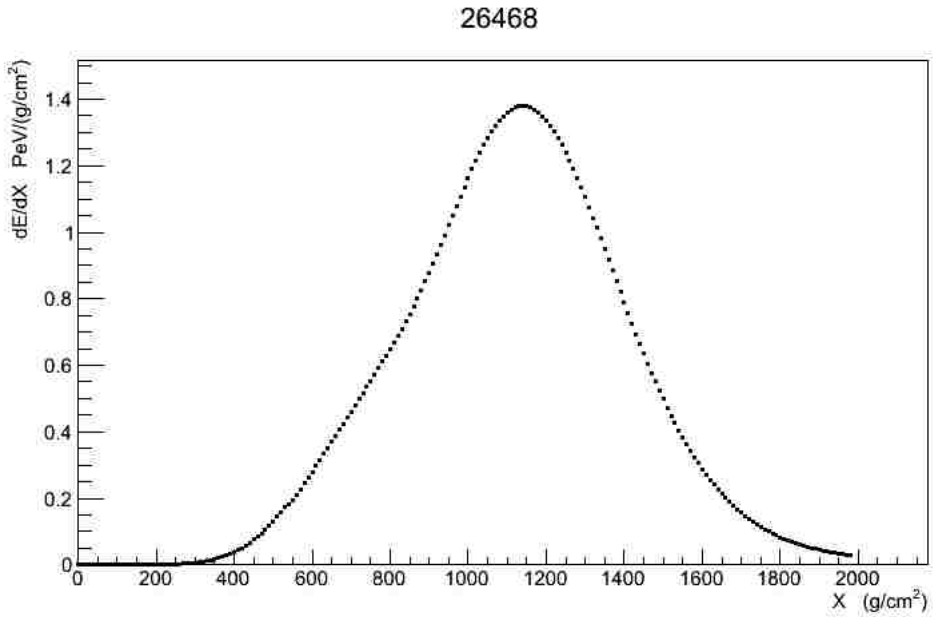

Figure 3.41: **LP**: Type: p^+ E_{LP}= 0.69E$_0$ ΔX_{LP} = 22 g/cm^2
LP-of-LP: Type: p^+ $E_{LP-of-LP}$= 0.68E$_0$ $\Delta X_{LP-of-LP}$ = 424 g/cm^2
2GFA fit: $N_{max}1/N_{max}2$=0.5 ΔX= 360 g/cm^2

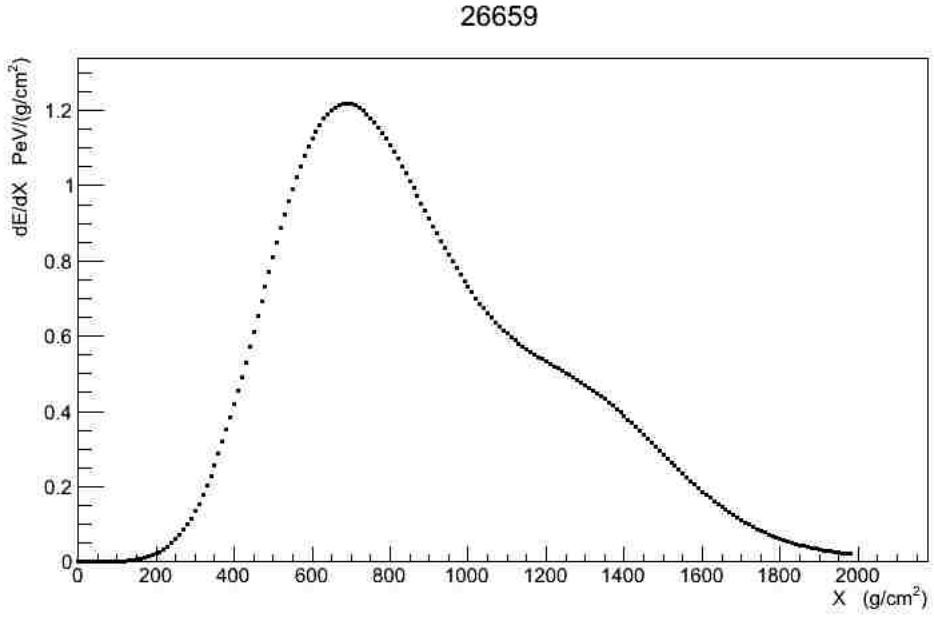

Figure 3.42: **LP**: Type: π^+ E_{LP}= 0.28E$_0$ ΔX_{LP} = 172 g/cm^2
LP-of-LP: Type: π^+ $E_{LP-of-LP}$= 0.26E$_0$ $\Delta X_{LP-of-LP}$ = 214 g/cm^2
2GFA fit: $N_{max}1/N_{max}2$=3.1 ΔX= 540 g/cm^2

3.3.7 Two Added Showers Separated With Exponential Distribution

We have made 90000 sample shower profiles by fluctuating and adding two simulated showers. The second shower is shifted such that the distance between X_{max} of the two added showers has an exponential distribution $\exp(-\Delta X/53)$ starting from 200 g/cm^2 (see figure 3.43). We make a very simplistic assumption that all shower profiles are superposition of two sub-showers with comparable sizes and a separation that has an exponential distribution.

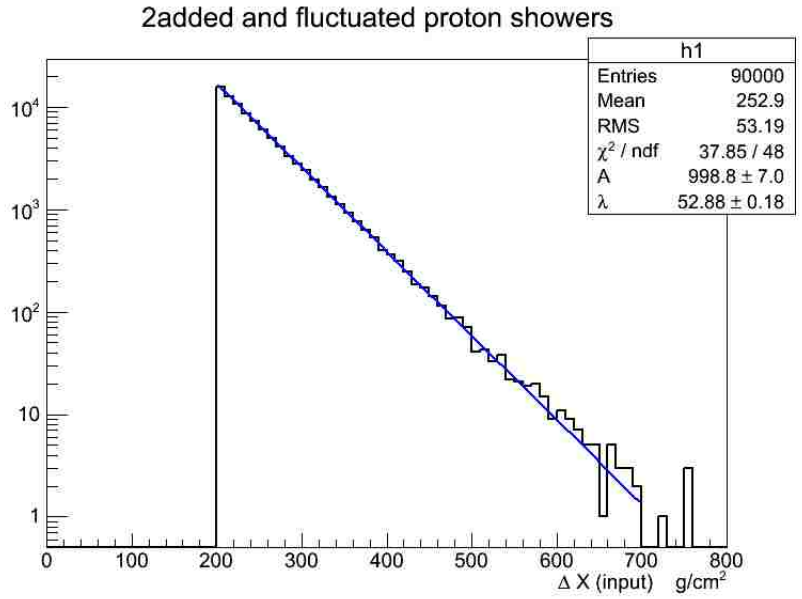

Figure 3.43: Histogram of the the input separation between X_{max} of the 2 added showers. It has exp(-X/53) distribution.

Figure 3.44 shows ΔX distribution from the 2GFA fit on the 2 added shower samples. The fit results are selected based on the following criteria:

- $\frac{\chi^2(1GFA)}{\chi^2(2GFA)} > 1.2$ [reduced χ^2].

The fit has kept the exponential features for $\Delta X(fit) > 350$ g/cm^2. There are two main reasons for the change in the exponential distribution for $\Delta X(fit)$ values less than 350 g/cm^2. First, the χ^2 ratio cut filters out many events with small separations. Second, the fit result has a random error in measuring the right separation $\Delta X(input)$.

Lets assume the $\Delta X(fit) - \Delta X(input)$ has a normal distribution with standard deviation of 40 g/cm^2. This normal distribution will convolute with the exponential distribution and

the result will be as is shown in figure 3.45. The convoluted distribution tail keeps the exponential feature.

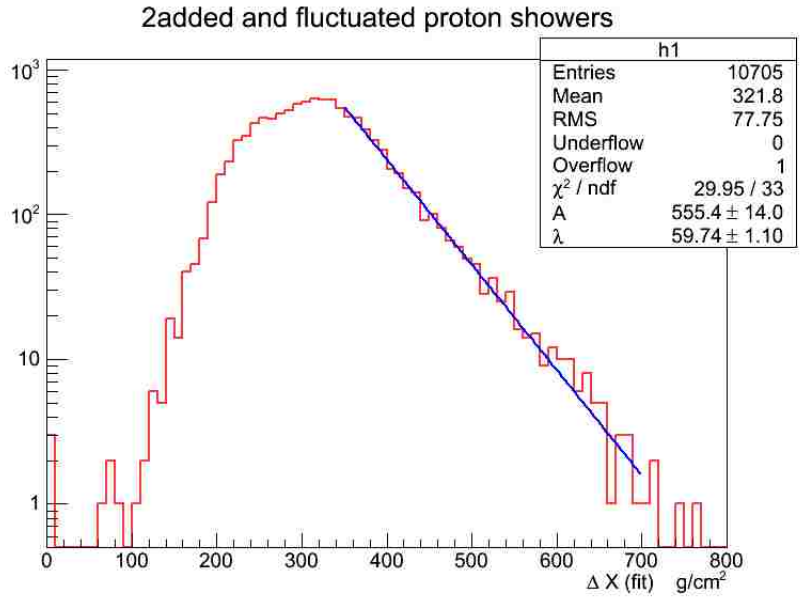

Figure 3.44: The separation that 2GFA fit finds for the 2 added showers. The distribution tail [350,700] keeps the exponential distribution with little change in slope ($\lambda = 59$).

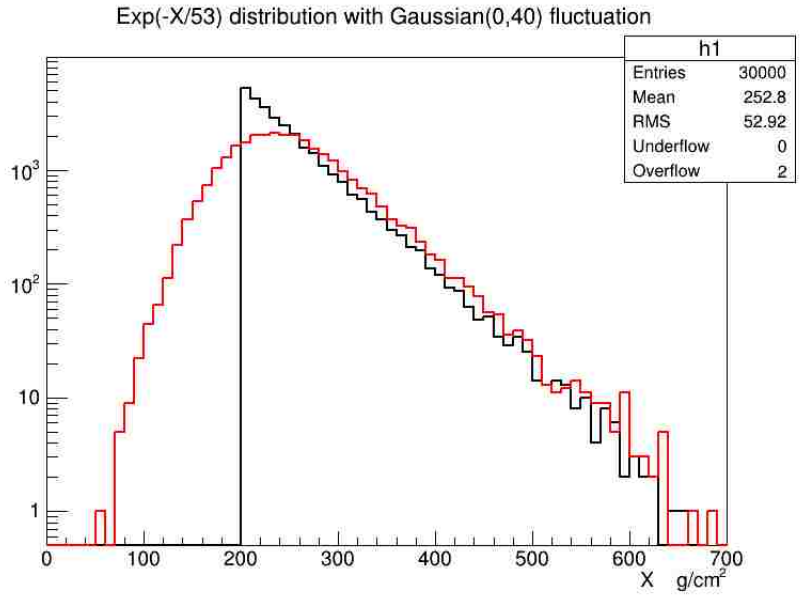

Figure 3.45: These are generated random numbers. The black histogram has exp(-X/53) distribution. Each data value is fluctuated with a normal function $N(0, 40)$ and the result is plotted in red.

3.3.8 Differences Due to Composition

What if the primary cosmic rays are nuclei and not protons? The method is applied on 10000 simulated iron showers and non of them passed the χ^2 ratio cut (see figure 3.46). So the method didn't pick any candidate for double-bump showers. The result is not unexpected, because an iron primary cosmic ray at high energy interactions behaves almost like 56 nucleons. So the total shower would be a superposition of these 56 subshowers.

It is very unlikely to have a double bump shower. It needs the subshowers to bunch up in two groups each with almost 26 members. Showers in each group shower have almost the same X_{max}, and the two groups should have well separated X_{max}. As I have mentioned, it is very unlikely for all these conditions to be satisfied all together.

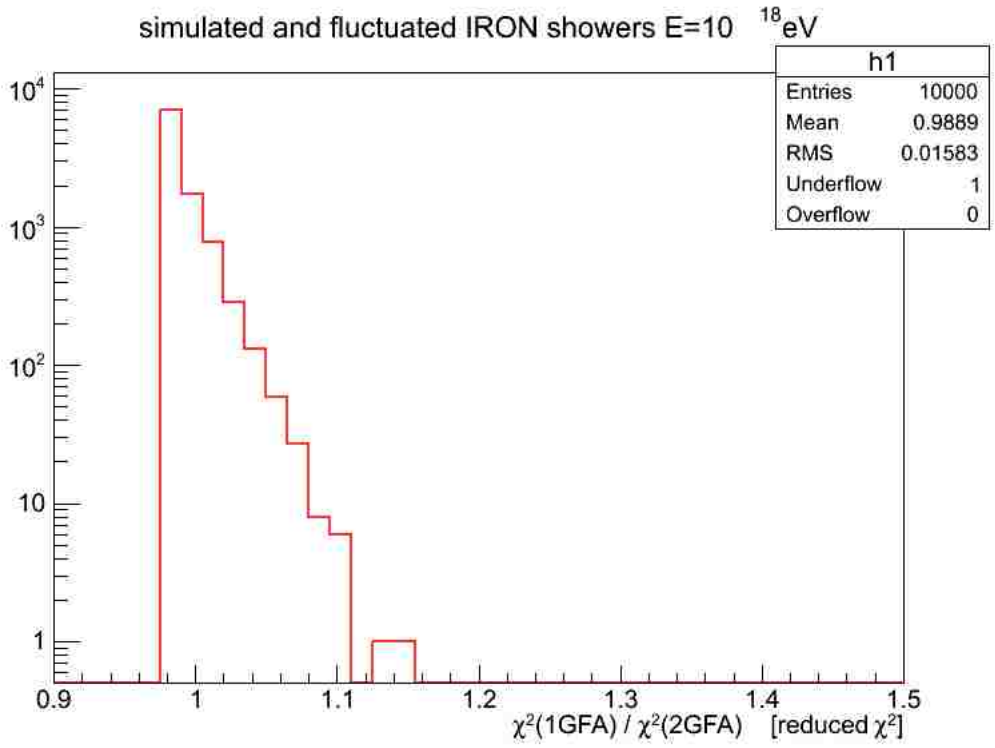

Figure 3.46: The χ^2 ratio distribution for 10000 simulated and fluctuated IRON showers.

4. Contaminated Data

4.1 Cloud Identification with Satellite

The interpretation of the detected cosmic ray air shower fluorescence light demands extensive and detailed information about atmosphere status. The existence of clouds in the field of view could affect the detected light. We discuss two shower and cloud geometries here.

If a cloud is located between the air shower and the fluorescence detector, then the cloud can shadow part of the fluorescence light coming toward the FD (figure 4.1a). This shadow usually looks like a valley in the reconstructed shower profile (figure 4.1b). The other scenario is that the air shower passes through a cloud. In this case the air shower Cherenkov light, which has a forward directed light cone, could be scattered toward the FD (figure 4.2a). Because this light is scatterred multiple times, it usually reaches the detector with more delay. This excess light makes a peak in the reconstructed shower profile (figure 4.2b). Multiple instruments like the central laser facility (CLF), extended laser facility (XLF), LIDARs and IR cameras are being used in the Auger observatory to detect the clouds over the array. But these instruments can't cover the whole array, and there are time gaps in their data [35].

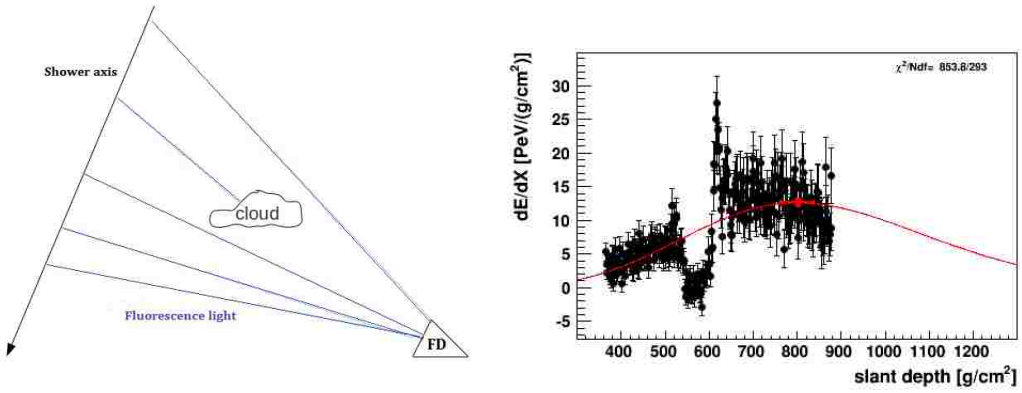

(a) (b)

Figure 4.1: (a) a cloud between the air shower and FD could shadow the Fluorescence light. (b) The cloud shadow shows itself like a valley in the reconstructed shower profile.

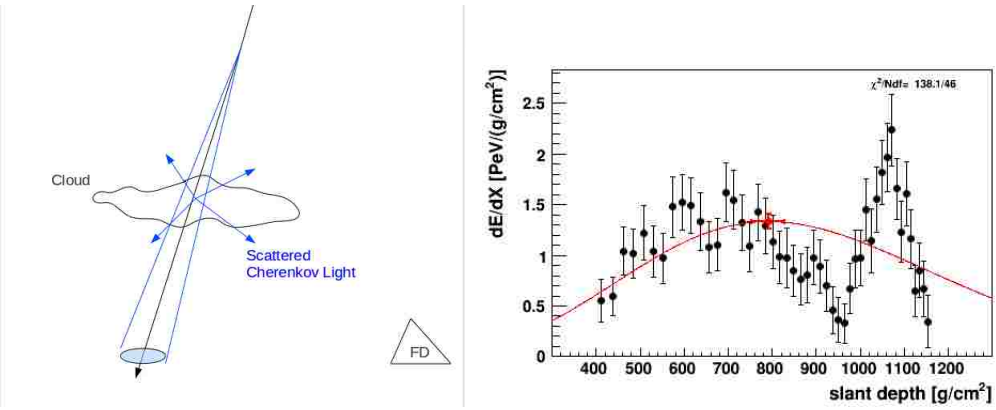

(a) (b)

Figure 4.2: (a) an air shower passes through a cloud and part of the Cherenkov light is scattered toward FD. (b) This excess scattered light makes a peak in the reconstructed shower profile

So a new method has been developed based on using meteorological satellite data to identify the cloud coverage over the Observatory site (see [36]).

4.1.1 GOES Satellites

Geostationary Operational Environmental Satellites (GOES) are a group of meteorological satellites that cover the whole planet [39]. The south American continent, where the Auger Observatory is built, is in the GOES-12 field of view (it is now replaced with GOES-13 [37]). It takes an image every 30 minutes. Each image is taken in 5 wavelength bands, four bands in infrared (figure 4.4) and one band in visible wavelength. The projection of these pixels on the Auger site has 2.4km×5.5km size (see figure 4.3).

The mean wavelengths of the four infrared bands are 3.9, 6.5, 10.7 and 13.3 μm. They are labeled in figure 4.4 with band identification numbers 2,3,4 and 6 respectively. GOES measures the radiation intensity $I(\lambda)$ for each band. The brightness temperature is calculated as follows

$$T_\lambda = \frac{hc}{k\lambda}\left(ln(\frac{2hc^2}{\lambda^5 I(\lambda)}+1)\right)^{-1},$$

where k and h are Boltzman and Planck constant respectively. These four brightness tem-

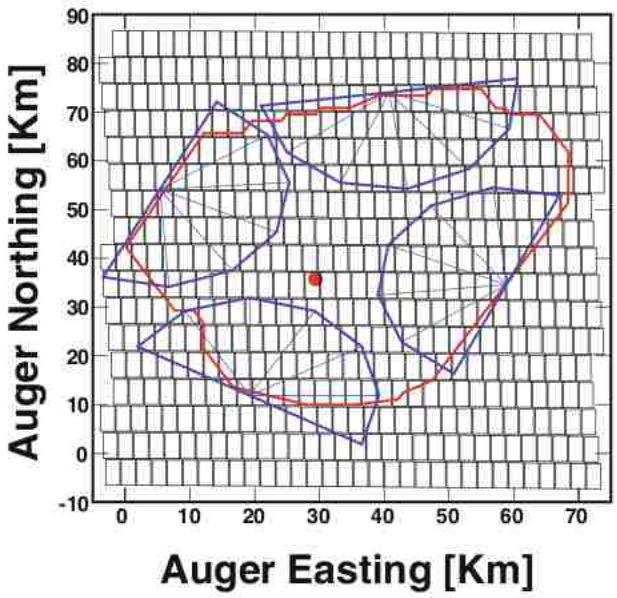

Figure 4.3: Satellite image pixels over the Auger site map. Red line indicates the SD border. Red point, in the middle of the site, is the CLF location. Blue lines show FD field of view. Picture taken from [38]

peratures, which are calculated for each pixel, can be used to identify clouds. The brightness temperature depends on the emissivity ϵ and temperature of the radiating surface . The object's surface temperature and its brightness temperature would be the same if $\epsilon = 1$. The $T_2 - T_4$ quantity would be almost zero if measured for earth surface, but it has a nonzero value for clouds. Because unlike the earth's surface, the emissivity of clouds depends on the wavelength. So the cloud transparency is different for each wavelength, and we are looking into different depths of cloud at different wavelengths. Band 3 is highly attenuated with atmospheric absorption (see figure 4.4), so it has low sensitivity to the earth surface temperature. But clouds could moderate the atmospheric absorption, So the T_3 value is sensitive to the cloud content of the pixel [38]. Both T_3 and $T_2 - T_4$ could be compared with ground temperature (measured on the ground) to distinguish the cloudy pixels. But we just have ground temperature information for 5 points over the Auger site. So we need a cloud finding method that relies only on the satellite data.

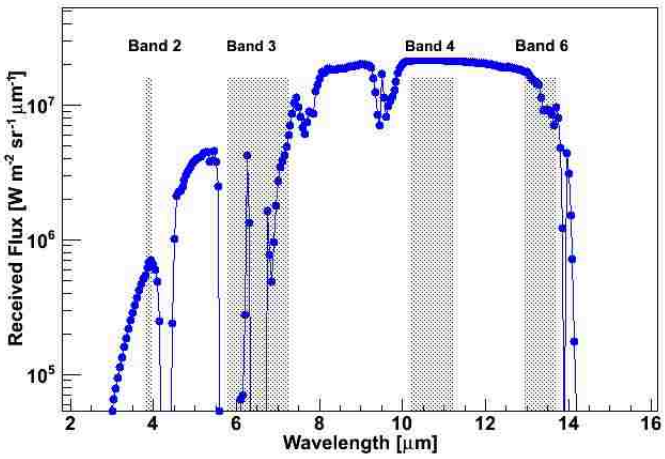

Figure 4.4: The four gray areas indicate the Infrared wavelength band coverage for GOES. It is superimposed on a thermal spectrum with T=280K. The atmospheric absorbtion is applied to the spectrum. Picture taken from [35]

The CLF has been used to cross-check if any method could find the cloudy pixels. CLF shoots a vertical laser beam every 15 minutes during the FD active time. The scattered light is detected by the FD and it is used to calibrate the detection. If a cloud happens to be above the CLF, it will scatter the light severely. Figure 4.5 shows the detected light for a clear and a cloudy event. The peak (red points) indicates scattered light from a cloud moving above the CLF. So we have the cloud data for the specific atmospheric pixel where the CLF is located.

Figure 4.6 shows a large sample of brightness temperature data from the CLF pixel measured by the satellite. If the CLF data indicate any cloud before and after the satellite image, the pixel is assumed to be cloudy. The same procedure is done to find out when the CLF pixel is clear. The separation between cloudy and clear events (red and blue points) in T_3 versus $T_2 - T_4$ scatter plot (figure 4.6) shows the cloud finding algorithm works properly. The blue and red points are most separated when projected onto the fitted line. There is a small mixture between cloudy and clear data points. This mixture indicates a disagreement between the satellite cloud finding and the CLF cloud data. The main reason that could explain this mixture is the CLF laser beam only illuminates an area of 100m across which is

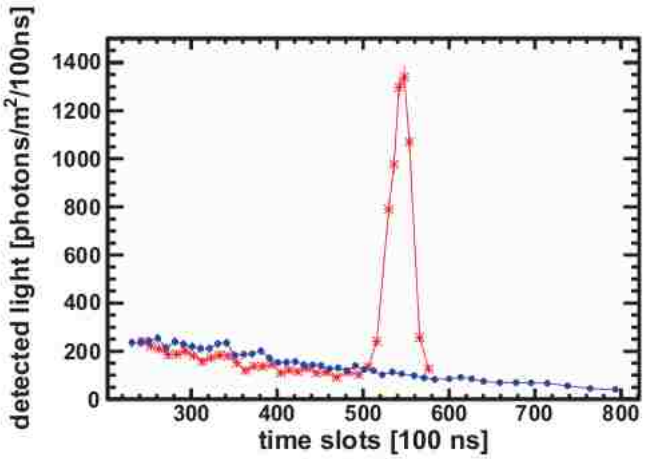

Figure 4.5: Two light profiles from CLF vertical laser shot detected with FD. Blue profile is measured during a clear night. The red profile shows a peak which indicates reflected light from a cloud. Picture taken from [36]

a tiny portion of the pixel [35]. A small cloud could show itself in the CLF data and the pixel would be assumed as cloudy. But the CLF pixel in the satellite image has nearly 13 km^2 area and the brightness temperatures are determined based on the total radiation intensity from the pixel area. Notice that all T_2,T_3 and T_4 are measured with the GOES satellite and if we quantify this separation between clear and cloudy events, this method could be extended to other pixels too.

Figure 4.7 is a histogram for the projected position of the blue and red points on the fitted line (X_P). The rotation transform of coordinates in figure 4.6 gives the value for X_P

$$X_p = (T_2 - T_4)\cos\theta - (T_3 - I_0)\sin\theta = \sqrt{\frac{1}{1+m^2}}(T_2 - T_4) - \sqrt{\frac{m^2}{1+m^2}}(T_3 - I_0),$$

where θ is the fitted line angle to the horizontal axis, and $\underline{m}$ is the fitted line slope. I_0 is the T_3 intercept and m is the slope of the fitted line. The black and red histograms represent the clear and cloudy data respectively. There are more clear than cloudy events in this sample. The clear data population should be weighted down until the area under the clear and cloudy histograms become equal. The blue line in figure 4.7 is the weighted curve for the clear events.

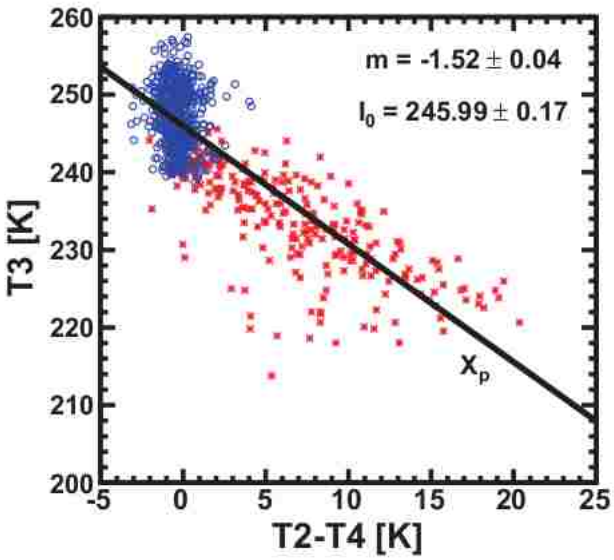

Figure 4.6: Brightness Temperature T_3 vs. $T_2 - T_4$ for the CLF pixel. Open blue circles show the clear event, and red stars show the cloudy events determined with the CLF data. I_0 is the T_3 intercept and m is the slope of the fitted line. Picture taken from [36]

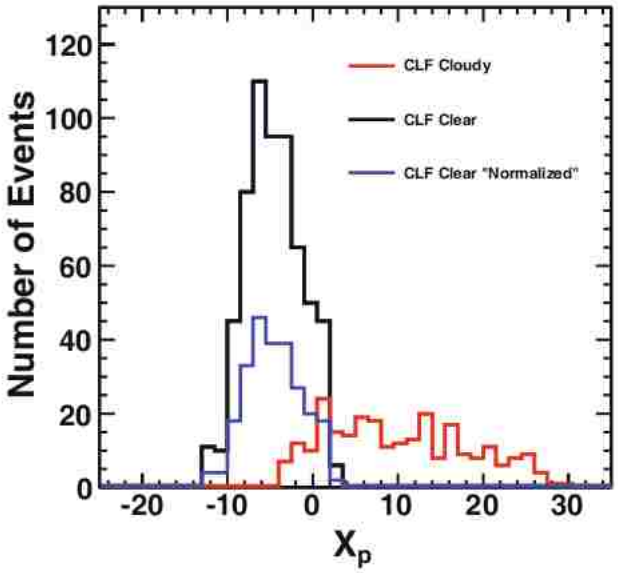

Figure 4.7: Histogram of the X_P values for the cloudy and clear events. The blue histogram is the normalized clear data which has the same area as the cloudy data histogram. Picture taken from [38]

Now based on the X_P value for a given pixel, a probability of cloudiness could be calculated for it. In equation 4.1, number of cloudy and clear events are determined from the red

and blue histograms (figure 4.7) at the specific X_P.

$$\text{Cloud Probability} = \frac{\text{Number of cloudy events}}{\text{Number of cloudy events} + \text{Number of clear events}} \tag{4.1}$$

Every pixel in the satellite image is given a cloud probability and the cloud probability map is made (figure 4.8). These cloud maps are made for most of the air showers detected by the FD with the shortest time difference possible from the actual shower recorded time. They can help us to determine the contamination of detected air shower fluorecence light as it has been explained in figures and .

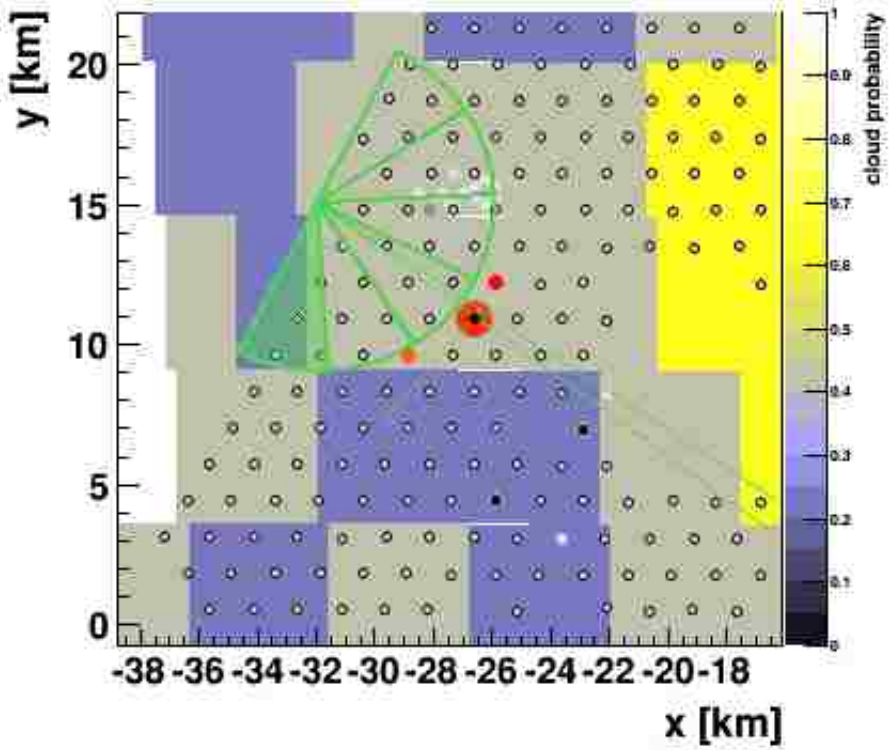

Figure 4.8: This is how a cloud probability map looks like. probability of cloudiness is shown with the color scales. The FD location is shown with green color. The triggered surface detectors are shown in red.

4.2 Cherenkov Light

When a charged particle passes through a medium with a speed higher than speed of light in that medium, medium radiates Cherenkov light. The speed of light in the medium is c/n, Where n is the refraction index of the medium.

At relativistic speeds, The electric field of the charged particle is contracted along the movement direction. So the electric field strength is boosted in a direction transverse to the moving direction (figure 4.9). This narrow and strong Electric field kicks the bounded electrons, and makes them oscillate. These bounded oscillating electrons radiate electromagnetic waves. These waves are add incoherently except when the particle has a speed βc higher than c/n. Then they will add up constructively on a cone surface behind the particle. This phenomena is similar to the shock made by a supersonic bullet.

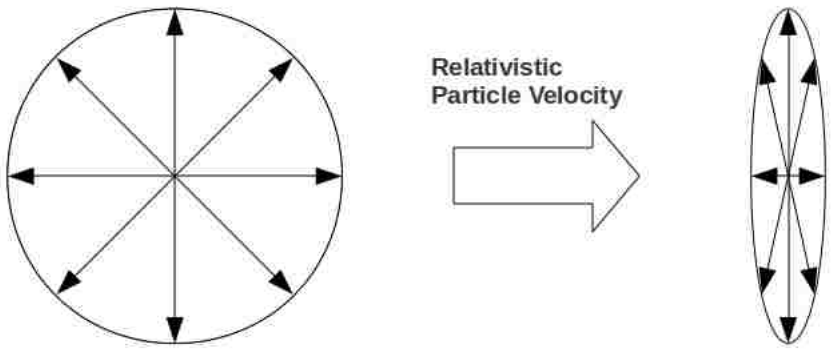

Figure 4.9: The electric field lines for a charged particle, non-relativistic (left) and relativistic (right)

For instance, an electron moving with speed βc from point A_1 to A_2 as shown in figure 4.10. As the electron reaches to A_2, the radiation wave travels from A_1 to B_1. The radiation will reach to the edge of all three circles simultaneously. So radiation on the D line (which is a cone surface in 3-dimensions) is coherent. The Characteristic angle of Cherenkov radiation (θ_c) which is dependent to particle energy and the medium is derived in equation 4.2.

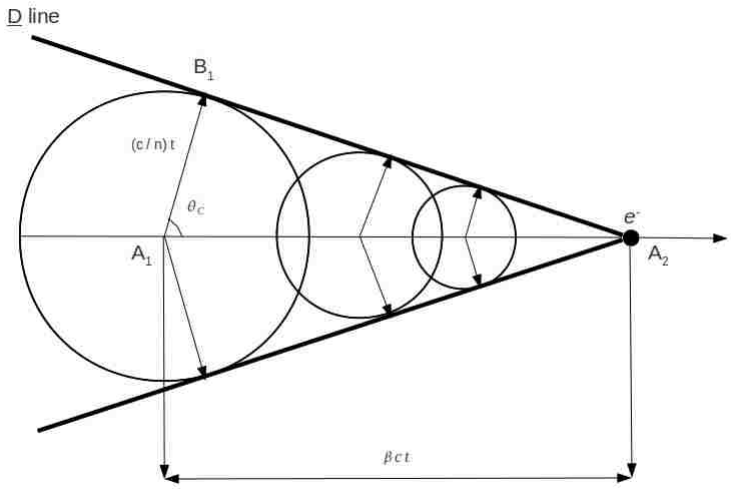

Figure 4.10: Huygens construction explains Cherenkov radiation as a phenomena very similar to the shockwave produced by supersonic jets. The characteristic angle for the Cherenkov radiation in the medium is θ_c. All the waves on the D line have same phase.

$$\overline{A_1B_1} = \frac{c}{n}t = \frac{c}{n}\left(\frac{\overline{A_1A_2}}{\beta c}\right) = \frac{\overline{A_1A_2}}{\beta n}$$
$$\cos(\theta_c) = \frac{\overline{A_1B_1}}{\overline{A_1A_2}} = \frac{1}{\beta n} \tag{4.2}$$

Air shower electrons can radiate Cherenkov light if they are above the minimum energy E^e_{min}.

$$v_e > \frac{c}{n} \implies E^e_{min} = \frac{m_e c^2}{\sqrt{1-\left(\frac{1}{n}\right)^2}} \tag{4.3}$$

The refractive index of air is a function of air density, so an atmospheric density model is required to determine where the electrons begin to radiate Cherenkov light.

4.2.1 Atmospheric Density Model

The atmosphere density decreases exponentially with elevation from the ground. The density at sea level is $\rho(0)$=0.001225 g/cm^3 (international standard atmosphere). It drops

to 36% of its maximum near altitude of H_0=8.4km above the sea level [42].

$$\rho(z) = \rho(0) \exp\left(-\frac{z}{H_0}\right) \tag{4.4}$$

The refractive index of air is related to the air density directly. It also varies with the radiation wavelength and the medium temperature. Equation 4.5 gives a linear approximation for the refractive index, where the n(0)=1.000291 at one atmosphere pressure, 15°C temperature, and $\lambda = 300nm$ [43]. Figure 4.11 shows the air refractive index versus altitude using the equations 4.4 and 4.5.

$$\frac{n(z) - 1}{n(0) - 1} = \frac{\rho(z)}{\rho(0)} \tag{4.5}$$

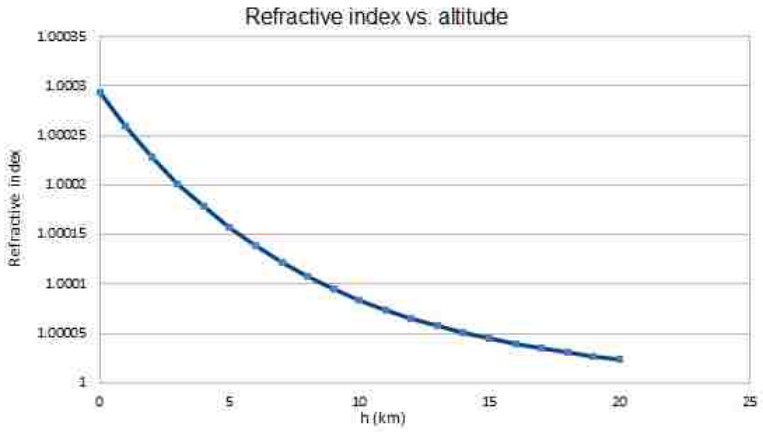

Figure 4.11: This plot shows the refractive index vs. altitude, n(z)=1+0.000291 exp(-z/H_0).

In the air shower analysis, the number of secondary particles are measured as a function of depth (g/cm^2) in the atmosphere. It is the amount of any matter traversed from top of the atmosphere to the point of interest. For a particle that enters the atmosphere with zenith angle θ, the trajectory length is $l = z/\cos(\theta)$. The atmospheric slant depth for a trajectory

with altitude z and zenith angle θ is calculated in following equation.

$$X(l,\theta) = \int_l^\infty \rho(l)dl = \int_l^\infty \rho(0)\exp(-\frac{l\cos\theta}{H_0})dl$$
$$= \left(0.001225\frac{g}{cm^3}\right)(\frac{8.4km}{\cos(\theta)})\ \exp(-\frac{l\cos\theta}{H_0}) = \frac{1030}{\cos\theta}\exp(-\frac{z}{H_0}) \quad (4.6)$$

This approximation works for showers with zenith angle $< 60°$. For larger angles the earth curvature should be taken into account. The total vertical depth of the atmosphere is 1030 g/cm^2 [44] (figure 4.12), and it is 2060 g/cm^2 for inclined showers with $\theta = 60°$ from the zenith.

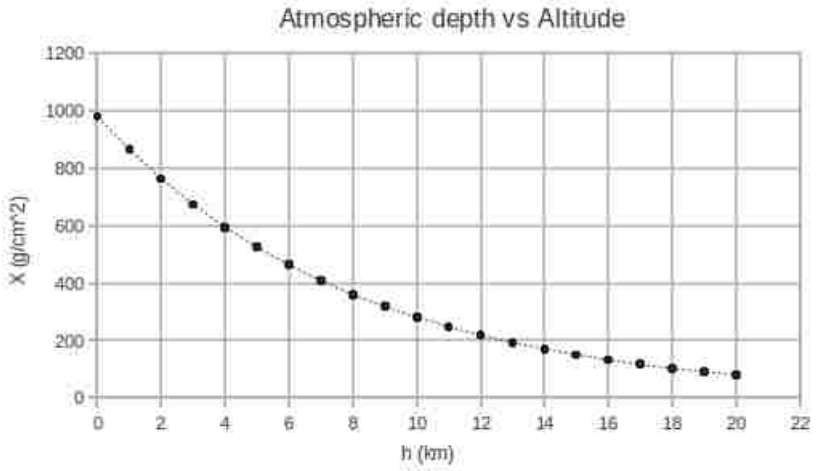

Figure 4.12: The atmospheric depth (g/cm^2) falls off exponentially as the elevation increases. For inclined showers, the $1/\cos(\theta)$ factor needs to be taken into account.

Based on the discussed atmospheric toy model, the minimum energy of electrons for Cherenkov radiation at different altitudes is given with equation 4.3. The threshold energy is shown in table 4.1 for several slant depths and two different zenith angles. The minimum required energy for muons is M_μ/M_e=206 times more than electrons. Energy distribution of electrons at shower maximum (s=1) is shown in figure 4.13. The spectrum is independent from the energy of the primary proton. A typical 10^{18}eV proton air shower has $X_{max} \approx$ 700g/cm^2, and the energy threshold for Cherenkov radiation is around 30 MeV (Table 4.1) .

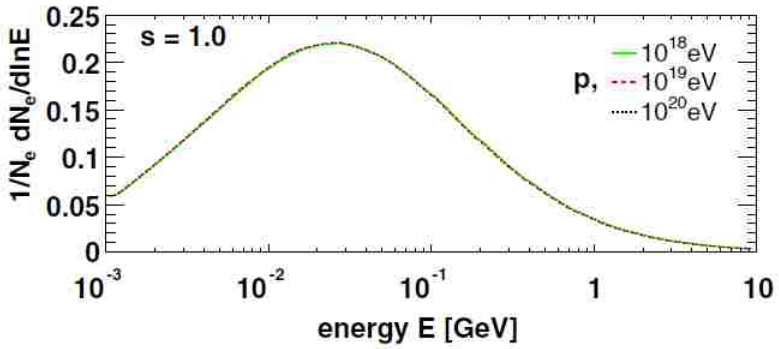

Figure 4.13: Electron energy spectra at shower maximum (s=1) for different proton primary energies. Picture is taken from [41]

Table 4.1: the minimum energy required for electrons to radiate Cherenkov light is shown for several slant depths and two different zenith angles.

	$E^e_{min}(\theta = 0°)$	$E^e_{min}(\theta = 60°)$
X = 300 g/cm^2	38 MeV	54 MeV
X = 700 g/cm^2	25 MeV	35 MeV
X = 980 g/cm^2	21 MeV	30 MeV

The Cherenkov angle θ_c for ultra-relativistic particles ($\beta \approx 1$) is arccos(1/n). Using this equation, one can estimate the θ_c at 700 g/cm^2, 1.17° and 0.82° for zenith anlges 0° and 60° respectively. So, This angle is roughly one degree everywhere. The air showers charged particles lateral distribution, electrons angular distribution (for details see [41]) and the scattering of Cherenkov light are the main reasons that in practice the air shower's Cherenkov light covers a larger region around the shower axis than what is expected from 1 degree divergence.

4.2.2 Number of Radiated Cherenkov Photons

The population of secondary particles produced in the air shower is dominated by electrons and positrons. These particles radiate a spectrum of Cherenkov light given by Frank-Tamm formula (Nobel 1958). This spectrum has $1/\lambda^2$ dependency, so it is attenuated fast for long wavelengths. In Equation 4.7, $\underline{\alpha}$ is the fine structure coefficient (1/137), and $\underline{z}$ is

the particle charge number.

$$\frac{d^2N}{dld\lambda} = 2\pi\alpha z^2 \frac{1}{\lambda^2}\left(1 - \frac{1}{\beta^2 n^2(\lambda)}\right) \tag{4.7}$$

In order to estimate the number of radiated photons, the equation 4.7 should be integrated over the lambda. The spectrum region we are interested in is $\lambda = 300 - 400nm$ [52]. The Fluorescence Detectors have optical filters that only transmit in this wavelength window. Also most of the radiation with $\lambda < 300nm$ will be absorbed in the atmosphere.

For ultra-relativistic particles $\beta \approx 1$ is a reasonable assumption. The refraction index $n(\lambda)$ variation with λ is approximately $dn/d\lambda = -0.14 \times 10^{-5} nm^{-1}$ [43] in this region of spectrum, which is very small and is negligible. So the refraction index could be estimated based on the altitude. The equation 4.8 shows the integral over the spectrum with $\underline{n}$ approximated for 700 g/cm^2 slant depth (z=6155m) and $\theta = 45^\circ$ zenith angle.

$$\begin{aligned}
\frac{dN}{dl} &= 2\pi\alpha z^2 \int_{300nm}^{400nm} \frac{1}{\lambda^2}\left(1 - \frac{1}{n^2}\right) \\
&= 2\pi \left(\frac{1}{137}\right)\left(1 - \frac{1}{1.00014^2}\right)\left(\frac{1}{300nm} - \frac{1}{400nm}\right) \\
&= 10.7 \ \ \frac{photons}{meter \times electron}
\end{aligned} \tag{4.8}$$

An air shower with 1EeV primary energy has almost 10^9 charged particles at its shower maximum which is around 700 g/cm^2 for proton showers. These particles will radiate 10^{10} photons per meter.

Figure 4.14 shows the number of produced Cherenkov photons per slant depth for a simulated 10^{19}eV proton shower with 30° zenith angle. In order to compare the number of photons between the simulation with our basic calculations, several details should be considered. First of all the primary energy is 10EeV, So the air shower will have about 10 times more particles at the shower maximum. Second is to consider the shower geometry

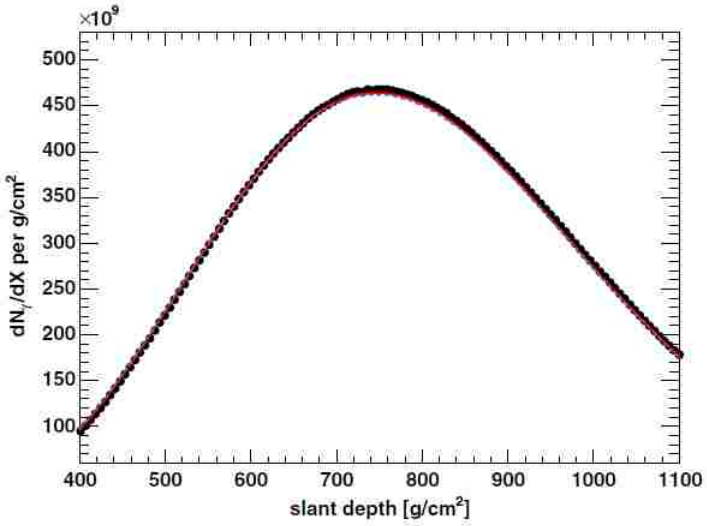

Figure 4.14: Total number of Cherenkov photons produced per slant depth (CORSIKA simulation, proton 10^{19}eV, $\theta = 30°$). picture taken from [41]

($\theta = 30°$), the shower maximum altitude at this energy (≈ 760 g/cm^2) and each slant depth is almost 10 meters at such altitudes. Finally, in this simulation (figure 4.14) indicates the number of Cherenkov photons over all wavelengths.

The Cherenkov radiation of an air shower covers a tight cone around the shower axis. If the cone is directed toward the FD telescopes, the collected amount of Cherenkov light could be comparable with the fluorescence light which propagates isotropically. The air shower Cherenkov light angular distribution is dependent on the angular distribution of the electrons. This angular distribution at shower maximum is well shown in a simulation at figure 4.15. The electrons are grouped in several energy ranges. The (a,b,c,d) energy ranges don't have enough energy to produce Cherenkov light. Also it is shown that the spectrum of more energetic electrons has less angular variation around the shower axis.

The propagation of the Cherenkov light in the atmosphere and its amount and direction is also dependent to the scattering and attenuation of the light. Rayleigh and Mie scattering are the major processes that affect the Cherenkov light propagation.

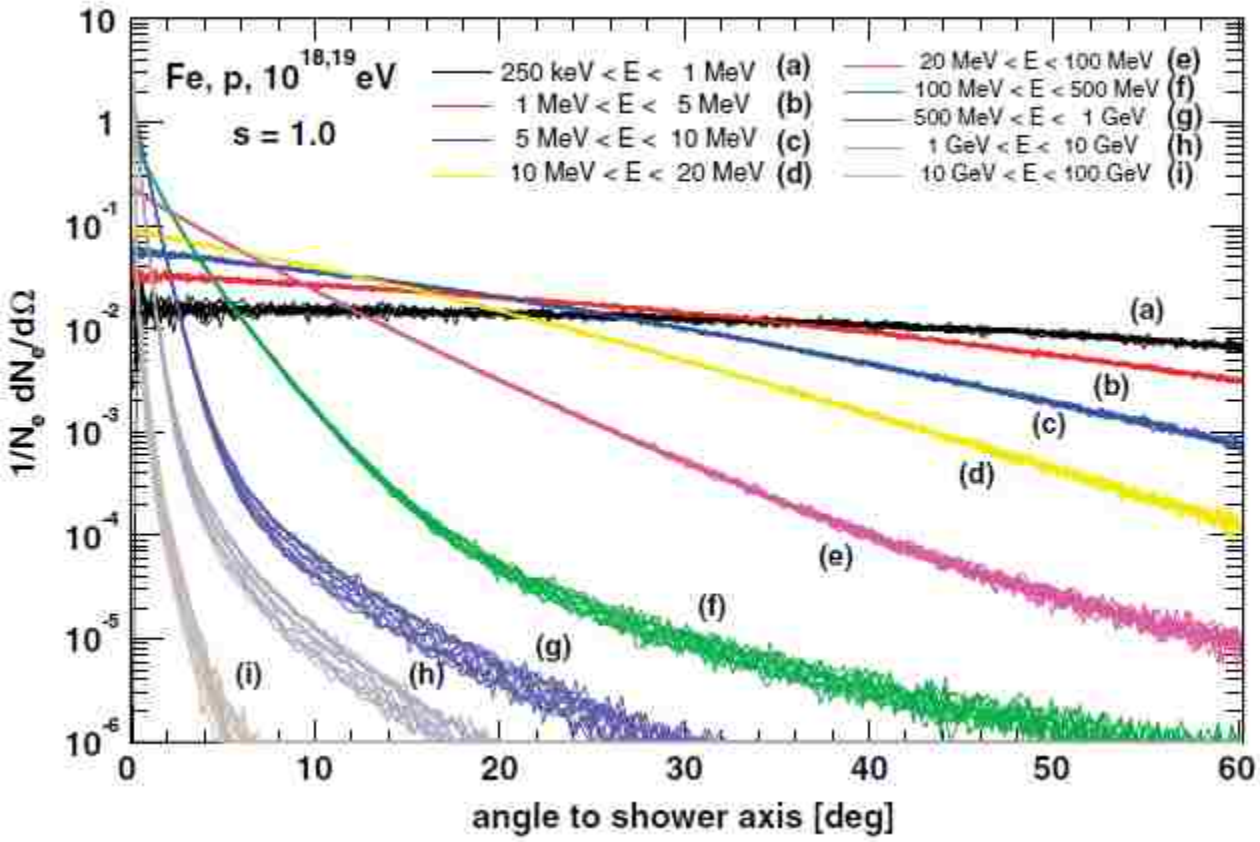

Figure 4.15: Electron angular distribution with respect to shower axis for showers with different energies and primary particles at shower maximum (CORSIKA simulation). Picture is taken from [41].

4.2.3 Rayleigh Scattering

Rayleigh scattering is an elastic scattering of photons from particles like atoms or molecules which have much smaller size than the photon wavelength. Because these particles are electrically polarizable, the oscillating electric field of the electromagnetic waves polarizes them. The electromagnetic wave being radiated from the oscillation of the charges in these particles have the same frequency with the incident wave.

The Rayleigh scattering cross-section is very sensitive to the wavelength and drops with $1/\lambda^4$ as the wavelength increases. The angular distribution of the Rayleigh cross-section has moderate dependence to the direction (equation 4.9). So the Rayleigh scattering is important for all angles. This effect causes some Cherenkov light to reach the fluorescence detectors,

even when the shower axis is not pointing toward the FD's.

$$\frac{d^2N}{d\theta d\lambda} \propto \frac{1}{\lambda^4}\left(1+\cos^2(\theta)\right) \tag{4.9}$$

The Rayleigh cross-section for an air molecule (%80 nitrogen and %20 oxygen) at λ=300 nm over all angles is σ_m=5.64×10^{-26} cm^2 [47]. Total amount of scattering for a volume of air is given with product of total molecular cross section, in the molecular number density of air N(z).

$$\sigma_T(\lambda, z) = N(z)\sigma_m(\lambda) \tag{4.10}$$

The molecular number density of the air at standard condition (P=1 atm, T=25 $^\circ C$) is N(0)=2.547 × 10^{19} cm^{-3}, that gives σ_T(300nm,0)=1.43 × 10^{-6} cm^{-1}.
Because number density N(z) and the density $\rho(z)$ are proportional, equation 4.4 could be used to find a rough estimation of N(z)/N(0).

$$\frac{N(z)}{N(0)} = \exp\left(-\frac{z}{H_0}\right) \tag{4.11}$$

In the case of the inclined air shower with 45° zenith angle, the probability of Rayleigh scattering for a Cherenkov photon with λ=300nm generated at 700 g/cm^2 is estimated in equation4.12. The assumption is that the photon is generated at 6150m altitude (700 g/cm^2) and will reach the FD at 1400m (1233 g/cm^2) with 45° angle. The 62% interaction probability means that 6 out of 10 photons will be scattered at least once in their path to the detector.

$$\begin{aligned}\int_{1400m}^{6150m} \sigma_T(300nm, z)\ \frac{dz}{\cos(45^\circ)} &= \frac{\sigma_m(300nm, 0)N(0)}{\cos(45^\circ)} \times (8.4km)\ exp(-\frac{z}{8.4km})\Big|_{1400m}^{6150m} \\ &= \frac{1.43 \times 10^{-6} cm^{-1}}{\cos(45^\circ)}(8400m)(0.3656) = 0.62\end{aligned} \tag{4.12}$$

These photons have passed through 1233 - 700 = 533 g/cm^2 of matter. The corresponding

mean free path is 533 $\times$ (1/0.62)= 860 g/cm^2. This value could be adopted for other wavelengths using the $1/\lambda^4$ scattering dependence. The mean free path for λ=400nm would be (400nm/300nm)^4 $\times$ 860 g/cm^2 = 2718 g/cm^2 The more accurate mean free path given by [Elterman & Toolin 1965] for wavelength $\lambda = 400nm$ is 2970 g/cm^2, which shows slight underestimation in our assumptions.

In the above example, It is assumed that the shower hit the ground at Auger FD location. So the estimated distance to the detector is the minimum amount of what actually exists. Also the estimated scattering probability in equation 4.12 shows that only a small fraction of air shower photon - whether fluorescence or Cherenkov - will arrive to the FD without scattering [48]. So the atmospheric scattering should be studied well.

4.2.4 Mie Scattering

Mie scattering is an elastic photon scattering which happens when the particle size is large respect to the photon wavelength. The atmospheric aerosol sizes has a wide distribution from few nanometers to micrometers in diameter [48]. The Mie scattering can not be described like the Rayleigh scattering with an analytic formula. Because in Mie scattering the size distribution and shape of the particles (aerosols) matters. The aerosols number density in the atmosphere is highly variable in time and location, and it depends on the wind and weather condition [48].

Mie cross-section dependency on photon wavelength is small and it depends on the kind of aerosols exists in the location. The measured Mie cross-section dependency on wavelength for auger site is almost zero. The scale height for aerosols number density is much smaller than H_0 [52], that makes the Mie scattering important for low altitudes.
The angular distribution of this scattering is highly peaked toward forward (see figure 4.16), and it drops exponentially for wider angles.

$$\left(\frac{d\sigma}{d\Omega}\right)_{Mie} \propto \exp\left(-\frac{\theta}{\theta_M}\right) \tag{4.13}$$

where $\theta_M = 22.6$ [52]. Equation 4.13 works for $\theta < 90°$. The angular dependence is not significant from $90° < \theta < 180°$ and it looks like the rayleigh scattering in this angular domain (more details are discussed at [48]).

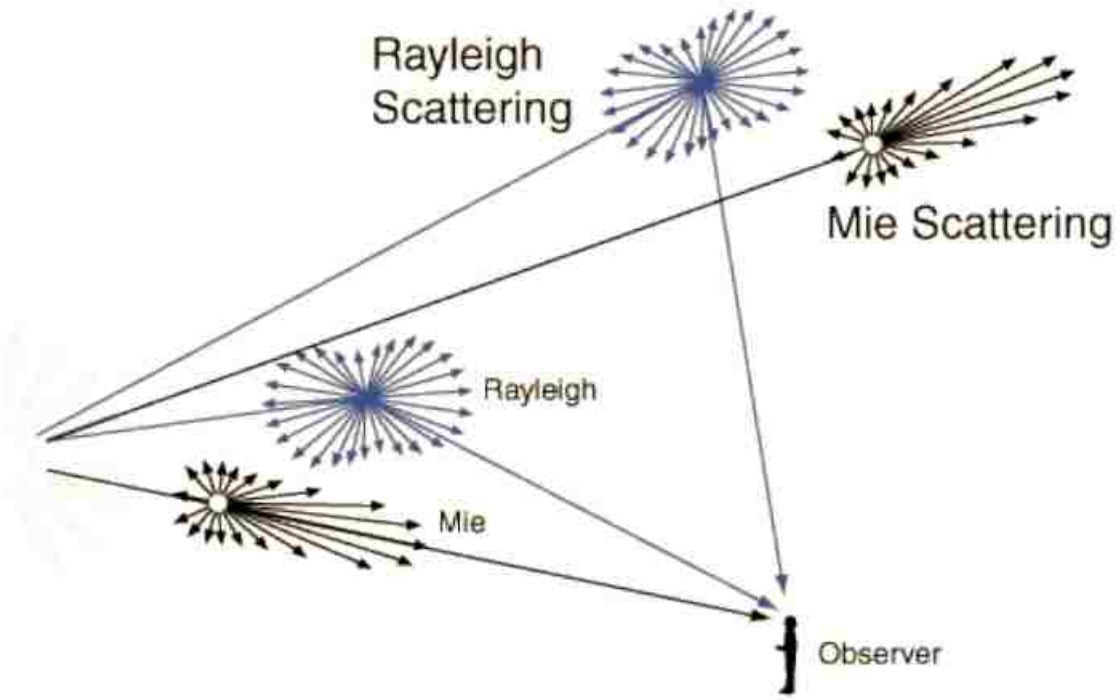

Figure 4.16: The Mie scattered light is more important for small scattering angles. For large scattering angles it is just the Rayleigh scattering that could play a role. Picture taken from [49].

4.2.5 Reconstructed Cherenkov Light at Auger Fluorescence Detector

The fluorescence detectors of the Pierre Auger Observatory are sensitive to the wavelength band 300-400nm. Air showers produce Cherenkov light with energy spectrum that include this detectable wavelengths. Fluorescence light is the main input for analysis of the main features of each air shower. So the Cherenkov light fraction is included in the reconstructed shower profiles. This fraction is determined with an iterative method based on the geometry of the shower and the attenuation of the Cherenkov light.

In the first step, the initial shower profile is reconstructed with the assumption that all the detected light from the shower is fluorescence light and no Cherenkov light contaminate it. Then number of charged particles ($e^{\pm}$) is calculated based on our knowledge about fluorescence yield factor [50]. The energy spectrum of $e^{\pm}$ in electromagnetic showers (see Hillas 1982 [51]) gives the fraction of the charged particles above the cherenkov emission threshold. So the number of radiated Cherenkov photons with wavelength 300-400nm could be calculated at each atmosphere level using the equation 4.8.

The attenuation due to Rayleigh and Mie scattering is taken into account to determine the direct Cherenkov light that arrives to the FD telescope. Most of Cherenkov light is not going toward the FD diaphragm directly, but a small fraction of it will be scattered toward the detector. The shower reconstruction also can determine the separate contribution of Mie and Rayleigh scattering in the detected scattered cherenkov light.

Finally, the calculated Cherenkov fraction will be subtracted from the total detected light and the same procedure is repeated untill the calculated Cherenkov fraction converges [52]. In figure 4.17, a reconstructed detected light of an air shower event is shown that has been detected with two fluorescence detectors (Los Leones & Coihueco) from different points of view. Figure 4.17.(a) shows the configuration of air shower axis with respect to the surface and fluorescence detectors. The surface detector (SD) colors specify respective arrival time of the shower front. The blue SD's are triggered earlier than the red ones. The fluorescence detectors, Los Leones and Coihueco, are shown with blue and red respectively. The shower axis is toward the Coihueco, and it is passing across the Los Leones field of view. So we expect more direct Cherenkov light be detected at Coihueco.

In figure 4.17.(b), the detected light reconstruction indicates the high fraction of direct Cherenkov light. But in Los Leones (figure 4.17.(c)) there is no detected direct Cherenkov light. The fraction of scattered Rayleigh Cherenkov light doesn't have significant difference at these two Detectors. Because the Rayleigh scattering angular dependence is small (as described in equation 4.9). We expect to see more fraction of scattered Mie Cherenkov light

in the Coihueco detection, because the Mie scattering is more toward the forward direction. But it is also important to know the aerosol distribution at the moment the event has happened, and without that information we can't predict the amount of Mie scattering.

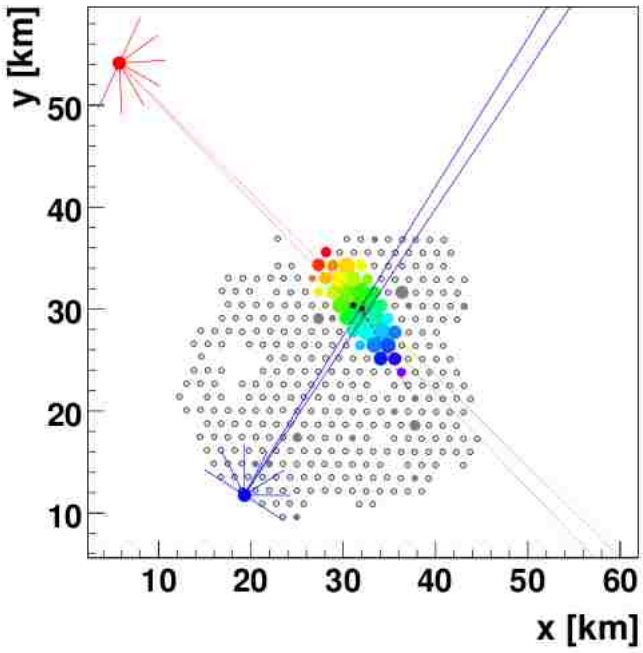

(a) Top view, Los Leones and Coihueco are shown with blue and red respectively

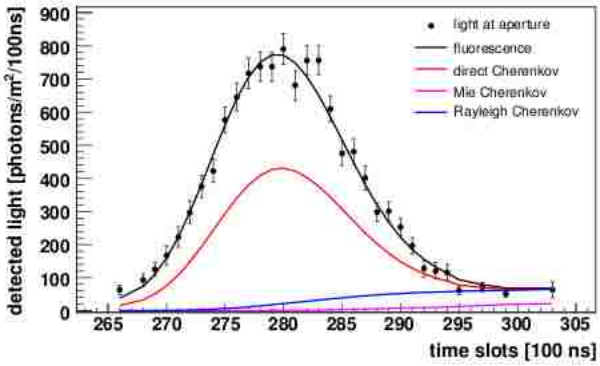

(b) Light flux at Coihueco

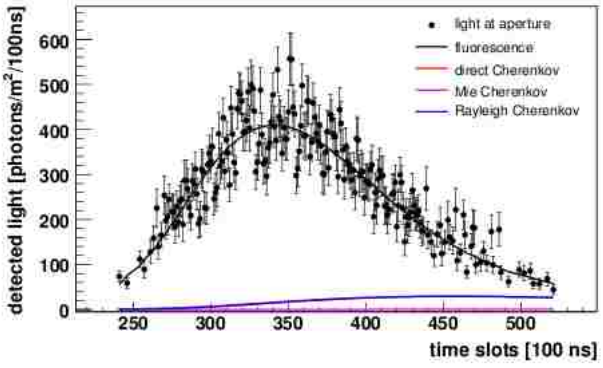

(c) Light flux at Los Leones

Figure 4.17: (a) The surface detector (SD) colors specify respective arrival time of the shower front. The fluorescence detectors, Los Leones and Coihueco, are shown with blue and red respectively. (pictures taken from [52])

The scattered Cherenkov light travels a longer path so it reaches the FD with a delay respect to the direct Cherenkov light [52]. Although Cherenkov light is highly focused toward

the particle direction, the total air shower's Cherenkov light can cover considerably wide angular range. Because the charged particles are deflected from primary particle direction due to multiple scattering [50]. Mean viewing angle (mva) is the angle between shower axis and the normal vector of the triggered pixel which has the mean trigger time with respect to the total observation time (figure 4.18).

The total fraction of detected Cherenkov light in an air shower is highly correlated with the mean viewing angle (figure 4.19). So in practice the mva quantity could be a good indicator of the fraction of Cherenkov light contamination in the air shower detected light.

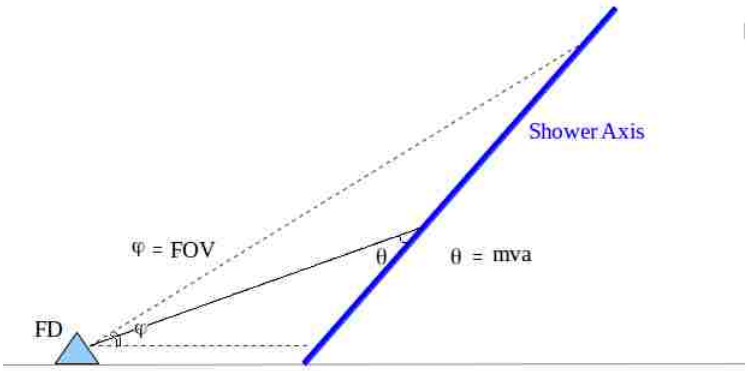

Figure 4.18: Mean viewing angle (mva) is the angle between shower axis and the normal vector of the triggered pixel which has the mean trigger time with respect to the total observation time.

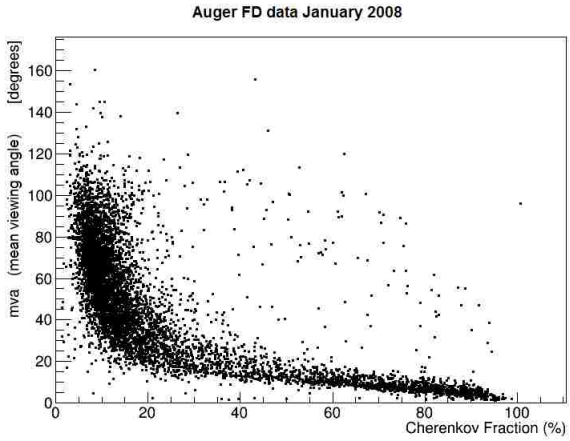

Figure 4.19: The Cherenkov fraction of the detected light for each air shower versus the mean viewing angle. Plot shows the total recorded data from January 2008 (Auger)

5. Auger Events

5.1 Events Selection

We have developed a method to find irregular air showers and determine if there are constituent sub-showers. The method first was tested on simulated shower profiles and then applied to the real Auger FD data. There are 1111981 reconstructed FD events from 2004 to 2013. We select reconstructed shower profiles using three criteria:

First: the shower profile should have 7 or more measured data points (The 2GFA fit has 6 parameters itself, and the number of parameters should be less than the fitted data points).

Second: the depth between first and last data point in the shower profile is at least 400 g/cm^2. The main reason for this criteria is that after the 2GFA fit we require the X_{max} of both sub-showers be inside the shower profile domain.

Third: all the shower profiles are already fitted with a Gaisser-Hillas function. The X_{max} found by this fit should be inside the shower profile domain. This is an important quality check to make sure both rising and falling part of the shower are detected.

In the standard Auger analysis chain there are quality checks on the results. For example, the Gaisser-Hillas fit quality must be good and the uncertainty in the reconstructed energy not too large. But in our irregular air shower analysis, we are especially interested in the events that don't fit with the Gaisser-Hillas function well. So we do not impose all the quality cuts that are done in the usual analysis. 300000 events pass all three cuts mentioned above. These events are fitted with one-GFA and two-GFA functions. In this step we have two criteria to select the events.

First: The 2GFA fit result for $X_{max}1$ and $X_{max}2$ (X_{max}'s of the two sub-showers) should lie within the shower profile domain.

Second: The ratio between the reduced χ^2 values of the one-GFA to the two-GFA fit should be larger than 1.2. We have defined this cut based on the fit results of the simulated air showers.

After implementing these two cuts almost 43000 events remain for further analysis. Figure 5.2 shows one of these events fitted to one-GFA and two-GFA functions. The two-GFA function fits nicely to this event.

5.2 Cloud Contamination

There is recorded cloud information from LIDAR, the cloud camera and GOES satellite cloud maps for many of these events. The most complete source is the satellite cloud map. More than half of all 43000 events have cloud information (25000 events). 13000 events have clear sky data, based on at least one of the cloud information sources reporting that condition (and not conflicting with other sources).

The satellite cloud map in figure 5.1 belongs to the event shown in figure 5.2. There is no sign of any cloud in this map (clear sky). So we assume there was no cloud contamination for the recorded event. Based on the discussion in section 4.1 about the cloud contamination, existence of nearby clouds is the most common reason that explains irregularity in the shower profile shape.

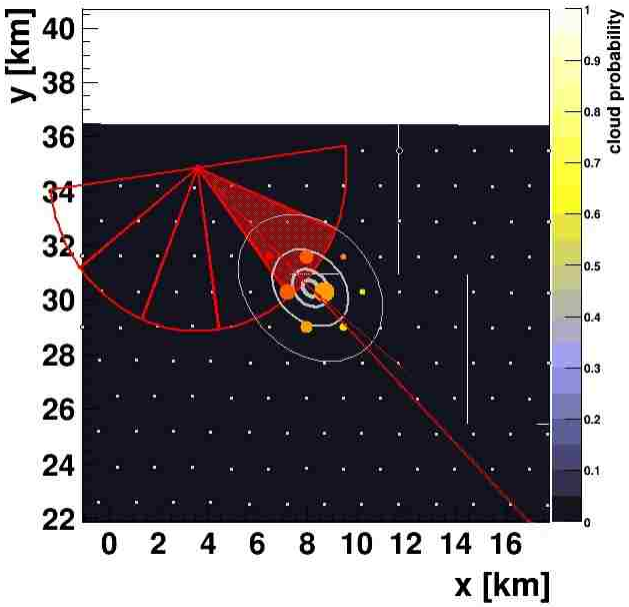

Figure 5.1: This satellite cloud map belongs to the event shown in figure 5.2. It shows a clear sky.

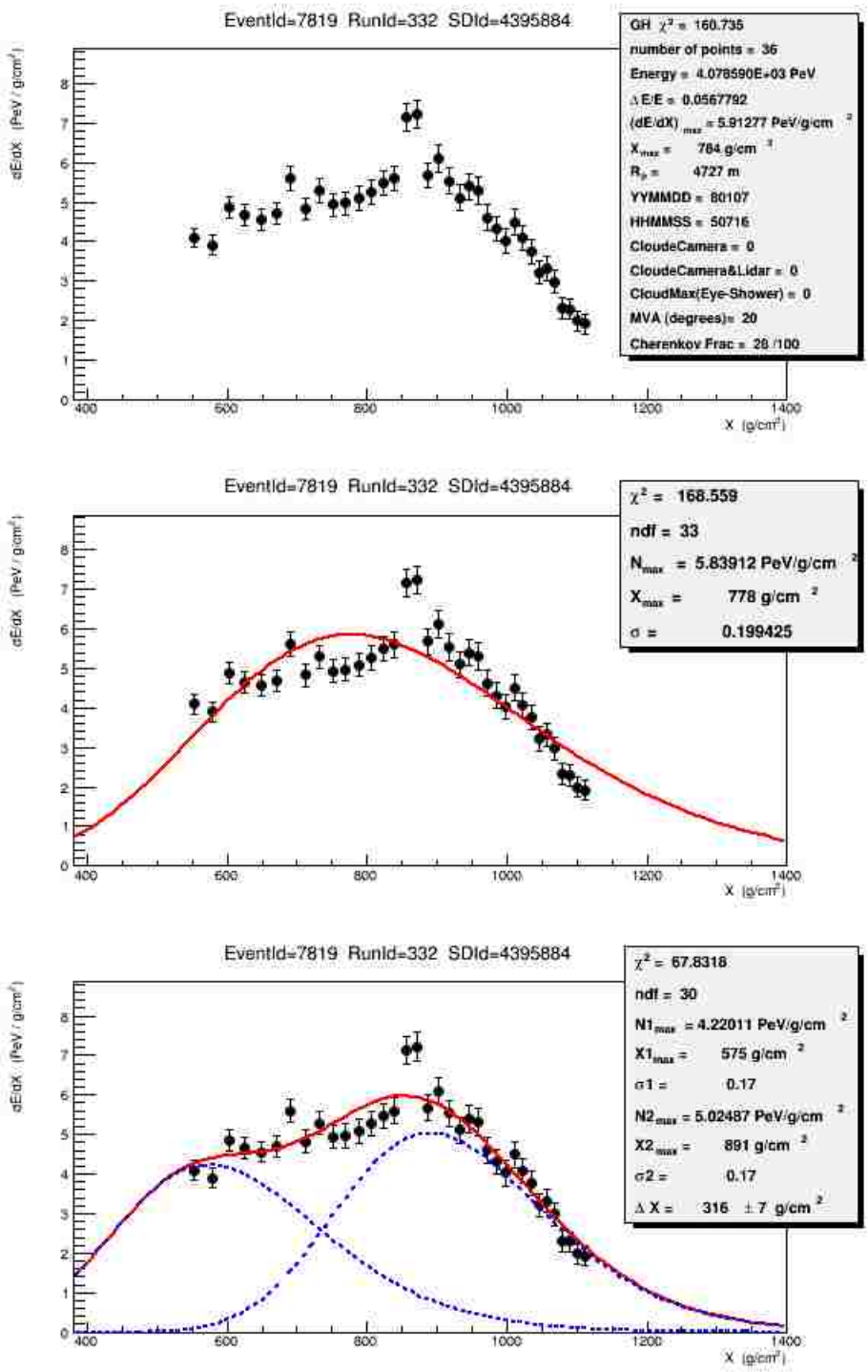

Figure 5.2: (top) A reconstructed shower profile, selected for fit. (middle) One-GFA fit on the shower profile. (bottom) Two-GFA fit on the shower profile.

5.3 Cherenkov Light Contamination

The contamination of air shower fluorescence light with Cherenkov light has been discussed in the section 4.2. Figure 5.3 shows the Cherenkov contamination fraction of the remaining events which were not contaminated with clouds. The histogram shows that most of these events have high Cherenkov contamination.

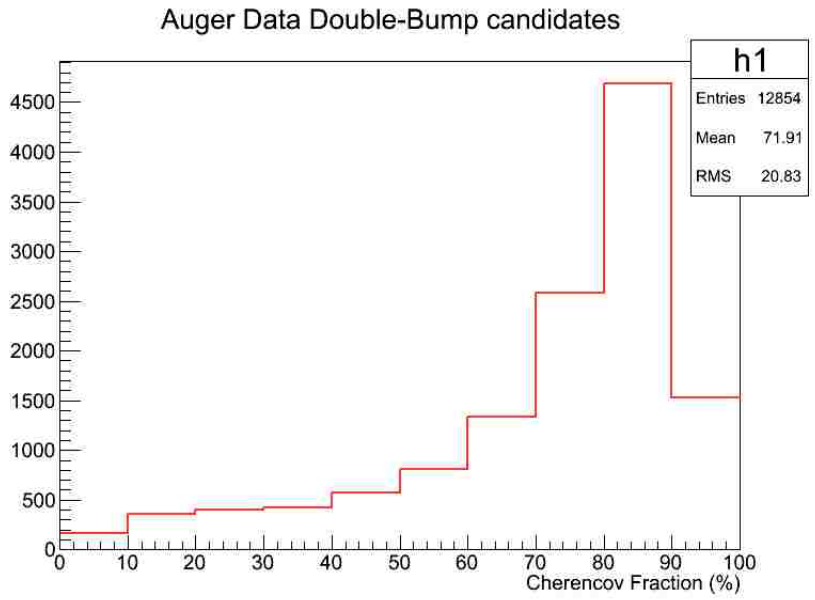

Figure 5.3: Cherenkov light contamination of the selected events. These are events that have passed all the other criteria so far.

Figure 5.4 shows the Cherenkov contamination fraction for a random sample of the Auger recorded events. The distribution indicate most of the FD events have Cherenkov fraction less than 30%. A comparison between the random shower sample (figure 5.4) and the selected double bump candidates (figure 5.3) shows that our method has a tendency to select events with high Cherenkov fraction.

We conclude that Cherenkov light contamination tends to change the measured shower profile such that it appears like the kind of irregular shower we are seeking. Events with such contamination must be eliminated from further analysis.

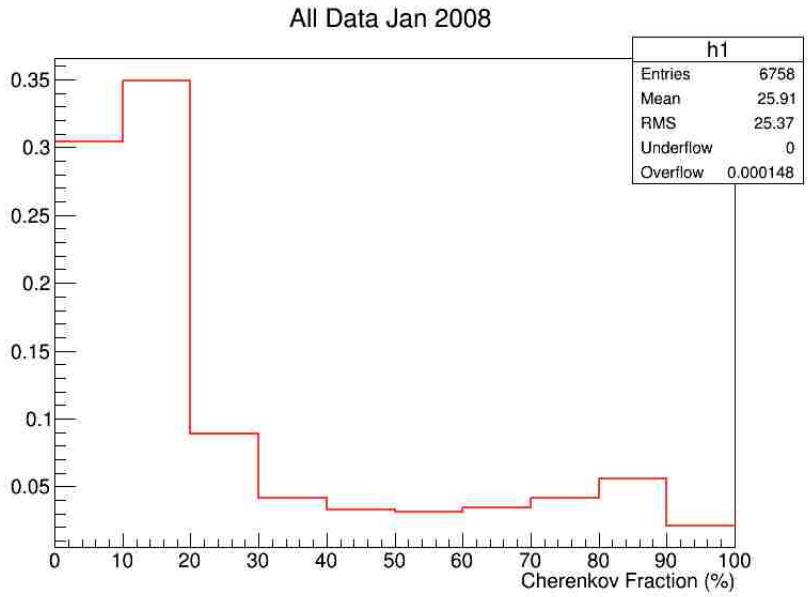

Figure 5.4: The Cherenkov light contamination for the Auger events recorded in January 2008.

Figure 5.5 shows an example of these highly contaminated events that has a nice fit with 2GFA function, and it looks similar to a double bump shower. But as the reconstruction analysis shows (figure 5.6), 84% of the detected light from this air shower belongs to the direct and scattered Cherenkov light.

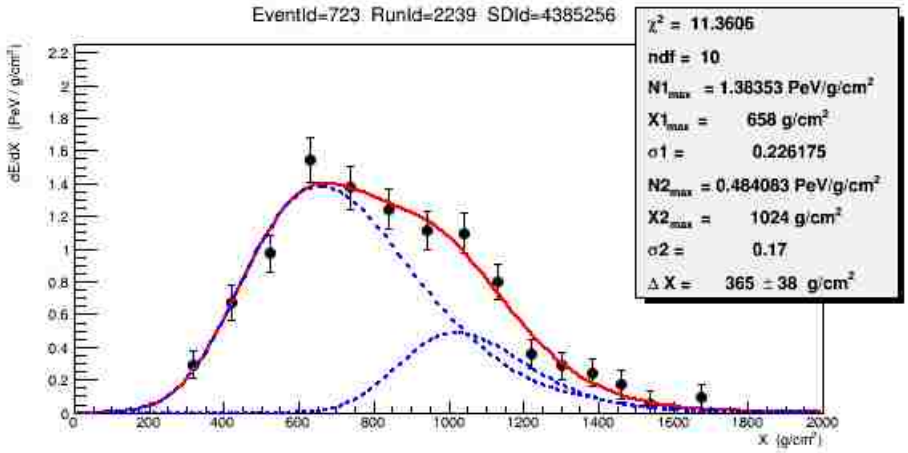

Figure 5.5: This event looks similar to a double bump air shower. But the reported Cherenkov light contamination is very high (84%).

The standard Auger analysis does not use the events with Cherenkov light contamination above 30% . So we have chosen the 30% cut for the Cherenkov light contamination. 924 events will pass this cut.

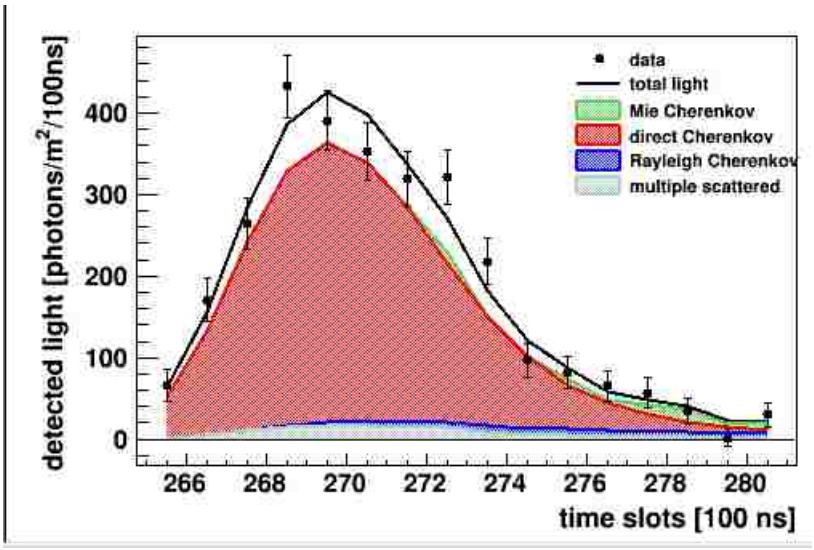

Figure 5.6: The reconstructed profile for Cherenkov light contamination of the event shown in figure 5.5.

5.4 Separation Distribution (ΔX) Between Fitted Sub-showers

Finally we have left with 924 events to analyze the 2GFA fit results. Figure 5.7 shows the ΔX distribution, which is the separation between the two X_{max} values of our fitted sub-showers.

There are many factors that determine the shape of this distribution. The real data is different from the simulations we have done in number of ways. For example, the number of data points in a shower profile, the field of view and data point uncertainties can be different for each shower. All of these affect the fit estimation from the two sub-showers. Also it can affect the selected cut on the χ^2 ratio between 1GFA and 2GFA fit.

Figure 5.8 shows the statistical errors of bin contents in the ΔX histogram. The tail of the distribution is fitted with exponential function $\exp(-\Delta X/\lambda)$ in the [420,700] interval. There are 251 events in this interval. The fitted value for λ is 67.7±4.8 and the average energy of these showers is $10^{18.2}$eV. The LP's average energy is around half of the total

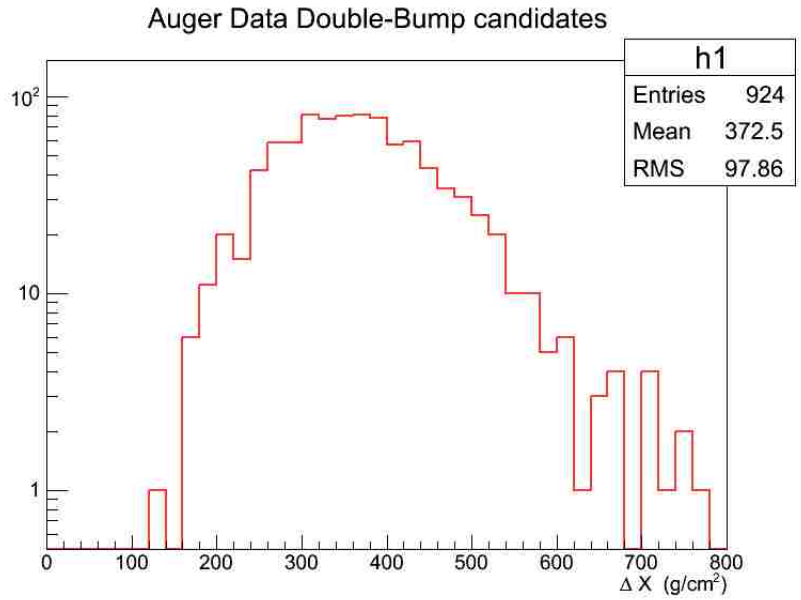

Figure 5.7: Separation between the two sub-showers in the 2GFA fit.

energy of showers.

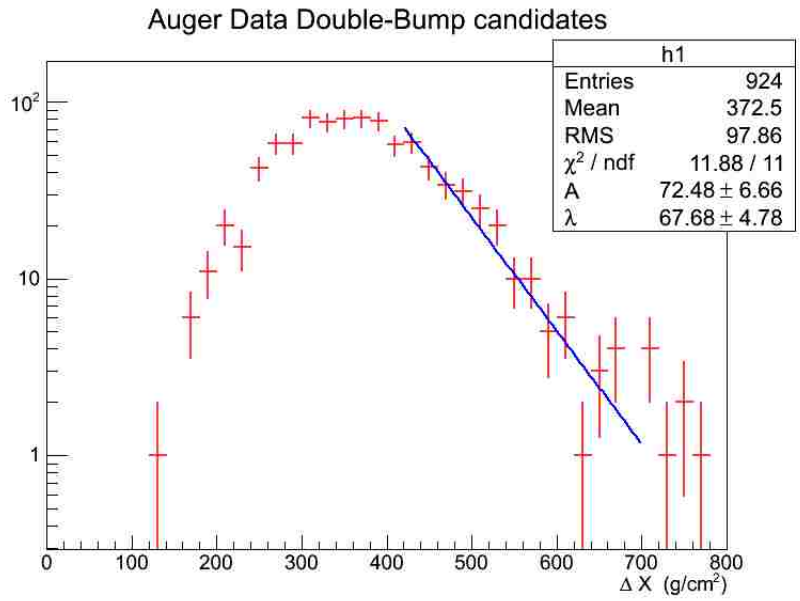

Figure 5.8: The same histogram shown in figure 5.7 with statistical error bars of the bin contents. The distribution tail is fitted with $\exp(-\Delta X/\lambda)$ function and the fitted λ is 67.68±4.78

5.5 Interpretation of the Result

In a recent analysis done by the Auger collaboration on measurement of the proton-air cross section [54], the proton-air cross section was determined from X_{max} data. The function $\exp(-X/\Lambda_\eta)$ was fit to the high tail of the X_{max} distribution (figure 5.9). The Λ_η value found is 55.8 g/cm^2 for these showers with average energy of $10^{18.24}$eV. It is discussed that for a mixed composition of hadronic showers in a narrow energy band, the proton showers are the ones that have the deepest X_{max} values. So the showers in the tail of X_{max} distribution are dominated by proton showers. There is a close relation between the fitted Λ_η value and the primary cosmic ray interaction length. For a sample of showers with varying energies, X_{max} is determined both by the initial interaction depth (which directly corresponds to the interaction length) as well as by the shower-development length which grows with energy. Hence we expect the slope of the tail of the X_{max} distribution to be a bit longer than simply given by the interaction length. In a careful, full simulation analysis on the X_{max} distribution it was found that a proton interaction length of 47.8 g/cm^2 corresponds to the observed (fitted) X_{max} distribution in the tail [54], Λ_η=55.8 g/cm^2. So the Δ fluctuations increase the X_1 distribution slope by 8 g/cm^2.

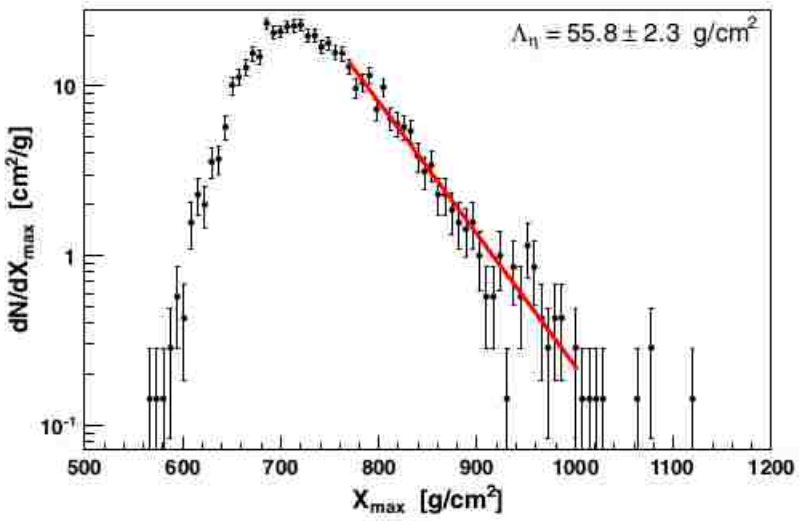

Figure 5.9: The X_{max} distribution tail is fitted with $\exp(X_{max}/\Lambda_\eta)$ function. The fitted Λ_η is 55.8±2.3 g/cm^2. The picture taken from [54]

An important difference between the X_{max} distribution analysis and our analysis here is that there are more than just protons to consider. The LP's consist of a mixture of particles (shown in figure 3.3) which mostly are p^+, n and $\pi^{\pm}$ based on the QGSJET-II simulations (not including the π^0 because it decays almost instantly). The interaction length of this mixture is 53 g/cm^2, where it is 48 g/cm^2 for proton LPs and 55 g/cm^2 for pion LPs (in QGSJET-II model). If there are heavier nuclei in the LP composition they will have much shorter interaction lengths. Hence, nuclei do not contribute to an exponential tale of the ΔX distribution.

Another difference between the X_{max} distribution analysis above and our analysis here is that we are fitting ΔX, the difference between two separated X_{max} values:

$$\Delta X = X_1(LP) + [\Delta(LP) - \Delta]. \tag{5.1}$$

In Eq. 5.1, X_1 is the distance that the leading particle travels after the first interaction. Δ and $\Delta(LP)$ are the shower development lengths for the initial shower and for the second shower (initiated by the leading particle) respectively. Our aim is to measure the exponential distribution of X_1 using the measured values of ΔX.

The fluctuations of the quantity $(\Delta(LP) - \Delta)$ in Eq. 5.1 must be estimated in order to assess the uncertainty in our result. $\Delta(LP)$ and Δ are independent variables and they have almost the same fluctuations, so we can approximate as follows:

$$\text{Fluctuations}[\Delta(LP) - \Delta] \simeq \sqrt{2}\ \text{Fluctuations}[\Delta]$$

where from the X_{max} distribution analysis we know the fluctuations for Δ is 8 g/cm^2. So the fluctuations of $[\Delta(LP) - \Delta]$ is 11.2 g/cm^2 approximately.
Now we subtract the $[\Delta(LP) - \Delta]$ fluctuations effect from the fitted ΔX distribution tail.

The result gives the interaction length for LPs as

$$\lambda_{int}(LP) = 67.7 \text{ g/cm}^2 - 11.2 \text{ g/cm}^2 = 56.5 \text{ g/cm}^2.$$

If we assume the LP composition is same as the QGSJET-II model prediction (shown in figure 3.3), then we can compare the $\lambda_{int}(LP)$=56.5 g/cm^2 with the simulation value and determine the proton interaction length.

$$\begin{aligned} \text{Simulation:} \quad & \lambda_{int}(LP) = 53\text{g/cm}^2 \longrightarrow \lambda_{int}(p^+) = 48\text{g/cm}^2 \\ \text{Auger Data:} \quad & \lambda_{int}(LP) = 56.5\text{g/cm}^2 \longrightarrow \lambda_{int}(p^+) = \ 51\text{g/cm}^2 \end{aligned} \tag{5.2}$$

The $\lambda_{int}(p^+)$ for the auger data is determined to be 51 g/cm^2 with a simple comparison from relationship 5.2.

An effect that could add to the overestimation of the LP interaction length in our analysis is that the leading particle interaction produces its own leading particle. Some small fraction of the time, this may have sufficient energy to complicate our result. As shown in figure 3.37, if the LP doesn't lose much energy in its interaction with air then the track length of LP and LP-of-LP will be added together.
Based on all these factors, we conclude the following:

- The air showers with large ΔX in this analysis are proton (or light nuclei) air showers (assuming that Auger events have mixed composition (proton and Iron)).
- The fitted $\lambda = 67.7 \pm 4.8$ g/cm^2 for the ΔX distribution tail corresponds to 56.5 g/cm^2 interaction length for LPs. If we assume the LP composition be same as it is predicted by QGSGET-II model, then the proton interaction length will be 51 ± 4.8 g/cm^{2}s. Where the average LP (and proton) energy is $E = \frac{1}{2} \times 10^{18.2} eV$ (the one half

coefficient is an approximation of E_{LP}/E_{total}).

$$\lambda_{int}(LP) = 56.5 \pm 4.8 \quad \mathrm{g/cm^2}$$

$$\lambda_{int}(p^+) = 51 \pm 4.8 \quad \mathrm{g/cm^2}$$

$$< E > = \frac{1}{2} \times 10^{18.2} eV$$

Bibliography

[1] Hess,V., "Uber Beobachtungen der durchdringenden Strahlung bei sieben Freiballonfahrten", *Physikalische. Zeitschrift.* 13: 1084-1091. (1912).

[2] Carl D. Anderson., "the positive electron", *Phys. Rev.*, 43:491494, Mar 1933.

[3] Seth H. Neddermeyer and Carl D. Anderson., "Nature of cosmic-ray particles", *Rev. Mod. Phys.*, 11:191207, Jul 1939.

[4] G. Occhialini and C. Powell., "nuclear disintegrations produced by slow charged particles of small mass", *Nature*, 159:186190, Feb 1947.

[5] J. Linsley, "Evidence for a Primary Cosmic-Ray Particle with Energy 1020 eV", Physical Review Letters 10 (4): 146. (1963).

[6] P. Auger, P. Ehrenfest, R. Maze, J. Daudin and A. F. Robley,"Extensive cosmic ray showers, *Rev. Mod. Phys.* 11, 288 (1939).

[7] E. Fermi "On the origin of the cosmic radiation" Phys. Rev. 75 (Apr, 1949) 11691174.

[8] T. Stanev "High energy Cosmic Rays" springer-praxis puublishing Ltd 2004

[9] J. R. Jokipii "Rate of the energy gain and maximum energy in difussive shock acceleration" Astrophysical Journal, 313:842-846, 1987

[10] W.I. Axford, Proc. 15th Cosmic Ray Conf. (Plovdiv), 11, 132 (1977)

[11] A.R. Bell, Mon. Not. R. Astr. soc., 182, 443 (1978)

[12] M. S. Longair "High Energy Astrophysics" Cambridge University Press 1981

[13] A. A. Penzias and R. W. Wilson,"A measurement of excess antenna temperature at 4080 mc/s. ", Astrophys. J. 142 (July, 1965) 419-421.

[14] K. Greisen, "End to the cosmic-ray spectrum?" Phys. Rev. Lett. 16 (Apr, 1966) 748-750.

[15] G. T. Zatsepin and V. A. Kuz'min, "Upper limit of the cosmic-ray spectrum" Zh. Eksp. Teor. Fiz., Pis'ma Red. 4 (1966), no. 3, 114-17.

[16] T. Stanev"High Energy Cosmic Rays" 2nd Edition, Springer (2004)

[17] G. F. Smoot, D. Scott "Cosmic background radiation" European Physial Journal C - Particles and Fields (2000) volume 15, issue 1-4, pp 145-149

[18] A. Mucke "Monte Carlo simulations of photohadronic processes in astrophysics" Computer Physics Communications, Volume 124, Issue 2, p. 290-314. (2000)

[19] A. A. Watson "Extensive Air Showers and Ultra High Energy Cosmic Rays" Lectures given at a Summer School in Mexico: 2002

[20] "Cosmic rays: the most energetic particles in the universe" Reviews of Modern Physics, Vol. 71, No. 2, Centenary 1999

[21] Cronin, J.W., Nuclear Physics B (Proc.Suppl.), 28B, 213 (1992).

[22] The Auger Collaboration "Technical Design Report"

[23] The Auger Collaboration "Properties and performance of the prototype instrument for the Pierre Auger Observatory" Nuclear Instruments and Methods in Physics Research A 523 (2004) 5095

[24] Stefano Argiro "Performance of the Pierre Auger Fluorescence Detector and Analysis of Well Reconstructed Events" 28th International Cosmic Ray Conference

[25] Segev BenZvi "The Lidar System of the Pierre Auger Observatory" Volume 574, Issue 1, 21 April 2007, Pages 171184

[26] Peter K.F. Grieder. "Hadronic interactions and cascades In Extensive Air Showers", pages 77146. Springer Berlin Heidelberg, 2010. 10.1007/978- 3-540-76941-5-3.

[27] S.S. Ostapchenko, Nucl. Phys. B (Proc. Suppl.) 151 (2006) 143-147

[28] T. Bergmann et al., Astropart. Phys. 26 (2007) 420432

[29] J. Matthews "Information on Cross Sections and Composition from Fluctuations of Xmax" Auger gap-note 2010-087.

[30] J. Stapeleton "A Three-Parameter Analysis of Fluctuations in Xmax" Auger gap-note 2010-105

[31] Gaisser, T.K.; Hillas, A.M. (1977). Proceedings of the 15th International Cosmic Ray Conference, 13-26 Aug 1977. 8. Plovdiv, Bulgaria. pp. 353.

[32] M. Giller, A. Kacperczyk, J. Malinowski, W. Tkaczyk, and G. Wieczorek, "Similarity of extensive air showers with respect to the shower age" Journal of Physics G Nuclear Physics 31 (2005) 947958.

[33] Chihwa Song, "Longitudinal profile of extensive air showers" Astropart.Phys. 22 (2004) 151-158

[34] Rene Brun and Fons Rademakers, ROOT - An Object Oriented Data Analysis Framework, Proceedings AIHENP'96 Workshop, Lausanne, Sep. 1996, Nucl. Inst. & Meth. in Phys. Res. A 389 (1997) 81-86. See also <http://root.cern.ch/>.

[35] J. Chirinos "Identifying Clouds Over the Southern Auger Observatory using Satellite Data" Gap-2010-094

[36] P. Abreu et al. "Identifying clouds over the Pierre Auger Observatory using infrared satellite data" Astroparticle Physics, Volumes 5052, December 2013, Pages 92101

[37] "GOES Project Science", <http://goes.gsfc.nasa.gov/>

[38] J. Chirinos "Ground-truthing a satellite-based night-time cloud identification technique at the pierre Auger Observatory" Eur. Phys. J. Plus (2012) 127:93

[39] "NOAA Geostationary Satellite Server", <http://www.goes.noaa.gov/>

[40] Arne Schnwald, "Measurement of the cosmic ray flux with H.E.S.S ", DIPLOMARBEIT, HUMBOLDT-UNIVERSITT ZU BERLIN 2008

[41] F. Nerling "Universality of electron distributions in high-energy air showersDescription of Cherenkov light production", Astroparticle Physics 24 (2006) 421437

[42] S. Cecchini "Atmospheric muons: experimental aspects", *Geosci. Instrum. Method. Data Syst.*, 1, 185196, 2012

[43] Philip E. Ciddor, "Refractive index of air: new equations for the visible and near infrared", Appl. Optics 35, 1566-1573 (1996)

[44] T. Stanev, "High Energy Cosmic Rays", Springer, 2003. Print.

[45] Auger Collaboration Gap-note 2005-063

[46] K. Bernlhr. "CORSIKA and sim hessarray Simulation of the Imaging Atmospheric Cerenkov Technique for the H.E.S.S. Experiment". H.E.S.S. internal note 02/04 (unpublished), 2000.

[47] Anthony Bucholtz, "Rayleigh-scattering calculations for the terrestrial atmosphere" *Applied Optics* vol 34, No 15 (1995)

[48] Karim Louedec, "Atmospheric Aerosols at Pierre Auger Observatory and environmental implications" *Eur. Phys. J. Plus* (2012) **127**:97

[49] Simon A. Scarn, presentation, Michigan Tech. University, Geological & mining enginnering

[50] M. Unger "Reconstruction of longitudinal profiles of ultra high energy cosmic rays showers from fluorescence and Cherenkov light measurements", Nuclear Instruments and Methods in Physics Research A 588 (2008) 433-441

[51] A. M. Hillas "Angular and energy distribution of charged particles in electron-photon cascades in air", J. Phys. G:Nucl. Phys. 8 (1982) 1461-1473

[52] Auger Collaboration Gap-note 2006-010

[53] A. A. Watson "The Role of Cherenkov Radiation in the Detection of Ultra High Energy Cosmic Rays"

[54] The Auger Collaboration "Measurement of the Proton-Air Cross Section at $\sqrt{s} = 57\ TeV$ with the Pierre Auger Observatory" Physical Review Letters, vol. 109, Issue 6, id. 062002

Vita

Amir Hosein Shadkam was born in Tehran, Iran, in 1983. He received his Bachelor Degree in Physics from Sharif University of Technology in 2006. He has joined the cosmic ray research lab in Sharif University of Technology from 2006 to 2008. He began his graduate study at Louisiana State University in Fall 2008. He expects to complete his doctoral degree in August 2014.